Characterization of deep UV photoresist properties by infrared near-field scanning optical microscopy and related methods

D i s s e r t a t i o n
zur Erlangung des Grades eines Doktors
der Naturwissenschaften

vorgelegt von
Jan Preußer
aus Otterndorf

genehmigt von der
Mathematisch-Naturwissenschaftlichen Fakultät
der Technischen Universität Clausthal

Tag der mündlichen Prüfung
7. Juli 2003

Vorsitzender der Prüfungskommission . . . . . Prof. Dr. D. Mayer

Hauptberichterstatter . . . . . Prof. Dr. W. Schade

Berichterstatter . . . . . Prof. Dr. D. Kip

Die vorliegende Arbeit wurde im Zeitraum vom November 1998 bis Juni 2003 am Institut für Physik und Physikalische Technologien der Technischen Universität Clausthal sowie am JILA, University of Colorado in Boulder, USA angefertigt.

Contents

1 Introduction

With advancing needs for higher packaging densities in chip technology, smaller and smaller feature sizes have to be realized in substrate materials used for microchip fabrication. It was proposed that the development in decreasing structure size follows an exponential behavior, also termed "Moore's Law" [1].

Today probably the most limiting factor is given by the photolithographic process, which is used to transfer an image of the designed structure onto the semiconductor. Polymeric photoresists are the key component in industry for patterning semiconductors, flat panel displays and data storage device components. An important step towards even smaller features was taken by Ito and coworkers [2, 3] by developing chemically amplified photoresists, which allow for an optical lithography process beyond Rayleigh's resolution limit. While the smallest dimensions possible scaled directly with the wavelength of light used in the lithographic process, the new resists open a range of possibilities due to their nonlinear response to UV irradiation.

With the introduction of acid-catalyzed chemically amplified photoresist chemistry, a microscopic understanding of dynamics in the photopolymers is needed. Latent image metrology provides the means to study the evolution of resist profiles at different steps of the pattern formation: after exposure, postexposure bake and development. Image spreading and surface roughness are only two examples of parameters that have to be understood and controlled on a nanometer length scale.

While optical microscopy utilizes fluorescent tracers to track diffusion properties and feature broadening at a microscopic level, other work employs atomic force microscopy to perform topographic profiling and examine local shrinkage, which is related to the acid-catalyzed process. Fourier transform infrared spectroscopy (FTIR) is used to deliver macroscopic information on bulk samples but none of the techniques above allow to gain unperturbed in-situ information on the dynamics in patterned photolithographic polymers.

Near-field scanning optical microscopy (NSOM) offers the possibility to obtain images at lateral resolutions far beyond the diffraction limit impinged on conventional microscopy. This is achieved by illuminating the sample through a subwavelength aperture in

proximity to the sample surface. Hence the resolution is given by the physical dimensions of the aperture rather than the wavelength of light. By scanning the miniature "light source" across the sample an image of the surface is obtained sequentially [4].

Since the optical resolution is not limited by the wavelength used, the wavelength range can be extended to the infrared regime at roughly the same high resolution as demonstrated for the visible regime [5, 6]. The key advantage of IR-NSOM is the chemical subgroup specificity, which allows determination of various chemical species at high spatial resolution. In case of photoresist systems this method will be used to map the polymer distribution of areas that have or have not been deprotected by the chemically amplified process. Different subgroups (OH and CH respectively) characterize polymers before and after deprotection and hence deliver the spatial distribution of the catalytic reaction in the latent image formation.

Measurements of the image spreading will be demonstrated and a closer look at the contrast and image formation in IR-NSOM will be given. It will also be shown that the lithographic mask causes optical artifacts due to UV light diffraction at the edges of the mask. A simple model allows a qualitative explanation of this artifact in the latent image.

While fourier transform infrared spectroscopy is widely used for gas phase applications or measurements on bulk materials and provides insight to the molecular subgroups of the sample, it lacks spatial resolution to observe the image spreading in photoresist patterning locally. By combining FTIR with a lithographic method to write highly reproducible periodical structures, averaging over many features will deliver a macroscopically scaled image of the dynamics happening locally at a single edge. From these measurements the nonlinear UV response of a specific chemically amplified resist will be extracted as well as the diffusion constant for the acid catalyzed reaction. A subsequent model allows the determination of the initial acid concentration in the latent image prior to and during diffusion.

Another prospect is to characterize the polymeric photoresist films on the length scale of the macromolecules involved. A method closely related to that of near-field scanning optical microscopy as described before will be introduced. Here, a tiny scatterer is used as a probe and the interaction between the probe and the sample, based on dipole-dipole coupling is monitored. By scattering light of a tiny subwavelength probe, using an aperture is obsolete. Since simple scatterers can be manufactured reproducibly on a much smaller

scale than apertures, the theoretical resolution of such a microscope reaches the atomic level. The superior lateral optical resolution will be demonstrated and the instrument will be characterized by suitable samples. A class of samples based on diblock copolymers will be examined, since copolymers are thought to be used for nanolithographic patterning of surfaces. Self-assembly of these polymers on flat surfaces can be used to deliver for example metal nanoparticles at controlled lateral distances. Finally measurements will be performed on photolithographic samples and contrast mechanism as well as microscope performance will be discussed.

2 Fundamentals of lithography

2.1 Introduction to optical lithography in semiconductor device manufacturing

Lithography in its general meaning describes a method of transferring a pattern structure from a master onto a substrate with the goal to produce an image or reprint of the original pattern. While this method was invented originally for duplication of printed matters, with the master made out of wood or metal and ink was used to transfer the pattern, lithography today finds a much broader application range [7]. As one of the key manufacturing processes, lithography plays an important role in semiconductor industry [1].

In order to transfer a pattern onto the semiconductor surface a thin layer of photopolymer resist is spin-coated on the substrate. UV light irradiation of the photoresist through a mask leaves exposed and unexposed regions, which alter the chemical structure of the exposed resist. As a result the solubility changes locally. In the following development step, either the irradiated (positive tone) or the unaltered parts (negative tone) are removed, which leaves defined areas of the substrate unprotected. An etching process that is designed to attack the substrate but not the protecting polymer layer transfers the photoresist pattern into the substrate sample. By the end of this process an image of the mask is written into the substrate [8, 9, 10].

This fairly complicated process of imprinting a given pattern on a substrate involves a great range of knowledge for each step of the lithographic procedure. A key technology hereby is the photoresist resin, which is namely responsible for the feature sizes later etched into the substrate. Photoresists play a quintessential role in the advancing optical resolution, which allows for structures smaller than dictated by the Rayleigh diffraction limit. The requirements for a lithographic resist are manifold, but a few functional properties are fundamental to every resist:

- The resist has to form a uniform and defect-free thin film on the substrate material.
- Adhesion to the substrate is required throughout the image transfer and development process.

- The resist has to provide a high reproducibility for the smallest features that it is used for as well as for the UV response, which resembles mainly the contrast in the latent image.

- During the image transfer into the substrate, the resist has to withstand the etching procedures that are designed to remove substrate material, for example plasma etching. In addition it is also required that the material covered by the resist is protected from the etching impact.

- For industrial applications it is important that the resist has a high radiation sensitivity, such that the exposure process takes up only a short amount of time of the whole image transfer, hence allowing for a larger throughput.

- After the image transfer it must be possible to remove the resist completely without damaging the substrate and its patterning.

A standard photoresist, that is used since the early 1960s, is the single-layer resist diazonaphthoquinone (DNQ) (novolac resin) [11, 12]. Exposure to 365 nm light converts the DNQ dissolution inhibitor into an acidic photoproduct, which is soluble by a base. Therefore the dissolution rate is increased in the exposed regions, leading to a fairly linear response of the resin to the amount of exposure. As a consequence, the image that is produced by the mask is ported also linearly into the photoresin. This puts limitations to the feature size, since diffraction occurs at the edge of the mask and hence does not allow the production of features much smaller than the exposure wavelength. Consequently only lowering the wavelength of light will give smaller features [13]. This is not easily extendable since DNQ-novolac resins are basically opaque for lower wavelengths than 300 nm. Another restriction is the overall brightness of light sources available for DUV exposure, which is much less than that of mercury arc lamps used at 365 nm. Though KrF excimer lasers ($\lambda = 248$ nm) are regarded as powerful sources of UV light, the spectral output line is relatively broad. Limitations of available lens materials for the projection make correction for chromatic abberation difficult, so the source output beam must span only a very narrow wavelength range. Introducing elements to spectrally narrow the wavelength output leads to a large attenuation. Hence, the photoresist must be much more sensitive to UV doses, when applied in the deeper UV range.

In a new approach, resists are developed, that have a highly nonlinear characteristic to UV exposure [2, 3]. By combining such advanced resists with high-quality projection optics, today's manufactured feature sizes can be smaller than 100 nm [14].

2.2 Chemically amplified photoresists

2.2.1 Nonlinear chemistry in latent image formation

Chemically amplified deep-ultraviolet photo resists were first described in the 1980s by Ito, Willson and Frechet [2, 3], and represent a fundamental change from the linear DNQ resin. In systems of this type, a latent image of photogenerated acid is produced in the resist film upon exposure to UV light. A subsequent post-exposure bake (PEB) drives a thermal reaction, causing a change in the aqueous base solubility of the resist in the exposed regions. Due to this decoupling of the photochemical and the thermal reactions, new variables that affect the resolution are introduced into the resist process. For example, the resists linewidths have been reported to depend strongly on factors as changes in the postexposure baketime and temperature [15, 16]. Also the volatilization of gaseous compounds as well as the diffusion properties of photoacid within the resist have big influences on the spreading of the features in the resist [17, 18].

So the general step of transferring the UV image to a latent image in the resist is composed of two elements: First photolysis leads to production of acid in the exposed regions, which is caused by photoacid generators placed in the polymer matrix. After the exposure process, heat is applied to the substrate. With the thermal energy, the acid molecules gain mobility and lead to deprotection of the surrounding polymer chains. One of the products of this chemical reaction is another acid molecule, which in turn can affect other polymers. This catalysis reaction receives its energy for the deprotection step as well as the mobility necessary to reach beyond his direct neighbor molecule from the baking process [19]. Usually chain reactions like this are known to produce 800-1100 new acid molecules upon thermolysis [20]. This process leads to a highly nonlinear response function of the chemically amplified resist to UV exposure as depicted simplified in figure 2.1 [16].

2.2.2 Poly(t-butoxyoxycarbonylstyrene) (PTBOCST)

One candidate for chemically amplified photoresists is the polymer poly(t-butoxyoxycarbonylstyrene) (PTBOCST). The chemical structure is shown on the left in figure 2.2.

Upon acid presence the TBOC-groups convert from nonpolar PTBOCST to poly(hydroxystyrene) (PHOST), which is polar. Next to some volatile products

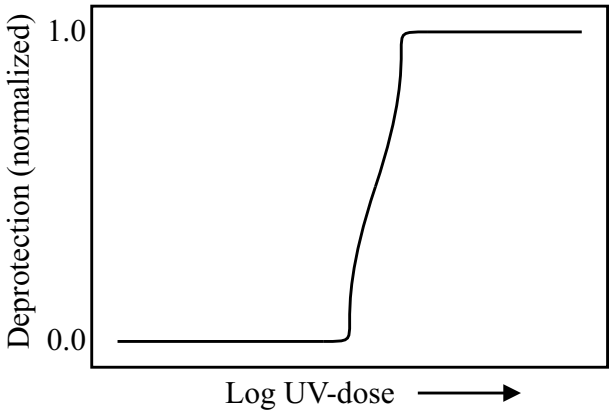

Figure 2.1: This simplified diagram shows the highly nonlinear response of modern chemically amplified photoresists.

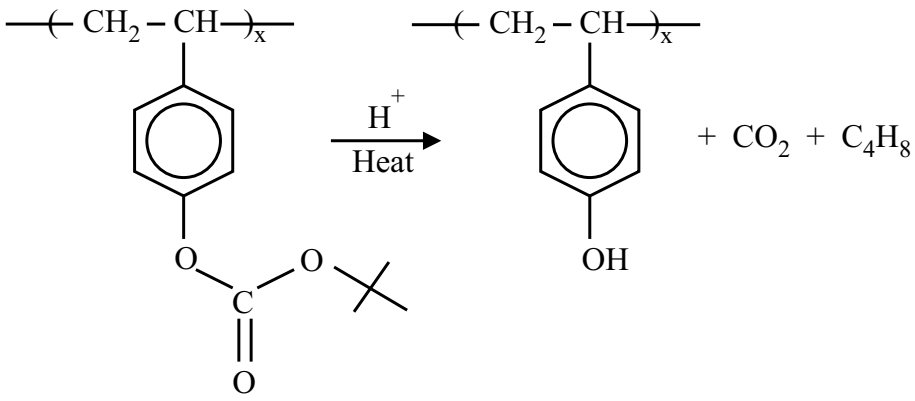

Figure 2.2: Chemical deprotection process for PTBOCST

this reaction also regenerates the initial acid. The chemical structure of (PHOST) can be found on the right of figure 2.2. Initial acid to start this so-called deprotection process is provided by doping PTBOCST with a photoacid generator (PAG). Onium salts are typically used since they belong to a class of compounds that efficiently generate a Bronsted acid upon photolysis (figure 2.3) [21].

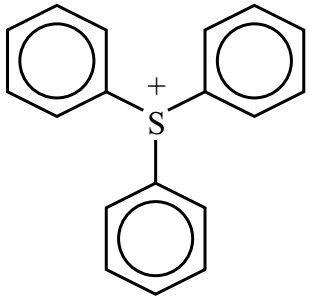

Figure 2.3: Photoacid generator (PAG): onium salt

After the thermolysis step, deprotected areas, which now consist of PHOST, are vulnerable to nonpolar solvents, while the chemically unaltered sites of PTBOCST are solvable in polar solutions. Hence, this photopolymer resist can easily be used as a positive- as well as a negative-tone resist.

The overall efficiency of a chemically amplified system can be expressed as the catalytic chain length, basically the number of deprotected polymer-groups per one initial acid molecule. For PTBOCST it is measured to be in the range of 800-1100 deprotected sites per acid molecule. As a consequence only very low exposure doses are needed to start photolysis on a few photoacid generators, while the complete deprotection of an area is governed by the catalytic chain reaction. This makes the chemically amplified photoresists very sensitive to UV irradiation, which is one of the requirements for deep UV lithography as pointed out earlier.

Indicators for the transition between the original polymer material and its deprotected successor are visible in the infrared spectrum due to vibrational and rotational contributions of the specific subgroups [22, 23]. Figure 2.4 shows a typical spectrum recorded on a 1.2 μm thick film of PTBOCST in the spectral range of 4000 to 1500 cm^{-1} (2500-6667 nm). A strong and narrow absorption peak at 1750 cm^{-1} can be assigned to the carbonyl-group present in PTBOCST. As expected, with the loss of this group after deprotection the peak also vanishes as well as the CH peak at 3000 cm^{-1}. On the other hand the rising

of a broad absorption line around 3400 cm^{-1} indicates the presence of an OH group, which can be found in PHOST. Typical absorption coefficients for the CH as well as the OH band are determined to $\alpha = 0.04\ \mu m^{-1}$, while the peak at 1750 cm^{-1} has an absorption coefficient of $\alpha = 0.24\ \mu m^{-1}$. Since all following experiments were conducted on sapphire, the strong absorption of the carbonyl group had to be discarded for infrared tracking of the photopolymer dynamics due to sapphire being opaque in this specific wavelength range.

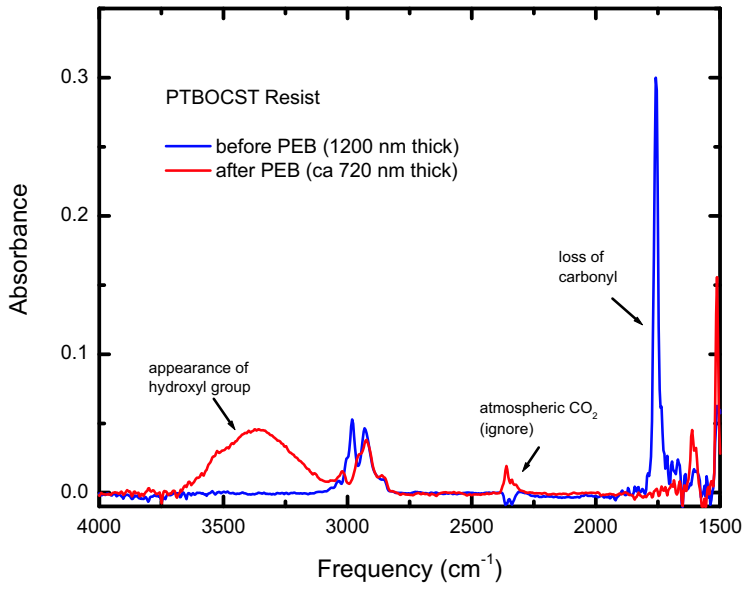

Figure 2.4: Infrared spectrum of PTBOCST and the deprotected polymer (PHOST). The strong peak at 2981 cm^{-1} can be attributed to a CH bond, while the absorption at 3379 cm^{-1} is due to a change in the hydroxyl-group (OH).

2.2.3 Poly(t-butylmethacrylate) (PTBMA)

Yet an alternative chemically amplified photoresist is the polymer poly(t-butylmethacrylate) (PTBMA). The chosen photoacid generator is also an onium salt (TPS-SbF_6), forming hexafluoroantimonic acid upon photolysis. The deprotected form of the polymer is poly(methacrylate acid) (PMAA), which results from the photoacid catalyzed decomposition of the t-butoxycarbonyl groups. In figure 2.5 the infrared spectrum shows similar behavior as the previous polymer system. Again deprotection specific absorption can be found around 3000 cm^{-1}, which consists of a fairly narrow CH stretch, that can be attributed to the original polymer PTBMA and vanishes in the broad hydroxyl-band of the deprotected PMAA.

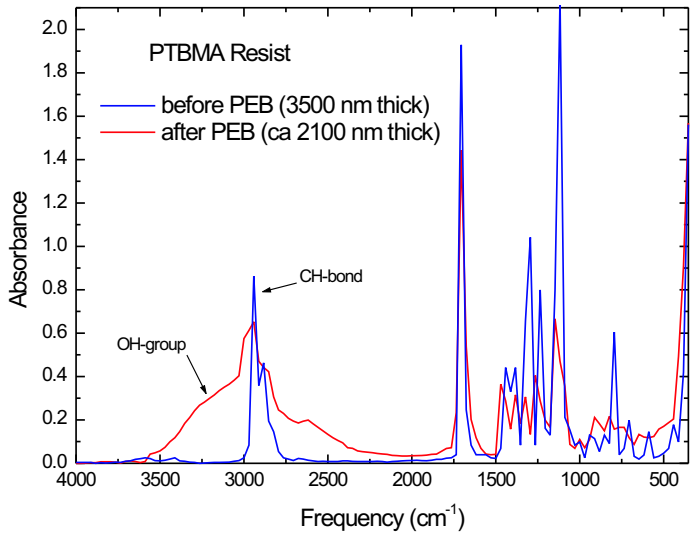

Figure 2.5: Infrared spectrum of PTBMA and its deprotected derivative PMAA. The peaks identifying the deprotection process are the CH absorption at 2900 cm^{-1} and the OH band, which also peaks at about 2900 cm^{-1} but is much broader in appearance.

2.3 Diffusion in polymers

Acid diffusion during postexposure baking is viewed to be a limiting factor in the extension of lithography by chemically amplified photoresists. It is therefore important to quantify the diffusion processes, that are occurring in the latent image formation.

In general diffusion is described as the movement of matter from one part of a system to another due to random motion of the particles [24]. Many factors influence diffusion, such as temperature, viscosity, size of the diffusing particles and pressure. It is also important to differentiate between gaseous diffusion, which is fast (10 cm/min), compared to diffusion in liquids (0.05 cm/min) or even solids (0.1 μm/min). Because diffusion coefficients span a much larger range in solids, theoretical descriptions are difficult to estimate, while experimental results can be matched well with theoretical models in gases and liquids [25]. Diffusion rates of polymeric systems are usually found to lie between those of liquid and solid phases and depend, in addition to the above mentioned factors, on the degree of swelling and polymer concentration. It has been observed, that diffusion rates are also influenced by the backbone orientation of the polymer and transport phenomena have been reported, where the electrostatic charge of ions led to attraction between diffusing solvent and polymer matrix, hence resulting in a reduction of diffusion rates [26]. Therefore it is very difficult to develop theoretical estimates, which hold up well with experimental results.

A simple mathematical description of diffusion was first established by Fick, who developed a diffusion relation for one dimension [27]:

$$J_x = -AD\frac{\partial c}{\partial x}, \tag{2.1}$$

where J is the flux, A the area across which diffusion occurs, D the diffusion constant and $\partial c/\partial z$ describes the concentration gradient along the x-axis. For an unitary area and with the absence of convection, the above equation simplifies to

$$J_x = -D\frac{\partial c}{\partial x} \tag{2.2}$$

In the study of solvent diffusion in polymers, different behaviors have been observed, depending on the physical properties of the polymer network and the interaction between the polymer and the solvent itself. According to the solvent diffusion rate and the polymer relaxation, diffusion can be characterized as Fickian (Case I) or non-Fickian diffusion. The

second case is subdivided into anomalous and Case II diffusion [28].
Fickian diffusion is often observed in polymer networks, with temperatures well above the glass transition temperature of the polymer. When the polymer is in this rubbery state, the polymer chains have a higher mobility, which allows an easier penetration of the solvent [29]. Therefore, Fickian diffusion is characterized by a solvent diffusion rate, which is slower than the polymer relaxation. A large gradient of solvent penetration is typical in these systems. The solvent concentration profile shows an exponential behavior and the diffusion distance is proportional to the square-root of time [30]. This is expressed by the amount of absorbed solvent per unit area M of a polymer at time t

$$M(t) = kt^{1/2} \tag{2.3}$$

The non-Fickian case of diffusion is mainly observed in glassy polymers, where the temperatures were kept below the glass transition temperature. At lower temperatures the polymer chains are not sufficiently mobile to permit immediate penetration of the solvent in the polymer matrix [29]. The two sub-categories Case II and anomalous diffusion can be distinguished by the the ratio between the solvent diffusion rate and the polymer relaxation process. For Case II the polymer matrix relaxes on a much slower timescale than the solvent diffusion is happening. This leads to a pronounced solvent concentration front, that is trying to move into the polymer and the solvent diffuses at a constant rate, thus the diffusion distance is directly proportional with time

$$M(t) = kt. \tag{2.4}$$

It is also possible to find a mixed diffusion process, which is the case when the solvent diffusion rate and the polymer relaxation rate are about the same order of magnitude. With this so-called anomalous diffusion transport processes, which are not Case I or Case II diffusion can be characterized. Hence the above equation for M becomes

$$M(t) = kt^n, \tag{2.5}$$

with $1/2 < n < 1$.
Experiments for diffusion usually try to quantify system specific diffusion coefficients D. Depending on the method used to determine concentration changes due to diffusion, the diffusion coefficient can either be linked directly to the measured length of diffusion during a time interval t [31]

$$D = \frac{L^2}{2t}, \tag{2.6}$$

where L is the observed length in diffusion during time t. Using Arrhenius theory it is also possible to describe the temperature dependence of a chemical chain reaction due to

diffusion, which is expressed by

$$D = Ae^{-\frac{E_a}{RT}}, \tag{2.7}$$

with E_a being the activation energy, and T the temperature of the system. Values for E_a are mostly obtained experimentally [32, 33] or by numerical simulation [34], so from the activation energy of a diffusant in a given system, information can be obtained about the polymer network in which the diffusion takes place [22]. With the above equations based on Fick's formalism, it is already possible to develop numerical simulations for thin film diffusion in polymeric blends. These models are either based on free volume theory, diffusion based on obstruction effects (hard sphere theory) or hydrodynamic theories [35, 36, 37, 38, 39].

3 Image formation in optical microscopy

3.1 Resolution limit in conventional microscopy

In conventional microscopy a magnified optical image of an object is created. This is realized by a combination of at least two lenses, which in practical applications will be replaced by two lens systems to correct for abberations, maximize magnification and allow longer working distances at high numerical apertures. The principle image formation can easily be described by classical ray optics [40]. Usually two lenses are placed further apart than the sum of their foci. As figure 3.1 illustrates, the first lens produces a virtual image of the object within the focus of the second lens. The second lens in turn reacts as a magnifying glass and projects an inverted virtual image of the object onto the image plane.

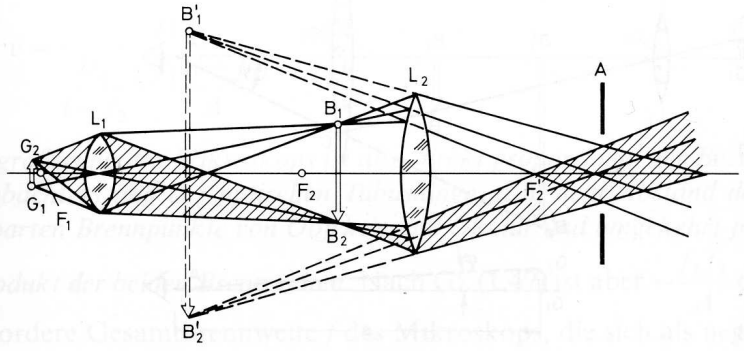

Figure 3.1: Image magnification of an object in a conventional 2-lens microscope.

In general, the pure image of the object **O** is convoluted with a transfer function **T** of the instrument.

$$\mathbf{I}(x_i, y_i) = \int_{x_o} \int_{y_o} \mathbf{O}(x_o, y_o) \bullet \mathbf{T}(x_i - x_o, y_i - y_o) dx_o dy_o \tag{3.1}$$

The above explanation of image formation in a microscope works well as long as the object is bigger than the wavelength used for illumination. Due to diffraction an optical system cannot correctly display features of very small sizes. Beyond a certain dimension the image of the object will not display its real size. Therefore it can be impossible to distinguish two very small objects, which are placed close together. In order to determine the smallest features that a classical microscope can resolve, an infinitely small object is defined and

the image that it produces is calculated.

$$\mathbf{O}(x_o, y_o) = \delta(x_o - x'_o)\delta(y_o - y'_o), \tag{3.2}$$

hence the transfer function is equal to the image that is obtained.

$$\mathbf{I}(x_i, y_i) = \mathbf{T}(x_i - x_o, y_i - y_o) \tag{3.3}$$

This transfer function characterizes the optics of the microscope and is called the point spread function (PSF). For a simple lens system the point spread function is defined as

$$PSF = \frac{2J_1(\nu)}{\nu}, \tag{3.4}$$

with $J_1(\nu)$ being the first order Bessel function and ν the Airy function.

$$\begin{aligned} \nu &= krNA & (3.5)\\ &= krn\sin\theta_0 & (3.6)\\ &= \frac{2\pi}{\lambda}rn\sin\theta_0 & (3.7) \end{aligned}$$

The width of the point spread function depends on the wavelength λ and the numerical aperture (NA) of the microscope. It can be calculated at full width half maximum to FWHM $= \frac{0.51\lambda}{\mathrm{NA}}$. In figure 3.2 a typical point spread function is plotted for intensity and amplitude signal.

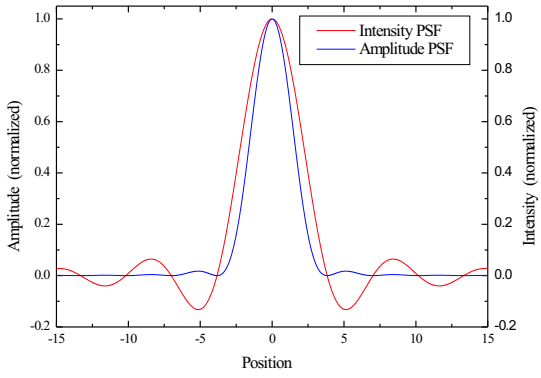

Figure 3.2: Point spread function for intensity and amplitude. The position ν is a function of the numerical aperture and the wavelength ($\nu = k\ r\ NA$).

Lord Rayleigh defined a criterion in case of incoherent illumination to determine if two small objects close together can still be separated optically. The shift between the two related point spread functions has to be so big that the intensity maximum of one PSF is placed in the first minimum of the second PSF. In this case the contrast to differentiate between the two objects is still 37.5 percent and the related distance is given by $0.61\frac{\lambda}{\mathrm{NA}}$.

For the case of coherent illumination it is also important to know the phase of the point spread functions involved. Instead of using the intensities, the overlap of two point spread functions is given by adding the amplitudes. Depending on the relative phase between the two images, it can be completely impossible to separate two objects, which would be easy to see in incoherent illumination. Diffraction experiments with optical gratings by Abbé showed that it is necessary to include at least the zero- and first-order diffraction information to image an object correctly [41]. Using the numerical aperture of the imaging system and the wavelength, Abbé's resolution criterion is given by

$$\delta x = \frac{\lambda}{2\mathrm{NA}}, \tag{3.8}$$

where δx defines the distance between two objects that can still be separated.
Confocal microscopy performs quite a bit better in terms of resolution. Here the FWHM of the point spread function is given by $\mathrm{FWHM} = \frac{0.37\lambda}{\mathrm{NA}}$. In addition, the short focal depth eliminates the influence of light outside a small volume. The lateral resolution still depends on the illumination wavelength as well as the numerical aperture and has therefore practical limitations that are typical for the above methods [42, 43].

3.2 Overcoming the resolution limit

A completely different approach for optical imaging was already taken by Synge in 1928. His suggestion was, to bring a subwavelength aperture very close to the sample that is to be examined. Light, which is penetrating through this opening, would only illuminate and interact with the small region directly underneath it. By scanning the aperture across the sample, an image would be acquired. Hence the resolution of such an imaging system would be determined by the size of the aperture rather than the employed wavelength [44]. For the first time this method was proven experimentally by Ash and Nicholls with microwaves [45] and Pohl et. al. achieved first optical images in 1984 [46]. This kind of microscope is referred to as near-field scanning optical microscopy (NSOM), due to the distinction between the electromagnetic field near the probe, which contains the information for the high resolution, and the far-field as seen by conventional microscope. For the visible wavelength region a variety of review articles are available covering a broad application range as well as the basic image formation in near-field optical

microscopy [47, 48] All the basic requirements for a near-field optical microscope are depicted in figure 3.3. For resolution beyond the diffraction limit it is necessary to have an aperture much smaller than the wavelength of light, which has to be brought in close proximity to the sample.

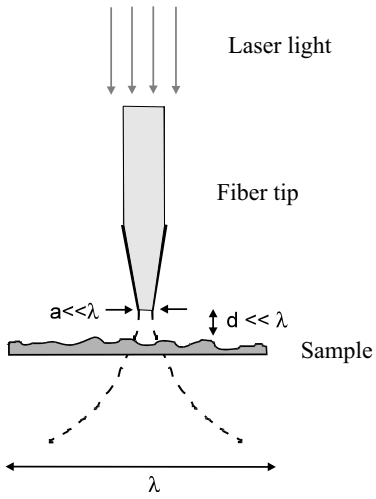

Figure 3.3: Simplified experimental set-up, illustrating an optical waveguide that is tapered down to a subwavelength aperture. The parameter d is the tip-sample distance and a is the diameter of the aperture.

The reasons for these requirements can be understood when looking at the components of electromagnetic waves. The complete information of an electromagnetic wave is expressed by

$$\overrightarrow{E} = e^{i\overrightarrow{k}\overrightarrow{r}}, \tag{3.9}$$

with $\overrightarrow{k}$ being the optical propagation vector. The requirement for $\overrightarrow{k}$ is that

$$|\overrightarrow{k}| = \frac{2\pi}{\lambda}, \tag{3.10}$$

with $\overrightarrow{k}$ being defined as

$$|\overrightarrow{k}| = \sqrt{k_x^2 + k_y^2 + k_z^2}. \tag{3.11}$$

With each component of $|\overrightarrow{k}|$ being smaller than $\frac{2\pi}{\lambda}$, the $k_{x,y,z}$ are elements of real space. But it is also possible to fulfill equation 3.11, with components being imaginary. If a wavevector-component is imaginary the resulting electromagnetic field is called evanescent and contains information from a much broader range of spatial frequencies. If, for example, the electromagnetic field is evanescent in z, $\overrightarrow{E}$ looks like

$$\overrightarrow{E} = e^{i(k_x x + k_y y) - \frac{2\pi}{\lambda'} z}. \tag{3.12}$$

Looking at the absolute values for $\overrightarrow{k}$, k^2 is

$$k^2 = \frac{4\pi^2}{\lambda^2} \tag{3.13}$$

$$= k_x^2 + k_y^2 - \frac{4\pi^2}{\lambda'^2} \tag{3.14}$$

Or, describing the ratio between the real components of $\overrightarrow{k}$ and the rest

$$k_x^2 + k_y^2 = \frac{4\pi^2}{\lambda^2} + \frac{4\pi^2}{\lambda'^2} \tag{3.15}$$

If λ' becomes much smaller than the wavelength λ, which is the case for higher spatial frequencies than permitted for a propagating wave, the above equation simplifies to

$$k_x^2 + k_y^2 \cong \frac{4\pi^2}{\lambda'} \tag{3.16}$$

As a result, $|\overrightarrow{k}|$ can still be much smaller than the sum of each component of the propagating modes, therefore containing the spatial imformation of the evanescent wave. Hence the evanescent part of the optical wave propagation vector contains all the spatial frequencies, which are not describable in real space components of $\overrightarrow{k}$.

3.3 Theoretical approximations for near-field imaging

3.3.1 Theory of Bethe and Bouwkamp

Describing the electromagnetic field analytically beyond a qualitative understanding of the power delivery through a subwavelength aperture is almost impossible due to the boundary conditions found in a somewhat realistic tip-aperture model. A general treatment by Kirchhoff's theory, where the diffracted field is expressed in terms of the incident field in the hole is not applicable for a subwavelength aperture since the boundary conditions near the hole are not satisfied. Synge's idea of an illumination source with a subwavelength spot size was first confirmed theoretically by work from Bethe, who treated the propagation of light through a subwavelength diameter hole formed in an infinitely thin, perfectly conducting screen [49]. With corrections from Bouwkamp, this approximation is solvable analytically and presents a good picture of the electromagnetic field distribution in the far- and near-field [50, 51]. Even comparison with numerical calculations of more realistic tip-aperture shapes show good agreement with analytical results from Bethe and Bouwkamp [52, 53].

Bethe's approach was to define fictitious magnetic charges and currents in the aperture, which would satisfy the boundary conditions on the metal surface surrounding the hole and give analytical solutions for Maxwell's equations. The complete derivation can be found in Bethe's and Bouwkamp's publications [49, 50].

For the analytical solution of the subwavelength aperture problem a transformation from cartesian coordinates x, y and z to oblate-spheroidal coordinates u, v and φ is performed.

$$x = a\sqrt{(1-u^2)(1+v^2)}\cos\varphi \tag{3.17}$$

$$y = a\sqrt{(1-u^2)(1+v^2)}\sin\varphi \tag{3.18}$$

$$z = auv, \tag{3.19}$$

where $0 \leq u \leq 1$, $-\infty < v < \infty$ and $0 \leq \varphi \leq 2\pi$. The parameter a resembles the diameter of the aperture. With the appropriate back-transformation in the given ranges of u, v and φ, the electric field components in cartesian coordinates are given by

$$E_x = ikz - \frac{2ikau}{\pi}\left(1 + v\arctan v + \frac{1}{3(u^2+v^2)} + \frac{x^2-y^2}{3a^2(u^2+v^2)(1+v^2)^2}\right) \tag{3.20}$$

$$E_y = -\frac{4ikxyu}{3\pi a(u^2+v^2)(1+v^2)^2} \tag{3.21}$$

$$E_z = \frac{4ikxv}{3\pi(u^2+v^2)(1+v^2)} \tag{3.22}$$

These expressions depend on the aperture diameter a and the optical propagation constant $k = \frac{2\pi}{\lambda}$ only. As an example the electric field intensity is plotted 10 nm behind an aperture of 100 nm diameter in figure 3.4. The wavelength is chosen to be $\lambda = 3$ μm and the incident light is linearly polarized along the x-axis. Notice the strong field enhancement at the edges of the metal screen for the main polarization direction.

Even though the Bethe-Bouwkamp model does not deal with a possible sample-aperture interaction, this method can be used to gain information about the microscopic field distribution after leaving the plane of the metal screen. Calculations have shown that the light passing through the aperture remains collimated for a distance approximately equal to the radius of the aperture [54]. Therefore a fiber-tip, that is hold in close proximity to a sample surface really defines the optical resolution mainly by its aperture diameter. Analysis of the throughput of a subwavelength aperture was also performed, which revealed that no propagating modes can penetrate the aperture anymore for wavelengths that are approximately three times bigger than the radius of the aperture. As a consequence all modes are evanescent and the throughput decreases with the fourth power of the tip radius.

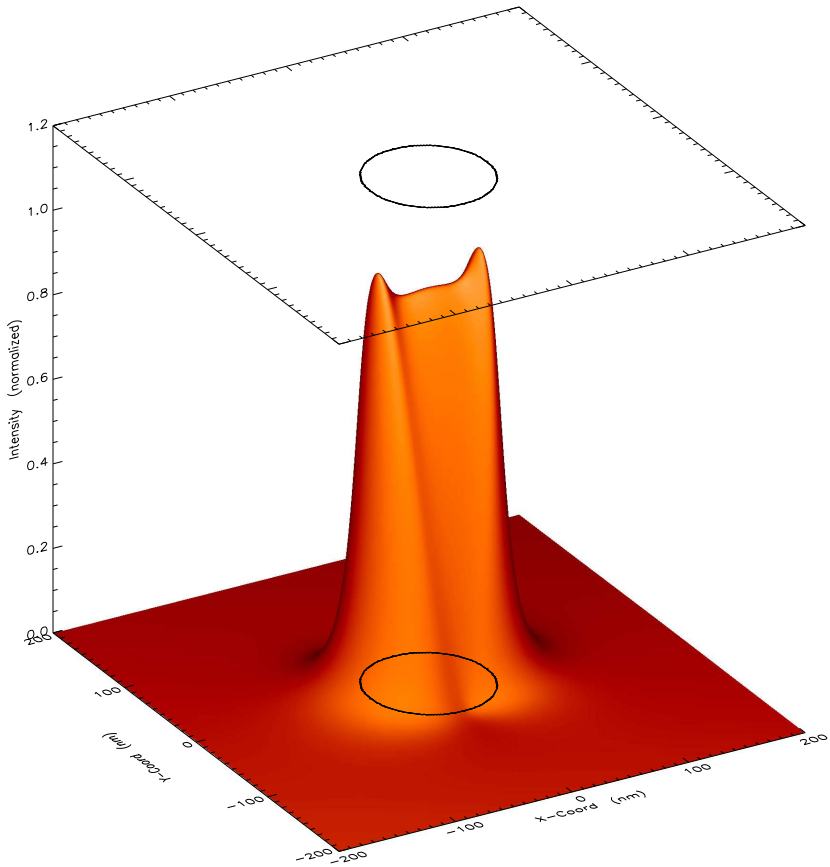

Figure 3.4: Calculation (Bethe-Bouwkamp) of the electric field intensity 10 nm away from the aperture plane. The circle in the plane of the graph represents the dimension of the aperture with a diameter of 100 nm. The wavelength is $\lambda = 3\ \mu$m.

This is certainly the case for application in the infrared wavelength range as used in this work. In figure 3.5 the electric field intensity is plotted for different tip-sample distances and shows a strong decay for the edge enhancement as well as the intensity measured in the center of the aperture.

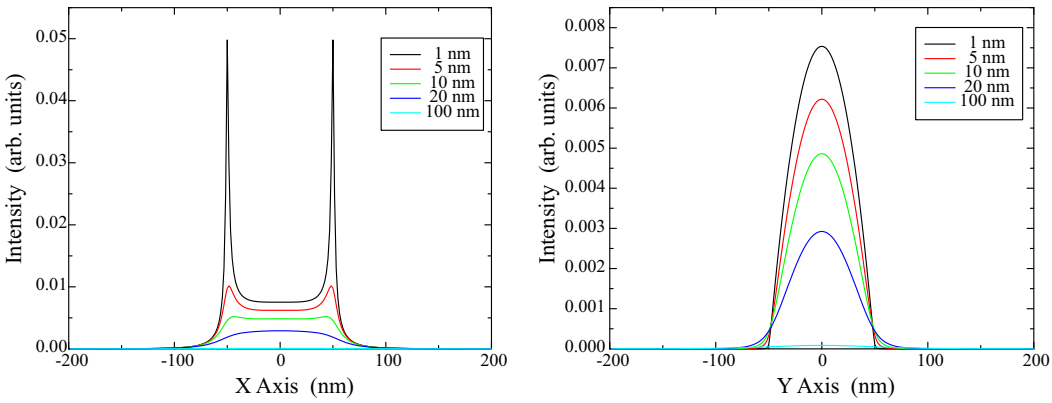

Figure 3.5: Electric field intensities for different gap sizes between tip and sample (Bethe-Bouwkamp model). The incoming light is linearly polarized along the x-axis.

The distance dependent decay is also illustrated in figure 3.6, following a first order exponential law with a 1/e drop-off of 20 nm. The calculations were performed in the center of the aperture since in this case the direction of the pointing vector of the electromagnetic field is normal to the surface and contributes most to a near-field optical signal on a far-field detector.

3.3.2 Multiple multipole approximation (MMP)

Since analytical solutions are not available for more realistic tip shapes and especially for more complicated situations, as for example the tip-sample interface, numerical methods have been employed in the literature to simulate dielectric fiber-tips and their interaction with sample structures. Many of these results provide a more complete picture to image formation in near-field optical microscopy but also show that the above demonstrated Bethe-Bouwkamp approximation is a very good model for the electromagnetic field of an unperturbed near-field optical probe [55, 56].

One class of numerical methods is based on matching boundary conditions at interfaces [57]. The object of interest is divided into small pieces, where each is describable by analytical solutions based on their local boundary conditions. Matching the boundary

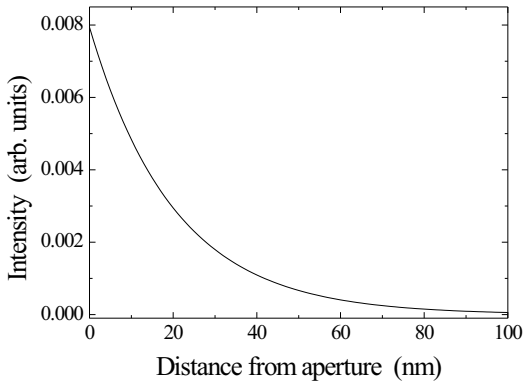

Figure 3.6: Exponential decay of the intensity after exiting the aperture (Bethe-Bouwkamp model). The intensity drops to 1/e of its original value after 20 nm.

conditions with all neighboring fractions gives the macroscopic field distribution of the object. Inside each domain, the field is approximated by a series expansion, which takes the generic form

$$E(r) = E_0(r) + \sum_k c_k f_k(r - r_k). \tag{3.23}$$

The functions f_k are analytical solutions to the Maxwell/Helmholtz equation

$$(\nabla^2 + k^2) f_k(r) = 0. \tag{3.24}$$

These basis functions can be waveguide modes, plane waves or evanescent waves. In the multiple multipole technique, the basis functions are multipoles, which are solutions to the Helmholtz equation in either cylindrical or spherical coordinates. The coefficients c_k are determined by matching the expansions from adjacent domains at discrete points along the domain interface. The multipole functions used as the basis set are of short range and therefore only affect their immediate neighbors significantly. This makes them useful in modelling more complicated structures, since regions, which would otherwise be unsolvable analytically due to discontinuities, can be approximated by small domains, that are only in communication with their direct neighbors. This makes the multiple multipole approximation an useful tool to model more realistic near-field optical probes and also investigate the electric field distortions during tip-sample interaction as can be found in quite a few publications [52, 57, 58].

3.4 Apertureless near-field optical microscopy

3.4.1 Dipole induced dipole interaction

A completely different approach to overcome the resolution limit is taken by scattering type or apertureless near-field optical microscopy (ANSOM). This method was introduced first by Wickramasinghe et. al. in 1995 [59]. In this case light is not guided through a subwavelength aperture but instead is focused on a sharp, pointy probe, which is in close proximity to the sample. This probe acts like an antenna and incoming light induces a dipole field, which in turn interacts with the sample substrate. For long and sharp antennas a confinement of high energy densities is reached at and nearby the end of the probe and therefore allows to observe localized interaction with the sample. Hence the lateral resolution of such an instrument would mainly be determined by the sharpness and shape of the probe.

By using the electromagnetic field from an antenna to probe the sample rather than the incoming light, a small "light source" is introduced, that interacts very localized with the sample. The back-scattered light is then collected in the far-field by diffraction limited optics. Changes in the scattering intensity give the optical contrast, while the antenna is scanned with respect to the sample. Figure 3.7 illustrates the basic principle of this method. Special notice has to be taken regarding the polarization of the incoming light [60]. An effective coupling between antenna and sample is only possible, if the illuminating laser beam has an electric field component, that is oriented along the main axis of the antenna. For the dipole excitation it would be best to have vertically polarized light coming in parallel to the sample surface, so the poynting vector of the electromagnetic field is vertical to the main axis of the probe. There are a few disadvantages related to this set-up. Since the probe does not have an overall diameter, that is small compared to the focal spot, an asymmetric excitation is observable, which leads to tip-sample interaction at other places than the end of the probe. For good excitation of the dipole it is necessary to concentrate as much light as possible at the very end of the antenna. This can only be reached by a very small focal spot as given by optics with a high numerical aperture (NA). Since the NA gives the ratio between the diameter of the lens system and its focal length, high NA optics have to be mounted very close to the probe. With the sample and the probe holder already being in close proximity, it is almost impractical to fit a high NA objective in the set-up. For the reasons above, the antenna was illuminated through the sample as depicted in figure 3.7. Now very high NA optics could be employed, since the sample thickness is the only distance limiting factor in such a set-up. Concerning the excitation of the antenna dipole, the main direction of the poynting vector is parallel.

Due to focussing of the laser beam, the light has a strong electric field component parallel to the antenna, which is responsible for the dipole excitation.

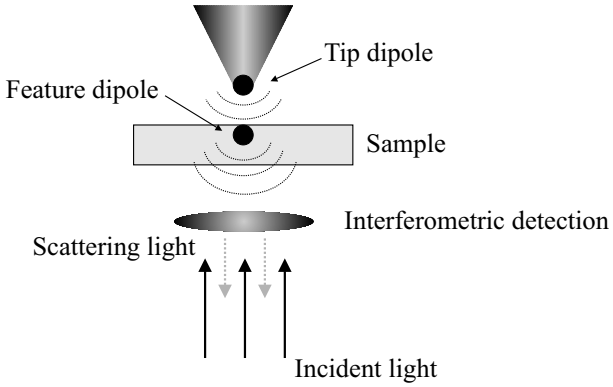

Figure 3.7: An AFM tip resembles the antenna, which is brought in proximity to the sample. Incident laser light induces a dipole field, which in turn produces a mirror dipole in the substrate. Depending on the local polarizability of the sample, changes in the far-field scattering of the tip can be observed.

In experimental realization the probe is mostly made out of cantilevers used in atomic force microscopy (AFM). AFM tips can be manufactured with tip curvatures as small as a few nanometers, providing the sharp scattering center that is needed to confine the electromagnetic fields. At the same time the AFM mechanism allows the distance between tip and sample to be kept constant, which is important due to the nonlinear distance dependence of the optical dipole. For the distance measurement the tip probes the Van-der-Waals interaction by dithering vertically in and out of the field described by the Lennard-Jones potential. Damping of the dither amplitude indicates the height over the surface and with help of a feedback system can be locked to a steady value (see the experimental section as well).

The contrast mechanisms in apertureless near-field optical microscopy can be understood qualitatively by treating the tip-sample interaction as dipole-dipole coupling [61]. As first order approximation the tip and the sample features can each be modelled as a sphere. This assumption is acceptable considering the strong distance dependence of the optical dipole interaction, which decays with $1/\mathrm{d}^3$. Therefore contributions from interaction regions that are farther apart than the closest distance between sample and tip have rapidly decaying influence and can therefore be neglected. The scattered electric field E_s of the tip depends on the incident field E_i as follows:

$$E_s = E_i k^2 \frac{\chi}{4\pi}, \tag{3.25}$$

where $k = \frac{2\pi n}{\lambda}$ is the optical propagation constant (wave vector) and χ the susceptibility

of the sphere given by

$$\chi_{\parallel} = 4\pi a^3 \frac{(\epsilon^2 - 1)}{(\epsilon^2 + 2)} \cos\theta \tag{3.26}$$

$$\chi_{\perp} = 4\pi a^3 \frac{(\epsilon^2 - 1)}{(\epsilon^2 + 2)} \tag{3.27}$$

Here, ϵ is the complex index of refraction of the sphere, a represents the radius of the sphere, while the susceptibility χ depends on the polarization of the incident electric field relative to the scattering angle θ.

Since the optical signal is collected in the far-field, scattering theory provides an expression for the electric field, which depends on the polarizability modulation $\triangle\alpha$.

$$E_{scatter,far} = \frac{2\pi n^2}{\lambda^2 d_{far}} \triangle\alpha \tag{3.28}$$

Tip and sample each have their own material dependent polarizabilities. Upon approach of the two, a common polarizability $\triangle\alpha$ results from the coupling of probe and sample dipoles.

$$\triangle\alpha = \frac{2\alpha_{tip}\alpha_{sample}}{(d^2 + a^2)^{\frac{3}{2}}}, \tag{3.29}$$

With α_{tip} and α_{sample}, the individual polarizabilities are used to express the common polarizability as seen in the far-field. Parameter d represents the distance between the two objects and a the radius of the spheres. The polarizabilities can also be expressed through the susceptibilities (equation 3.26/3.27) instead. For the approximation of spheres, α is

$$\alpha = \frac{\chi}{4\pi}\left(\frac{4}{3}\pi a^3\right). \tag{3.30}$$

Even though the modelling of the tip and the sample as two communicating spheres is a very simple approximation, it becomes quite obvious from the above calculation, that the resulting electric field is strongly distant dependent. Therefore the probe has to be kept in very close proximity to the sample to detect any light modulation that is related to direct tip-sample interaction. With detectors measuring intensity variations rather than electric field amplitudes, the intensity is proportional to the inverse sixth power of the distance.

3.4.2 Artifact reduced optical imaging

One of the major drawbacks in near-field optical microscopy is the great crosstalk between topographic and optical signal. As shown for the aperture-based as well as

the apertureless near-field optical microscope, the electromagnetic coupling of tip and sample is strongly dependent on the distance between them. Hence it is important to keep the tip-surface gap constant, so changes in the optical signal can be related to optical contrast rather than variations in topography. Still it is not possible to completely avoid influences from topographic features due to finite dimensions of the probe. Therefore it becomes necessary to differentiate topographically induced artifacts in the optical signal from true optical contrast [62]. Fukuzawa et. al. developed a set-up, that would dither the tip and the sample in a horizontal and a vertical direction at different frequencies, thus allowing heterodyne detection of the tip-sample interaction [63].

One possibility to minimize the influence of topographical variations on the optical signal is to utilize the nonlinear distance dependence of the optical interaction [64, 65, 66]. With the sinusoidal modulation of the tip-sample distance, the nonlinearity implies that the scattering signal will be an anharmonic modulation of the dither frequency. As a result higher harmonics are efficiently produced in the optical modulation.

$$A(t) = A_0 + A_1 \cos(\omega t) + A_2 \cos(2\omega t) + \dots \tag{3.31}$$

Hence a detection at a higher harmonic than the driving modulation of the cantilever will mainly contain contributions from the nonlinear tip-surface interaction. As it is already visible in figure 3.7, the incoming light will not only be scattered by the tip but also be reflected back from horizontal interfaces at the sample. This leads to a strong background, which will interfere with the backscattered light from the probe, causing it to be the biggest part in unwanted artifacts upon topographical changes. In the following estimates are made, when a higher harmonic detection will be advantageous.

At first a function K is defined, which resembles the nonlinear behavior of the optical signal.

$$K\big(z(t)\big) = e^{-\frac{z(t)}{d}} \tag{3.32}$$

with d being the average tip-sample distance and $z(t)$ the modulation of the AFM cantilever at the amplitude A

$$z(t) = A\cos(\omega t). \tag{3.33}$$

The main artifact is induced by optical interference of the backscattered light of the tip with that from the sample surfaces. It can be described by

$$W\big(z(t)\big) = \sin\left(\frac{4\pi z(t)}{\lambda} + \frac{\pi}{4}\right). \tag{3.34}$$

The phase shift $\frac{\pi}{4}$ displays the worst-case scenario of interference of the surface backreflection with the scattering signal. Small modulation in topography will result in a maximum change in signal. So the signal function of the instrument is the sum of both effects:

$$S(t) = W(t) + \gamma K(t) \tag{3.35}$$

with γ being the weight of scattering contributions.
This function can be expanded in series for small A with $t_0 = 0$.

$$S(t) = \underbrace{\left(\frac{1}{\sqrt{2}} + \gamma\right)}_{const} + \underbrace{\left(\frac{4\pi}{\sqrt{2}\lambda} - \frac{\gamma}{d}\right) A\cos(\omega t)}_{1.harmonic} + \underbrace{\frac{1}{2}\left(-\frac{16\pi^2}{\sqrt{2}\lambda^2} + \frac{\gamma}{d^2}\right) A^2\cos^2(\omega t)}_{2.harmonic} + \ldots \tag{3.36}$$

The expansion was done up to the second order, where the first order term resembles the signal at the tip resonance ω and the second order term likewise at 2ω. In each case we can separate the near-field and the artifact contribution and compare their magnitude with respect to each other. The near-field expression for first harmonic is simply $\frac{\gamma}{d}$, with the term $\frac{4\pi}{\sqrt{2}\lambda}$ being the interference signal. Similarly $\frac{\gamma}{d^2}$ is the near-field term for the second harmonic term and $\frac{16\pi^2}{\sqrt{2}\lambda^2}$ is the artifact contribution. The ratios between interference and tip scattering are as follows.

$$R_1 = \frac{\sqrt{2}\lambda\gamma}{4\pi d} \tag{3.37}$$

$$R_2 = \frac{\sqrt{2}\lambda^2\gamma}{16\pi^2 d^2} \tag{3.38}$$

To evaluate under what conditions the use of second harmonic detection is beneficial, R_2/R_1 is calculated.

$$\frac{R_2}{R_1} = \frac{\lambda}{4\pi d} \tag{3.39}$$

Hence demodulation at twice the driving frequency will yield more scattering signal compared to the inherent background than the first harmonic, if the tip-sample distance d is smaller than $\frac{\lambda}{4\pi}$, which is usually the case. In the experimental section, apertureless NSOM measurements were performed at the driving resonance as well as twice the tip modulation.

4 Lithographic sample preparation

4.1 Structuring by mask

The general method used to transfer a predefined pattern onto a substrate is by physically masking areas of photosensitive polymers, which are spin-coated on the surface of the sample. Masks are usually made of chromium, which contains the desired pattern. In figure 4.1 a typical flow-chart of the photolithographic process as it is used for semiconductor manufacturing is presented. In a first step a thin uniform film of photopolymer resist is coated on the substrate. In the exposure step, the photosensitive material is illuminated through the mask by an ultraviolet light source, which causes local chemical changes due to photolysis. Now either the chemically altered material or the opponent can be removed by a matching solvent in the development step. In a following etching process, the areas, which are unprotected by polymer can be etched and therefore the pattern is transferred into the sample plain.

Since this method is diffraction limited, the wavelength of the light source is directly correlated with the smallest possible feature size. Typically excimer lasers are used at wavelengths of 248 nm and 193 nm. New approaches are made to utilize UV light at 157 nm. In the case of these experiments the light of a doubled Ar^+-laser was used to produce features size down to 1 μm.

The mask patterning is divided into three different modes of operation. The chromium mask is either attached directly to the surface of the photosensitive polymer, which is called the "contact mode" and provides sharp images in the photoresist. The difficulty with this method is, that damage of the polymer and the substrate can occur upon removal of the mask. In order to avoid the physical impact on the resist, a second method was established, called "proximity mode". In this case, the chromium mask is brought in close distance to the surface, with typically a few hundred nanometers in between. Now the mechanical damages are avoided, but the images in the photoresist appear blurred. Hence feature sizes can not be as small as in contact mode. A third alternative is usually employed for the manufacturing process, which is named "projection mode". Here the light passes through the chromium mask first, with the image of the mask being projected onto the photoresist through a sophisticated system of high-quality optical lenses ("stepper").

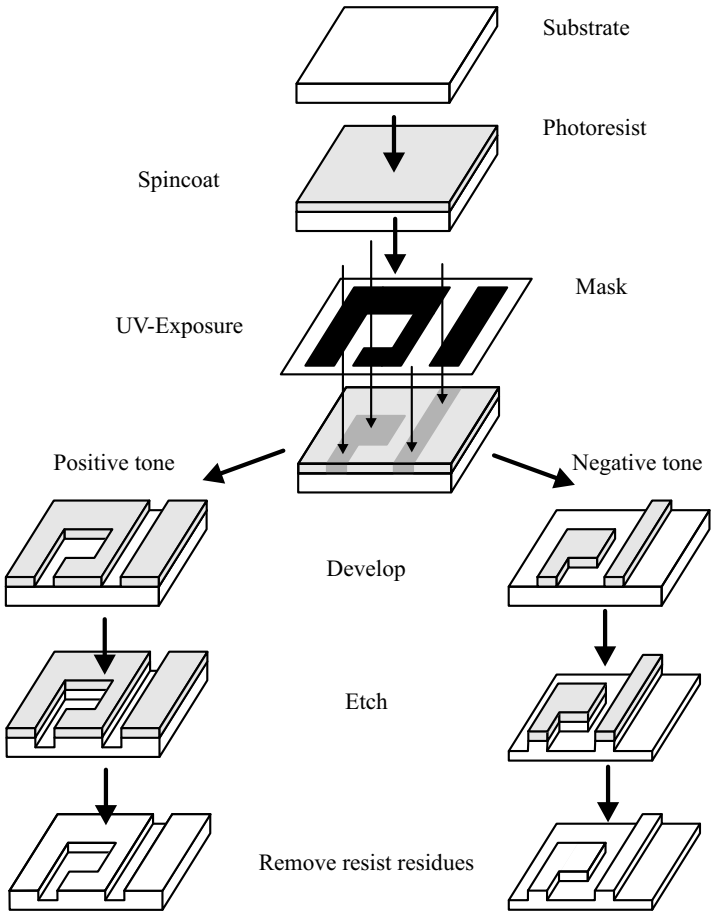

Figure 4.1: Photolithographic process

For the sample preparation of mask-patterned structures the contact mode was used and resulted in fairly good reproducibility at least in the small areas, that were examined.

The main focus of this work is the characterization of the exposure/development step and especially the properties of a new class of photoresists used in the photolithographic process. With the employment of chemically amplified photopolymers, the development process requires the substrate to be heated in order to provide energy for the necessary deprotection. For mask patterned samples these bake times were usually set at 90 seconds, while the exposure dose was varied to see changing influences of the UV light intensity.

4.2 Structuring by interferometric lithography

Another way of writing a pattern onto a substrate is given by interferometric lithography. Even though this method is - in its most basic set-up - only capable of writing periodic line structures, these structures can be very small, very accurate and highly reproducible [67]. With these advantages, interferometric lithography is very valuable for basic research and can be used to understand fundamental issues in photolithographic resists.

In interferometric lithography a standing wave pattern is produced by interference of two coherent light beams. A substrate that is coated with a photoresist is positioned in the overlap of the two beams and is exposed to the intensity pattern, that results from the interfering light sources at the surface of the substrate (figure 4.2). The periodicity P of the line pattern is determined by the wavelength of the light source λ and the angle θ, which describes the intersecting angle of the two beams.

$$P = \frac{\lambda}{2} \sin\theta \tag{4.1}$$

The optical pattern, that is produced on the surface of the substrate from an above illumination set-up can be analytically described. Assuming that both beams, that are brought in overlap, have gaussian intensity distribution, the local intensity $I(x)$ in the plain of the overlap is

$$I(x) = \sin^2\left(\frac{2\pi \sin(\theta)}{\lambda} x\right) e^{-\left(\frac{x}{A}\right)^2}, \tag{4.2}$$

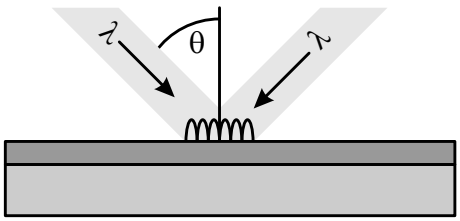

Figure 4.2: Two coherent beams are overlapped on the substrate to produce an interference pattern in the photoresist.

with A being the width of the gaussian beams, θ the intersecting angle and λ the UV wavelength.

The main requirement for the sample preparation is the need for a coherent light source in the UV wavelength range. In figure 4.3 the set-up used for the samples in this work is shown. It utilizes the output of an argon ion laser ($\lambda = 515$ nm) in an external cavity with a frequency doubling crystal (ADP) to produce coherent UV light at $\lambda = 257$ nm. Maximum output powers of 2 mW could be reached. It is also important to preserve the gaussian mode structure of the argon ion laser during the doubling. This helps to later identify the differently exposed regions on the samples. After splitting the UV beam in two equally bright parts, they are brought in overlap on the surface of the substrate. With the help of the attenuator in one of the two beams, the depth of intensity modulation could be varied if needed.

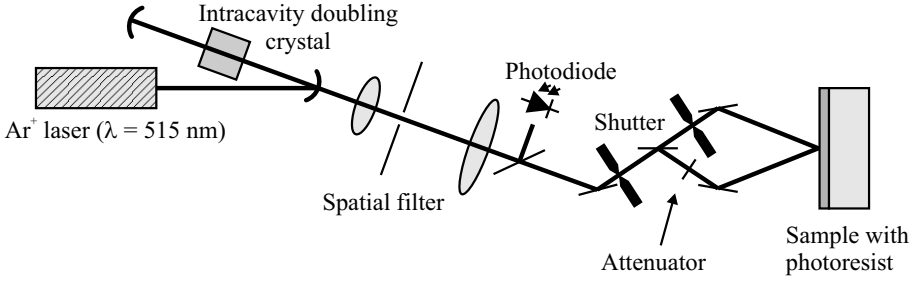

Figure 4.3: Set-up to irradiate the photoresist coated substrate with UV light ($\lambda = 257$ nm).

With an intersecting angle θ of 7.6 degree, the periodicity of our samples came out to be 972 nm. Due to volatile compounds in the deprotected features, shrinkage occurs, which can be mapped topographically. In figure 4.4 an AFM image shows a 5 μm $\times$ 5 μm topography scan of one of the samples used. The maximum UV intensity during illumination was 2.3

mJ/cm^2 in this section of the sample. The post exposure bake time was 90 seconds. The line scan in figure 4.5, which was taken from the x-plane of the AFM image illustrates the narrow valley and unproportionally wide plateau as an indicator for broadening effects that are happening during the deprotection process.

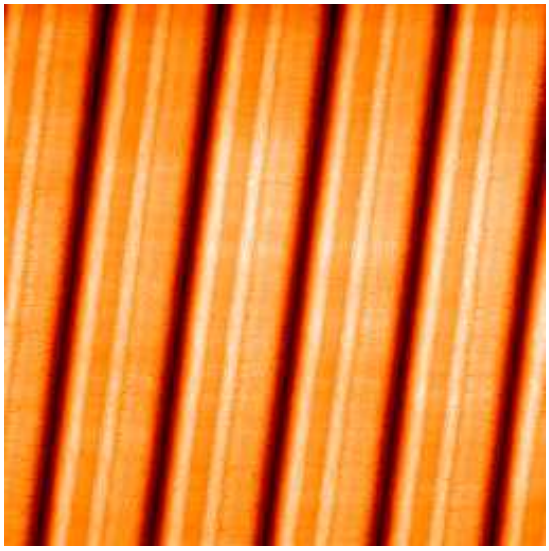

Figure 4.4: AFM image of developed PT-BOCST sample 5 μm × 5 μm, 90 sec PEB, UV intensity was 2.3 mJ/cm^2.

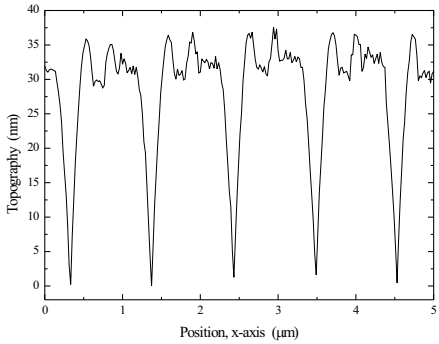

Figure 4.5: Linescan from the x-plane of the AFM image.

5 Infrared near-field optical microscopy

5.1 Set-up

The set-up for a near-field optical microscope consists basically of three major parts.

In the optical realm a subwavelength aperture has to be build, which can deliver enough light close to a surface, so measurable interaction with the sample can be observed. Hence, also special care must be given to collect as much light as possible from the interaction region. And the third task is to provide a mechanism, that keeps the aperture in close proximity to the surface at all times, combined with a sturdy design to allow repeatable resolution in the range of a few ten nanometers. Figure 5.1 shows the elements of the design used for the following experiments.

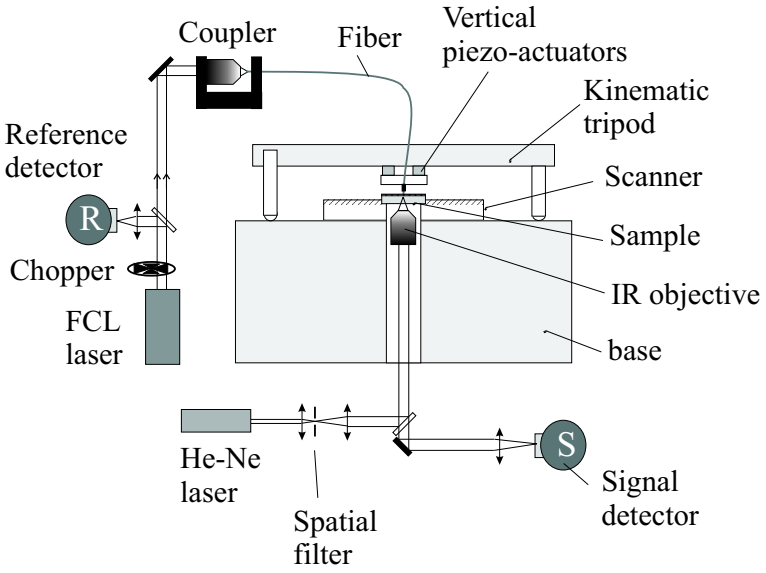

Figure 5.1: Schematic of experimental set-up. The reference and the sample signals from the pinhole detectors R and S are fed to the differential input of a lock-in amplifier, which is locked at the chopper frequency (1 kHz). The numerical aperture of the IR objective is important for establishing the contrast mechanism. The spatially filtered He-Ne laser beam is used as a pilot beam for alignment, as well as for confocal reflection microscopy.

On the left of figure 5.1, the incoming light from a laser source is depicted as it is coupled into an optical waveguide. The waveguide is tapered down to a small aperture, which is mounted on a kinematic tripod, thus allowing the precise vertical positioning of the

aperture relative to the base underneath. The base consists of a commercially available XYZ-scanning stage (Physik Instrumente, PI) and is used to scan the sample relative to the aperture. The stage is piezo-driven and has a reproducible resolution of less than 1 nm due to a capacitive-based feedback control. The light exiting the aperture is collected in the far-field by an objective, which is part of a confocal collection beam path, that guides the light from the interaction volume to a detector. Depending on the wavelength experiments were performed with different objectives of varying numerical apertures. For infrared experiments ($\lambda \sim 3$ μm), special objectives had to be used, which show transmittance in this wavelength range. In principle, reflective and refractive objectives can be used for infrared light collection. Refractive objectives are usually based on calcium fluoride, but can only be build for small numerical apertures, due to the index of refraction of the lens material. Another disadvantage are the losses due to absorption in the objective, which decreased the transmittance for the wavelength range used ($\lambda = 3$ μm) to less than 90 %. Reflective objectives, most commonly known as cassegrain objectives, are build of two spherical mirrors, which focus the light in a similar way as a lens system. The advantage of relying on surface reflection rather than transmission through material is two-fold. First, the throughput of such an objective can be much bigger, since no losses due to absorption are apparent. The second advantage is the absence of chromatic abberation in the objective. As disadvantageously is to mention the obscuration of the light due to the second mirror placed in the beam path. Also the mechanical dimensions make it difficult to simply replace refractive objectives by reflective ones.

The collection beam path was designed in a confocal way by focussing the light through a pinhole onto the detector. In this way the collection volume of the detector is restricted to the confocal volume on the sample. Hence, scattering from other places than the aperture was avoided, improving the signal-to-noise ratio of the detection path enormously.

Implemented in the microscope was also a reference system for the laser output. By subtracting the reference signal of the laser before entering the fiber from the signal observed by the detector at the end of the collection beam path, the influence of laser fluctuations could be reduced.

The electrical layout is shown in figure 5.2. The scan-stage was controlled by a computer, which allowed to move to any point in a 100 μm $\times$ 100 μm area and obtain images by moving the probe across the sample and sequentially recording data points. Two signal channels delivered information about the current height of the probe above the

sample and about the light reaching the detector and were stored and plotted on the screen instantaneously. For the optical output signal recovery was obtained by employing lock-in detection. Therefore the incoming optical light had to be modulated, here done mechanically with a chopper wheel at typically 300-1000 Hz. The lock-in amplifier was also used to subtract the reference signal from the near-field optical signal.

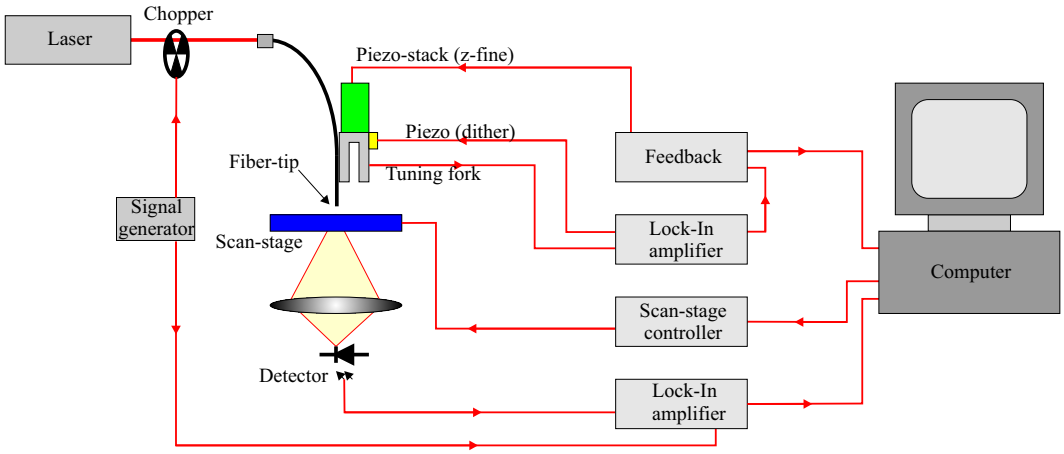

Figure 5.2: The electrical layout of the scanning near-field optical microscope.

As pointed out in section 3.3 the interaction of the electric field strength between sample and probe has a highly nonlinear distance dependency. Therefore it is necessary to keep the sample-probe distance constant and the tip in close proximity to the surface. Several methods have been established for distance control in near-field optical microscopy in the past and almost all of them utilize Van-der-Waals interaction between tip and sample [68, 69, 70, 71], which is described by the Lennard-Jones potential

$$U(r) = 4\epsilon\left(\left(\frac{\sigma}{r}\right)^{12} - \left(\frac{\sigma}{r}\right)^{6}\right). \tag{5.1}$$

The Lennard-Jones potential consists of an attractive long range part and a very short ranged repulsive one. Figure 5.3 depicts qualitatively the potential as a function of distance. As in AFM, the Van-der-Waals forces are probed by dithering the tip at its mechanical resonance. The attractive part of the Lennard-Jones potential leads to a gap-dependent damping of the dither amplitude, which can be used as a measure for the distance above the surface. While the AFM cantilever is generally dithered in a vertical direction and therefore probes the Van-der-Waals interaction by dipping into the potential, in near-field optical microscopy this is not applicable. The fragile fiber tip would break immediately upon touching the surface. Instead the fiber is dithered horizontally above the surface, which still leads to an attenuation of the dither amplitude due to shear-force

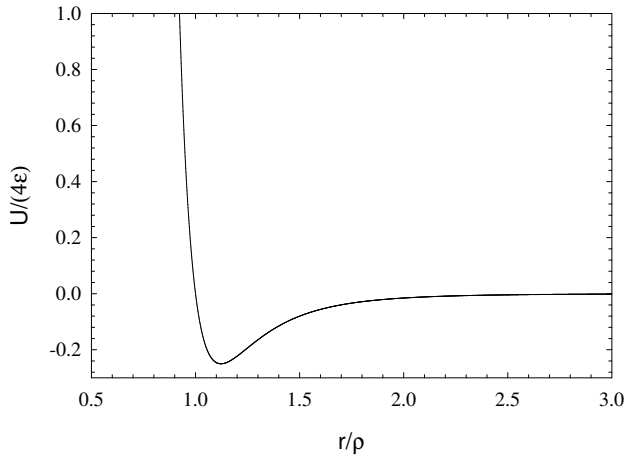

Figure 5.3: Lennard-Jones potential (normalized)

interaction. The interaction range depends on the strength of the dipole moments of the molecules that are present. Since, for example, water has a strong dipole coupling, the Van-der-Waals forces will be measurable over a range of up to 100 nm. Under ambient air conditions the observed range was usually between 5 and 20 nm.

For the set-up the experimental challenge is to detect dither amplitudes that are small compared to the desired optical resolution. With typical apertures of 100 to 200 nm the mechanical dither amplitude cannot exceed more than a few ten nanometers without influencing the optical resolution.

The excitation of a lateral oscillation is easily done by small piezo crystals, that are electrically driven by a function generator at the mechanical resonance of the fiber probe. The detection of the damping of the amplitude is based on the inverted piezo effect and utilizes a commercially available tuning fork piezo based crystal as used in clocks and timers [72]. The crystals are packaged in small aluminum cans, which can be crushed carefully with a vice such that the bare tuning fork can be mounted directly. After gluing the tuning fork onto a macor holder, which resembles the head of the microscope and connecting the two electrodes the quality factor Q is usually measured to be 5000 to 7000. Using a cyano acrylate based adhesive the fiber is glued to one prong of the tuning fork with the tip reaching beyond the end of the fork only a few hundred micrometers. This

way the tip resonance frequency is strongly coupled to the tuning fork resonance, shifting it barely by a couple hundred hertz. Due to the attached fiber and the glue, the Q-factor typically drops to a value of 100 to 300.

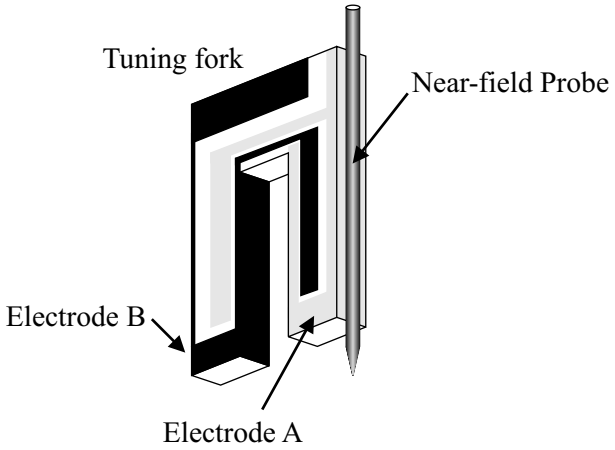

Figure 5.4: A quarz tuning fork is used to detect the lateral fiber motion. The metal coated fiber with the tapered end is glued to one of the prongs of the fork. The piezo voltage can be measured by attaching wires to the electrodes.

Feeding the signal into a second lock-in amplifier allowed detection of dither amplitudes as small as 5 nm. A calibration was obtained by the assumption that the amplitude changes linearly with the applied piezo voltage, which is a good estimate for excitation amplitudes that are small compared to the length of the dithering fiber. For higher voltages (up to 30 V) the dither amplitude could be detected and measured by a conventional microscope optic. Extrapolation of the voltage for small excitations allows the determination of the above number ($\pm$ 2 nm). Scanning a sharp topographic edge confirmed at least the order of magnitude for the dithering range. The output of the lock-in amplifier gives a DC voltage, that is proportional to the amplitude of the dithering fiber tip. Therefore, damping of the oscillation results in a smaller value at the amplifier. A feedback system was now employed to keep the amplitude of the damped oscillation constant, therefore restricting the tip aperture to a constant distance above the sample surface. With the feedback bandwidth much higher than the scanning rate, the constant tip-sample gap was always assured during the scans.

5.2 Fiber tip preparation

5.2.1 Overview

In near-field scanning optical microscopy one of the challenges is to produce a subwavelength aperture that can be brought in close proximity to the sample. The common approach chosen and described in literature is to taper an optical fiber down to a sharp tip of a few nanometer diameter and then coat the fiber taper with a suitable metal. The deposition angle is set off-axis to the fiber, such that the end of the tip is not coated by metal and therefore leaves a small hole for light to penetrate.

5.2.2 Fiber taper preparation by melting/pulling

The taper of the fiber is usually achieved by applying a mechanical pulling force on both ends of a bare fiber and then melting the fiber by a powerful CO_2-laser ($\lambda = 10.6\mu m$). The mechanical force draws both ends of the fiber apart, leaving two cone shaped fiber tips (figure 5.5). The shape of the taper depends on the melting properties and viscosity of the fiber material as well as the diameter of the fiber. By adjusting the laser intensity, the pulling force and velocity one can influence the shape of the fiber tip. A convenient way of controlling all the parameters above is given by utilizing a commercially available micro pipette puller. With this apparatus fiber tips can be produced under repeatable conditions. In the case of this work the micropipette puller model P87 manufactured by Sutter Instruments was used together with a 40 Watt CO_2-laser from Syncrad. Depending on the fiber material only a fraction of the power was needed to actually melt the fiber. For fiber pulling, the power of the CO_2-laser was usually set around 600 mW with a focus diameter at the fiber of about 1 mm. The settings for pulling velocity and force varied widely depending on the fiber diameter and materials.

5.2.3 Fiber taper preparation by etching

Another method of manufacturing fiber tips is to etch the fiber core in a suitable solvent [73, 74]. The fiber core is simply dipped into the solvent, usually a strong acid, which has an organic buffer layer on top. The reason for the buffer layer is twofold. For once it simply prevails the solvent from crawling up the fiber. On the other hand it provides a clear horizontal barrier for the etching process. This is important to establish a convectional flow of the etching solvent as shown in figure 5.6. Used solvent (close to the fiber)

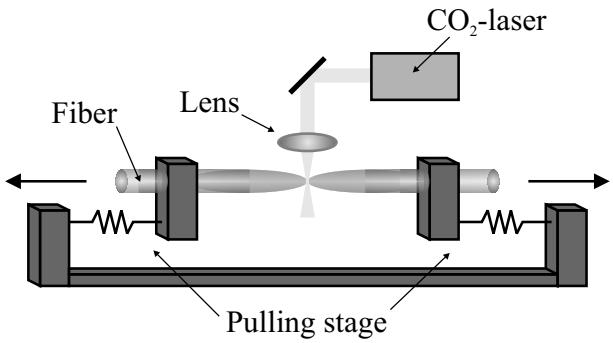

Figure 5.5: Tip preparation by fiber pulling. An optical waveguide is mounted under tension and heated to its melting point. The counteracting mechanical forces draw the fiber apart and leave the fiber ends tapered to small cones.

is floating to the bottom while being replaced by fresh solvent. This leads to the fastest etching rate near the top interface, which is given by the buffer layer. As a result the fiber will develop a wasptail, which eventually leads to dropping of the bottom part of the immersed fiber, leaving a tip with a big taper angle.

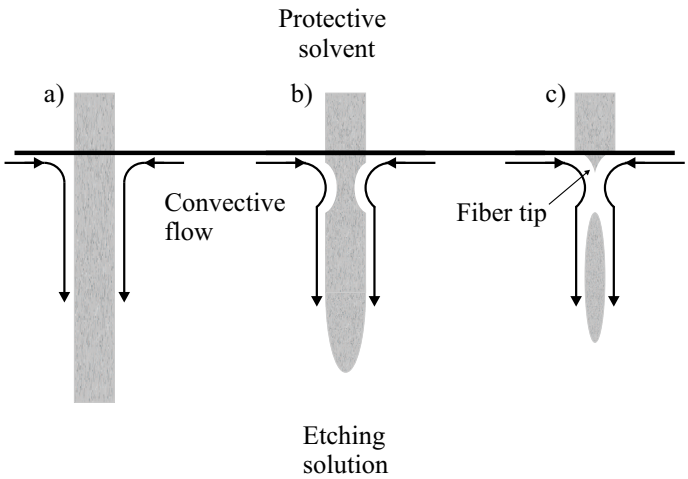

Figure 5.6: Etching of fiber tip: a) the fiber is immersed in the etching solution, b) due to convection a neck is forming near the etchant/protection interface, c) the faster etching process at the neck results in drop-off of the remaining material, leaving a sharp tip just below the interface.

5.2.4 Aperture formation by deposition of metal coating

Since a bare fiber taper will not guide the light sufficiently it is necessary to provide a coating of the taper that confines and delivers the light to the very end of the tip. This is achieved by coating the taper with a thin metal layer. By choosing an off-axis angle for the incident deposition beam, the tip end will not be coated with metal and leave a round aperture, which represents the near-field probe as illustrated in figure 5.7.

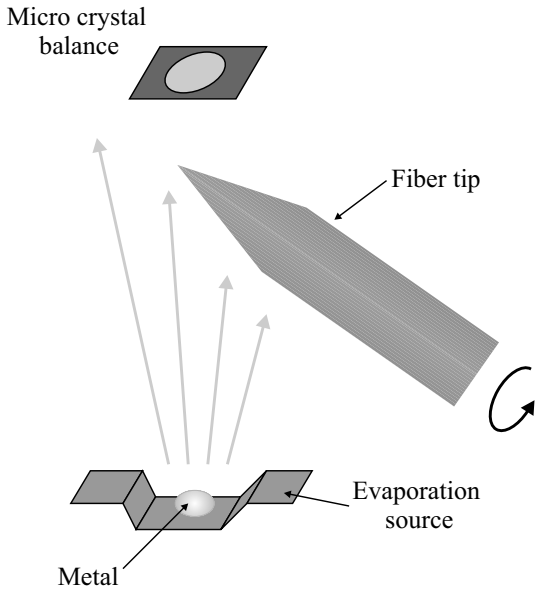

Figure 5.7: The evaporation source deposits metal under an off-axis angle onto the rotating tip. By shading, metal cannot reach the far end of the tip, leaving a small aperture. The evaporation parameters are monitored by a micro crystal balance.

The minimum thickness for the deposition is determined by several factors. Most importantly each metal has a wavelength dependent skin depth, defined as the thickness, that is needed to extinct 63 % (1/e) of the incoming light. Another aspect for the chosen thickness of the coating is the initial surface roughness of the fiber material as well as the tendency of each metal to form grains. The coating has to be thick enough to cover all nonuniformities and corrugations of the surface, so that no light can penetrate. Finally the metal has to have enough adhesion to bond well with the waveguide material. This also leads to a mechanical stabilization of the fragile fiber tip and makes it less vulnerable to mechanical impacts. In the following table the skin depths are listed as calculated for aluminum, gold and chromium at the two wavelengths, that were used in this work.

	Al	Au	Cr
Skin depth (nm) at $\lambda = 633$ nm	6.7	15.9	11.5
Skin depth (nm) at $\lambda = 3000$ nm	7.6	11.5	26.6

Empirically it was found that a layer of about 30 nm of aluminum will provide sufficient shielding to deliver almost all the light to the aperture. During the coating process a fast deposition rate of several nanometers per second was used to avoid the formation of islands on the surface. Since aluminum does not stick very well on glassy materials, we used a 20 nm thick deposition of chromium as an intermittent layer.

During the process of adjusting the parameters, which influence the taper formation as well as the metal coating, fiber tips are imaged by scanning electron microscopy (SEM) to determine the shape of the taper and the quality of the aperture. The fiber tip quality can also be analyzed prior to employing the probe in the near-field optical microscope by studying the diffraction pattern of 633 nm wavelength light emerging from the aperture under a conventional microscope. The tip is mounted so that the aperture is facing the collection objective. The spatial resolution of the microscope in this case is 460 nm. While this resolution is not enough to monitor the aperture directly, a perfectly round, subwavelength aperture produces a pattern that is described by the Airy function. Leakage through the coating or aperture imperfections, even if not resolved, leads to distortions of the Airy disk pattern (figure 5.8).

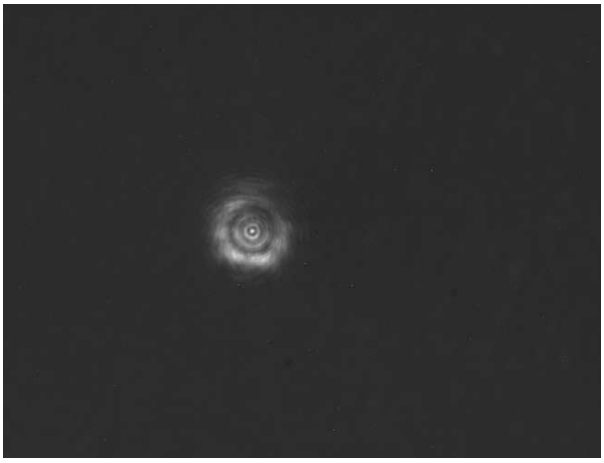

Figure 5.8: Conventional microscope image of a subwavelength aperture, showing diffraction induced Airy-disks.

The deposition chamber was equipped with an aperture collimated, current heated evaporation source for aluminum and chromium and a stepper motor for rotating the fiber tips. The mechanical rotation of the tips allowed for an even, circular deposition of the metal coating. The thickness as well as the deposition rate was monitored by a micro crystal balance. Generally vacuum pressures of 10^{-6} torr by use of a cold trapped diffusion pump backed up by a roughing pump were reached.

5.2.5 Waveguide materials for the infrared wavelength range

The previous sections described the standard methods used to make optical fiber based apertures for near-field optical microscopy in the visible wavelength range. Extending the transmission range into the infrared leads to a variety of new problems that have to be solved.

Most importantly the fiber material has to have waveguiding capabilities for the chosen wavelength. Commercially available fibers that are transmittant in the required wavelength range around 3 μm are either made of sapphire, doped fluoride or chalcogenide. These materials are either difficult to melt (sapphire) or are made of toxic chemical compounds that can become volatile when heated (chalcogenide).

5.2.5.1 Sapphire

While sapphire has superior mechanical and optical properties as a fiber tip, it is actually very difficult to manufacture a tapered cone from a bare sapphire fiber. Sapphire has very poor heat conductivity, which makes it hard to achieve a uniformly melted volume in the center of the CO_2-laser beam. This leads to a non-cylindrical symmetry of the fiber tip after pulling. Etching of sapphire on the other hand is almost impossible due to its inertness to any solvents. Only hydrogen fluoride is capable of etching sapphire but too difficult to use for a repeatable method of producing fiber tips.

5.2.5.2 Chalcogenide

Chalcogenide fibers are made out of a mixture of arsenic (As), selenium (Se) and telluride (Te). They are transparent over a great range of the infrared spectrum but mechanically very fragile. Another disadvantage is contributed by silver halogenides that are also a compound found in chalcogenide fibers and will darken the material when exposed to visible light, which will make the fiber appear opaque. Hence it is not possible to use the

same fiber as a waveguide for infrared as well as visible light. Making tapered fiber tips by the pulling method described above is shown to work [75], but the high concentration of toxic elements requires precautions, that were not available in the current set-up. As shown by Unger et al. [73], etching chalcogenide fiber results in fiber tips with short tapers and big taper angles. While this is desirable for infrared near-field probes and indeed can produce tips of superb quality (figure 5.9), the reproducibility with the etching method was very poor and therefore had to be abandoned.

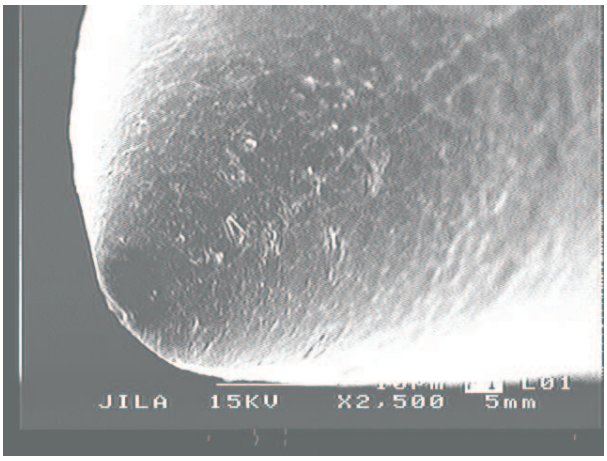

Figure 5.9: SEM image of an etched tip. This tip was coated with a 30 nm layer of aluminum and clearly shows a round aperture of about 1 μm diameter.

5.2.5.3 Zirconium aluminum fluoride

For the results achieved in this work, pulling fluoride doped fibers turned out to be the most reliable way to reproducible fiber tips. Etching of this fiber was also examined but discarded due to unsatisfactorily big surface roughness. The fiber was purchased from Infrared Fiber Systems, Inc. with a core diameter of 100 μm and a vinyl cladding. The chemical composition of the fiber material is given by 53% ZrF_4, 20% BaF_2, 4% LaF_3, 3% AlF_3 and 20% NaF. The cladding was easily removed by sonicating the fiber in di-chloromethane for a few minutes. At first, pulling the fiber with different parameter settings on the micropipette puller resulted in undesirably long tapers, which left the fiber tip mechanically unstable and more importantly limited the light throughput to 10^{-6} and less.

The light throughput of a fiber based near-field optical aperture is mainly determined by three factors: The diameter of the aperture, the cone angle of the taper and the wavelength. Once the diameter of a waveguide is smaller than approximately the wavelength most of the energy will partly be reflected back or dissipated into an evanescent field.

Since it is always unavoidable that the light has to be guided through some length of the taper with a diameter smaller than the wavelength, one should keep this distance as short as possible to minimize the losses. Hence for high throughput it is desirable to have a big cone angle such that the light has to be guided only through a short region, where the diameter of the taper is smaller than the wavelength.

Achieving big angled tapers by pulling, which at the same time have a pointy, sharp end with a diameter no bigger than 100 nm, is intrinsically difficult. In order to form short tapers the pulling velocity on the fiber melt has to be very small. This in turn leads to blunt tips and does not produce a well-defined sharp tip end. With faster pulling speeds on the other hand one reaches the necessary finite tip diameter of at least 100 nm at the cost of a long small-angled taper.

5.2.6 Two-taper pulling of near-field optical probes

Combining the advantage of power delivery of a blunt tip with small aperture formation of sharp tips is key to high resolution/high throughput near-field optical probes.

At first the tip is formed by using a slow pulling velocity, leading to a blunt tip. Just before the melted fiber separates the speed is increased and a sharp tip rises from the top of the rounded taper. The overall length of both tapers is only about 200 to 400 μm, which is much smaller than a single taper with a comparable tip end curvature.

This two-step pulling procedure is made possible by the computer controlled micropipette puller. The electronics of the puller controls the parameters pulling force, velocity and time duration, where force and velocity can be varied within a time resolution of better than 1 ms.

Figure 5.10 shows electron micrographs of a fiber tip, that was pulled using the two-step method and coated with aluminum afterwards. In figure a) one can clearly see the first taper, which by itself would lead to a blunt tip. Zooming in on the tip reveals the second taper in b) and further magnification even shows the aperture that has formed at the end of the coated tip. Typical aperture diameters of 200 to 300 nm were obtained. The throughput of such a near-field optical aperture was about 10^{-4} to 10^{-5} at 3 μm wavelength and therefore two to three orders of magnitude better than single tapered tips.

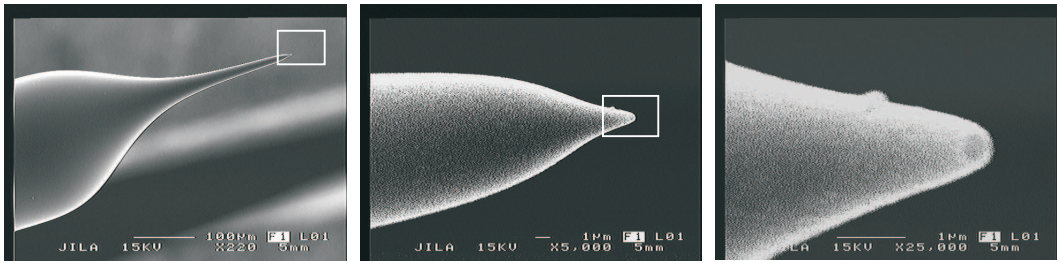

Figure 5.10: Two-step fiber pulling first produces a blunt tip, which receives a second taper with a much narrower taper shortly before the fiber breaks apart.

5.3 Light sources

5.3.1 Color center laser (FCL)

For the majority of the experiments a color center laser (FCL) by Burleigh Instruments was used. The laser offers a wide tuning range of 2.7 to 3.3 μm at output powers of up to 1 mW. As active medium a rubidium chloride crystal doped with fluorescent defect sites was placed in a folded Littrow-type cavity. By changing the angle of the grating the wavelength could be tuned throughout the amplification range of the rubidium crystal. The crystal was pumped by a Kr^+-laser with 1 Watt output power at 647 nm. In order to increase the possible output power of the FCL, the pump beam was chopped typically at 300 Hz. During the short dark intervals, the crystal could dissipate much of the heat produced by the absorbed pump intensity and therefore had a higher lasing efficiency. With this method average output powers on the order of 1 mW were achieved.

The main disadvantage of the FCL is given by the fact that it has to be used in multi-mode operation in order to reach the maximum output power given above. The multi-mode operation intrinsically increases the output noise of the laser. Another noise contribution comes from the pump laser itself due directional fluctuation of the output. The color center laser is very sensitive to any steering changes into the infrared cavity, which amplifies small fluctuation to relatively big output noise. In summary the infrared output of the FCL revealed intensity fluctuations of typically 1 %.

5.3.2 Diode laser (PbS)

In the past, only very few solutions to produce coherent light in the mid-infrared regime were available. The above color center laser was the most popular tool for spectroscopists due to its robustness and fairly high output power. Another way of reaching into the "fingerprint"-region of molecules was introduced by difference frequency generation. For this method, two single mode lasers, operating in the visible or near-infrared wavelength range, are overlapped in a nonlinear crystal, that has to be temperature- and angle-controlled. While it is possible to produce mid-infrared single mode output, the output powers are not high enough for the near-field microscopic application. Optical parametric oscillators (OPO) can span up to $\lambda = 3.75$ μm by use of a periodically poled lithium niobate crystal. The output power on the other hand is reported as big as a few Watt. [76]. Still a lot of research is done on improving quantum cascade lasers for the infrared wavelength range. While lasing has been achieved from 3.5 to 24 μm, today's output powers can also reach up to 0.2 W_{cw} [77]. Only recently did diode lasers become available for the infrared wavelength range spanning up to 30 μm [78, 79]. The lead sulfide based lasers have superior intensity and directional stability and can reach output powers of up to 1 mW. Since thermally induced recombination makes it difficult to achieve a population inversion in the small bandgap, the lasers have to be cooled in most cases to liquid nitrogen temperature. By use of an additional Peltier element, the temperature of the diode can be varied and hence the output wavelength be tuned. Wavelength tunability usually covers a range on the order of 1 % of the center wavelength, making the diode laser far less tunable than the color center laser. This makes it necessary to have more than one laser readily mounted in the beam path to cover a bigger spectroscopic range. A disadvantage that has to be accounted for is the largely diverging, asymmetrical beam profile of the diode laser. It is caused by diffraction at the laser diode exit slit. A parabolic mirror and two lenses forming a telescope are at least necessary to produce a parallel beam with a gaussian intensity distribution.

5.3.3 Incoherent light sources

Another way of producing infrared light is given by bulb-like incoherent light sources. Best known is the so called Nernst globar, which is considered a black body radiator. Usually it is manufactured from silicon carbide and its radiation temperature can be tuned by electrical heating. Typical applications are fourier transform infrared spectrometers, which need a broadband infrared light source. For the experimental set-up as described in this work, the globar is only of limited use. For spectroscopic measurements, only a small

wavelength range of its output can be used, which decreases the already small output power by a lot. The radiation does not have a pronounced direction either, so rather complicated optics have to be employed to couple the spherical infrared output into the optical waveguide of the near-field optical microscope. For the above reasons, the globar was not suitable for the following experiments and therefore discarded as an infrared light source.

5.4 Detectors

The further the detectivity needs to be extended into the infrared wavelength range the more difficult it is to find suitable semiconductors. The biggest challenge is to keep the noise low, which is intrinsic to detectors with smaller bandgaps. Since small bandgaps are needed to detect low energy photons it is more and more likely that thermal energy is high enough to bridge the bandgap and cause electron-hole recombination without the presence of a photon. This leads to a permanent background current and also causes intrinsic noises as the Shot-Noise to be increased. At the same time it is important that the detectors have a high enough bandwidth to follow the scanning motion of the microscope.

The optimal detectors for the wavelength range around 3 μm are photovoltaic indium antimonide (InSb) based detectors. Their detectivity is as good as D = $1{\cdot}10^{11}$cm $\sqrt{\text{Hz}}$/W (at 1 kHz) with a peak responsivity of 3 A/W [80]. To decrease noise, the detectors are mounted in a dewar and cooled with liquid nitrogen. A small tube in front of the sensitive area, which is also cooled down to liquid nitrogen temperature, provides a cold field of view so that only photons from the forward direction can enter the detector area. It also encapsulates the detector almost completely in a cooled volume so that temperature induced recombination is decreased to a minimum.

The detector bandwidth is controlled by the size of the sensitive area as well as by the electrical pre-amplifier. The smaller the active area of the detector is, the faster the response will be. On a smaller detector area the recombined electron-hole pairs can reach the electrodes faster and the driving electric field does not need to be as high (less noise). Since InSb detectors are current sources, a pre-amplifier has to convert the current to a voltage. This is done in the simplest case with a single resistor or in a more elaborate way with an operational non-FET amplifier. The size of the resistor determines the amplification but is also a load for the detector. So there is a trade-off between amplification and bandwidth of the detector.

6 Fourier Transform Infrared Spectroscopy (FTIR)

A Fourier transform infrared spectrometer (FTIR) is a great tool to gain precise information on the type of molecules that are present in a sample. It is used to determine the vibrational and rotational excitations of molecules. In the gas phase these excitations result in a complex frequency pattern composed of very narrow linewidths. Molecules in solid environments on the other hand show broadening of the absorption lines to the extend that groups of usually narrow lines smear out to one broad peak. The reason for this broadening effect is due to the fact, that the molecules are embedded in a solid matrix, which restricts the free vibration of the molecular branches. Still, these broad peaks can usually be assigned to specific groups of the involved molecules.

On first sight, FTIR should be the tool of choice to track diffusion in polymer thin films, since different infrared spectra allow to differentiate between the original and the deprotected polymer [81]. Unfortunately the infrared wavelength range puts a limit to the lateral resolution, which makes it impossible to observe feature broadening due to diffusion on the scale that is happening under realistic conditions.

For specially designed samples the above limitation can be overcome. By using a periodic structure, broadening that occurs at a single feature can still be measured due to averaging over many of them. In case of the samples prepared by interferometric lithography a periodical structure is inherently given, so they are therefore well suitable for FTIR experiments. Since the average UV irradiation was also varied throughout those samples, lateral resolution is required to resolve the influence of the illumination intensity. This requirement is not very difficult to fulfill, since the intensity changes occur on the scale of millimeters.

A Michelson interferometer is the basis for fourier transform infrared spectroscopy. The spectrometer consists of a "white" light source made of a Nernst globar (see also section 5.3.3), a beam splitter sending the light to a fixed mirror, a moving mirror, the sample to be measured, and a detector (figure 6.1).

A spectrum is acquired by recording the intensity of the radiation at the detector as a

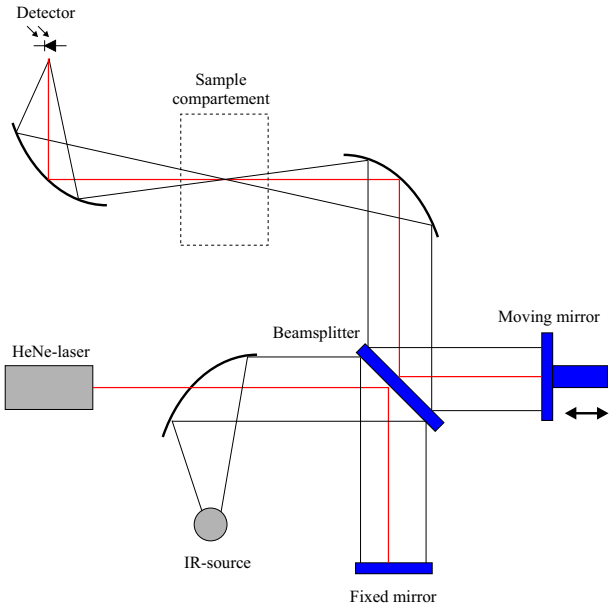

Figure 6.1: A principle set-up of a fourier transform infrared spectrometer.

function of the position of the moving mirror. As a result a spectrogram is obtained, which is recorded in the time domain. The signal at the detector is given by the interference of the backreflected light from the fixed ($\overrightarrow{E_1}$) and the moving mirror ($\overrightarrow{E_2}$) respectively:

$$I_{det} = |\overrightarrow{E}|^2 \tag{6.1}$$

$$= |\overrightarrow{E_1}|^2 + |\overrightarrow{E_2}|^2 + 2\overrightarrow{E_1} \cdot \overrightarrow{E_2} \cos\vartheta \tag{6.2}$$

With the light propagating only in one direction, the angular change ϑ can be expressed as $k_x \cdot x$. Here, k_x is the x-component of the wave propagation vector and x the position of the moving mirror. Also assuming that the backreflected light from both arms is equal in intensity, the above expression simplifies to:

$$I_{det}(x) = 2I(1 + \cos(k_x x)) \tag{6.3}$$

For light, which is not monochromatic - as it is the case for the infrared light source - the phase relation is different for each wavelength in the interferometer. Hence the output at the detector is composed of the intensity spectrum G(k_x) and the response of the

interferometer for each wavelength:

$$I_{det}(x) = \int_0^\infty (1+\cos(k_x x))\, G(k_x) dk_x \tag{6.4}$$

$$= \int_0^\infty G(k_x) dk_x + \int_0^\infty G(k_x) \frac{e^{ik_x x} + e^{-ik_x x}}{2} dk_x \tag{6.5}$$

$$= \frac{1}{2} I(0) + \frac{1}{2} \int_{-\infty}^\infty G(k_x) e^{ik_x x} dk_x \tag{6.6}$$

By rewriting the above equation, the term, which just contains the measured intensities as a function of the position and the term containing G(k_x) can be separated:

$$\frac{2I(x) - I(0)}{\sqrt{2\pi}} = \frac{1}{\sqrt{2\pi}} \int_{-\infty}^\infty G(k_x) e^{ik_x x} dk_x \tag{6.7}$$

The right term is only a function of frequency (wave numbers) now and can easily be accessed by a fourier transformation.

Usually two spectra are recorded: one with the sample placed in the path of the light and another one without the sample. The two spectra are subtracted point by point and the result is fourier transformed to obtain the frequency-dependent transmission of the sample. The reflectivity of the sample can be measured similarly. A coherent light source (He-Ne laser) is usually included in the beam path to enable an in-situ calibration of the moving mirror position, while taking the spectrum.

A commercial fourier transform infrared spectrometer (Nicolet 670) was used to obtain infrared transmission spectra at different lateral positions on the samples. The sample compartement was nitrogen purged to avoid influences from ambient air, especially water contributions. The spectral resolution was set to 8 cm^{-1}. For the precise positioning of the sample in the beam path some modifications were introduced to the sample holder. A mechanical mount allowed accurate positioning of the sample in vertical direction of the infrared beam, while a circular aperture in proximity to the sample restricted the spectra to be taken from a 0.8 mm^2 area. By manipulating the mount the sample could be moved with an accuracy better than 0.1 mm relative to the pinhole and therefore relative to the infrared probe beam to any point in the plane of the polymer film.

7 Apertureless near-field optical microscopy

While the fiber-tip based near-field optical microscope shows lateral optical resolution better than $\lambda/10$ for $\lambda = 3$ μm already, experiments were conducted to increase the resolution even further. Experimental work by Wickramasinghe et. al. fairly recently demonstrated the possibility of scattering light at a small apex of subwavelength diameter using an AFM tip made from silicon [59]. Oil droplets were examined to exhibit the improvement in optical resolution and first attempts were made to explain the image contrast of these scans.

With samples, that show dynamics occurring in a range of a few ten nanometers, the prospects of applying the technique of apertureless NSOM to diffusion in polymer thin films are promising. Therefore a modified instrument similar to Wickramasinghes set-up was build and images were obtained to characterize the capabilities of the instrument.

The mechanical base of the microscope was the same as described for the IR-NSOM (section 5.1). The head of the microscope and the optical beam path on the other hand had to be altered. The kinematic mount was modified to hold a typical atomic force microscope head. The head consists of an AFM cantilever, which oscillates in the vertical plane due to a small driving piezo similar to the one used in IR-NSOM. The focussed light of a diode laser ($\lambda = 630$ nm) is reflected off the back of the cantilever and detected with a quadrant photodiode. By aligning the photodiode relative to the beam, such that the beam is centered over two quadrants, the oscillation of the cantilever can be monitored. The damping of the oscillation amplitude upon approach is used for a feedback-based distance control (figure 7.1).

The light source for all apertureless NSOM experiments in this work was an intensity stabilized He-Ne laser lasing at $\lambda = 633$ nm. The output power was measured to 1 mW with the polarization being linear at a polarization ratio better than 500 to 1. The light was broadened in diameter and filtered spatially to obtain a pure TEM_{00} mode, which is necessary to reach the theoretical focus limit of the objective.

The illumination/collection beam path is the same as used for classical confocal reflection

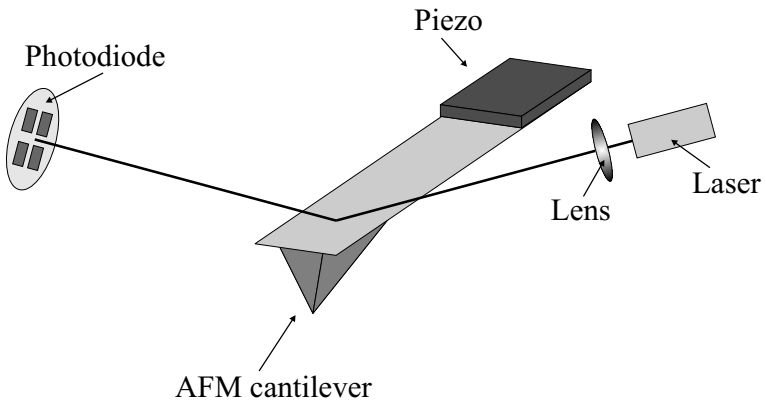

Figure 7.1: AFM detection scheme: Light from a diode laser is reflected of the back of an AFM cantilever and detected by a quadrant photodiode. The oscillation of the cantilever translates into a voltage signal at the photodiode.

microscopy. Incoming light is focussed by an objective (NA: 0.55, working distance: 11 mm) on the sample surface with the backreflected signal being collected by the same objective. A beamsplitter below the objective allows the incoming light to be coupled into the collection beam path colinearly. The backreflected signal is focussed on a pinhole, which is placed in front of the detector. With the pinhole diameter matching the focal diameter of this second objective, a confocal collection path is build, which will only guide light coming from a small associated volume on the sample to the detector. Hence, contributions from other sources outside this volume are greatly reduced.

Backreflections from surfaces in the beam path, especially of the back of the sample on the other hand are still present on the detector, so the total signal consists of a strong reflected field E_r and a weak scattered field E_s from the tip. Therefore E_s has almost no influence on the total amplitude of the signal interfering on the detector. More background light from surface contributions will also lead to an enhanced Shot-noise level of the detector making it less sensitive to small amplitude changes due to tip-sample interactions. An alternative way of detecting small influences on a hugh background was first introduced by Batchelder and Taubenblatt for small particle detection in a conventional microscope [82]. Similar ideas were published by Somekh et. al. [83]. Here a second beam is projected right next to the region of interest - the probe in this case - and is recombined with his neighbor on the detector. Now the first beam contains the signals E_r and E_s, while the second beam is only comprised of E_r. More importantly, E_s has introduced a small phase shift to the first beam, due to the localized interaction with the sample and also due to the Gouy-shift. The Gouy-shift causes a Gaussian beam in

the center of a focus to change its phase by $\pi/2$. Comparing the phase of both beams in a sensitive phase interferometer will allow to see very small fluctuations of E_s.

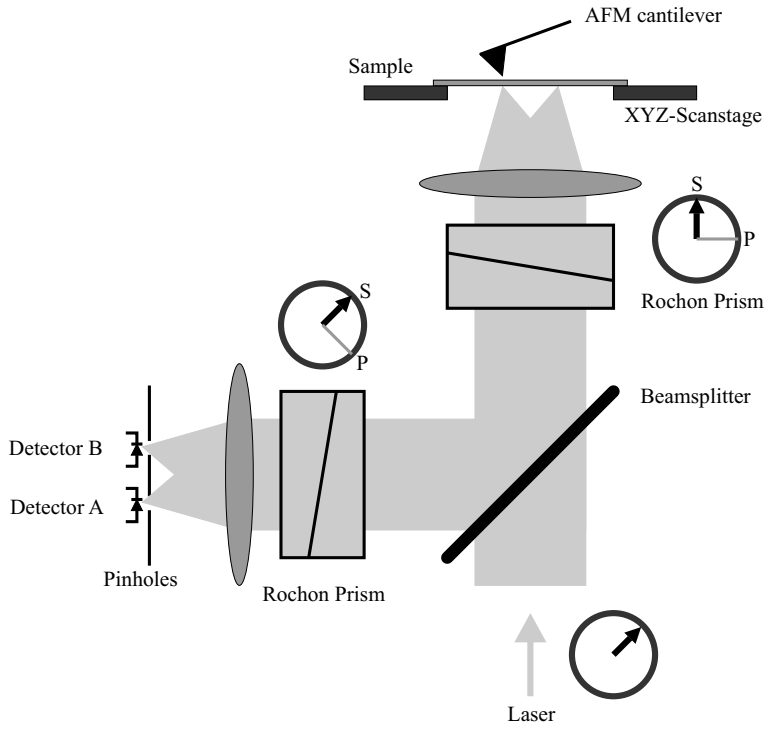

Figure 7.2: The set-up as used for the apertureless NSOM measurements

The implementation of the above concept is seen in figure 7.2. Two foci are produced on the sample surface by introducing a rochon prism in the beam path right before the light is focussed by the objective. A rochon prism is made of two birefringent crystals, which are glued together. Depending on the polarization state of the incoming light, the light passes through the crystal straight or is projected at a different angle than normal to the crystal surface. Hence two beams of equal intensity are produced if the polarization state of the incoming light is linearly polarized at a 45^o angle. The distance between the two focal spots is related to the angular divergence of the rochon prism, which can be influenced by the cutting angle of the two crystals. After being backreflected of the surface both beams are roughly recombined but can still be distinguished due to their individual polarization states. A second rochon prism is placed in front of two detectors at a 45^o angle with respect to both polarization states, mixing both beams so they can interfere on each detector. The output at the two detectors is described as follows:

$$I \propto A^2 + B^2 + 2AB\cos\left(\phi(\gamma_1 - \gamma_2)\right), \tag{7.1}$$

with A and B being the signals on the individual detectors, ϕ resembles the sum of all

constant phase shifts and $\gamma_{1,2}$ is the individual phase shift at each focus. As one can see, the phase changes between the spots due to perturbation by the AFM tip result in an intensity change of the the mixed term AB [84, 82, 85] and hence become detectable.

For signal recovery a lock-in amplifier (Stanford Research Instruments, SRS830) was employed. The AFM tip was dithered at its resonance for topographic tracking but in addition at a lower frequency (1 kHz) of very small amplitude to introduce a modulation of the optical signal. The high resonant frequency of the AFM cantilever could not be used, because the lock-in amplifier could only operate at frequencies lower than the standard resonances of AFM tips. For studies of the influence of topographic artifacts, the amplifier could either detect the optical signal at the modulation frequency or at multiples of it.

Observation of enhancement of the expected scattering signal has been reported by other groups [86] and is thought to be influenced by the shape and material of the probe and sample.

Comparison of plain AFM tips (length-to-base ratio: 1) with ion-milled, high aspect-ratio ones (length-to-base ratio: 10) did not yield any measurable improvement of the contrast. Coating of standard silicon AFM tips with a thin layer of gold (10-20 nm) on the other hand did help the signal enhancement by a factor of 2 to 5 depending on the quality of the coating. Figure 7.3 shows SEM images of a gold-coated tip. The magnification on the right reveals the disadvantage of a gold coating, since the tip usually is broadened and hence cannot track the topography as well as without the additional gold layer.

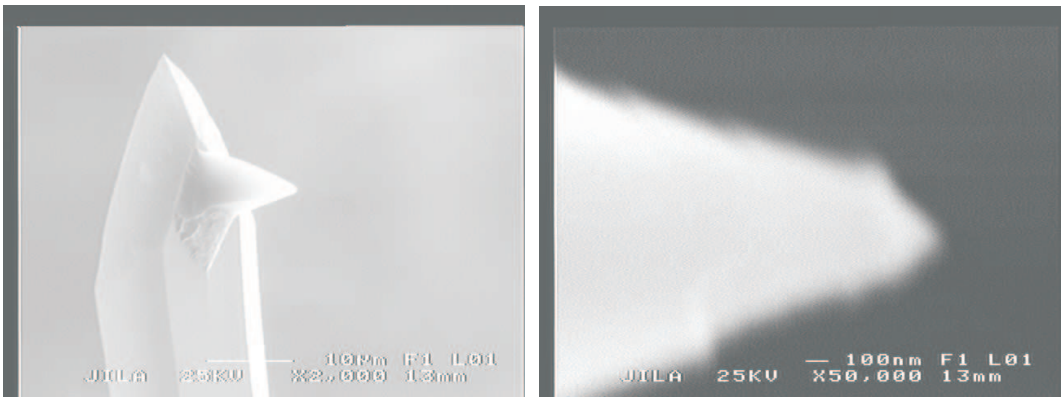

Figure 7.3: Scanning electron micrographs from gold coated AFM tips. The magnification on the right shows that the radius of the tip is 50 nm or better, which is limited by the resolution of the SEM.

8 Photoresist polymer structures

8.1 Infrared near-field optical imaging

8.1.1 General remarks

With decreasing feature sizes in modern semiconductor industry, the requirements for better photolithographic processes are vastly growing. This trend has lead to the use of chemically amplified photoresists, which were introduced earlier in this work. Structures as small as 100 nanometer make it necessary to not only understand the general image formation upon UV exposure of the resist, but to study the microscopic properties, which take an important role in the formation of the written features.

Infrared near-field optical microscopy (IR-NSOM) is a promising tool to examine microscopic processes in latent image formation [87, 88, 6]. The development of the photopolymer resists can be traced by monitoring infrared absorption bands, that are specific for the amount of deprotection in the polymer film. So far, tracing of the nonlinear chemistry in photopolymer samples by infrared absorption measurements could only be performed on bulk samples on a macroscopic scale due to low lateral resolution of available infrared techniques. With the introduction of a near-field optical microscope operating in the infrared wavelength range, the resolution is not limited by diffraction optics anymore and can therefore offer new insights in local effects in the latent image [5, 89, 90, 91].

Due to the presence of reactant concentration gradients caused by light intensity variations at edges, the local chemistry on a submicron feature can be quite different from the bulk. Important phenomena that limit the resolution are the diffusion of photogenerated acid during the postexposure baking step and random fluctuations in the width of a resist feature, termed line-edge roughness (LER) [16]. The line-edge roughness develops at the dissolution step, but it is actually related to the projected (aerial) UV image contrast. The patterned result after the dissolution step, being the last in the process flow, is readily characterized by scanning electron microscopy (SEM) or, for low aspect ratios, by atomic force microscopy (AFM). The post-exposure baking step can also be partly characterized by AFM, revealing the topographic changes that generally occur at this stage and even after the exposure step for both negative and positive-tone resists. However, the important chemical changes occurring in these steps may not always simply

correlate with the topographic changes. Chemically-specific techniques like on-wafer fluorescence microscopy were developed and used to monitor photoacid production. However, the fluorescent molecular probes incorporated into the polymer film may affect the acid activity [92, 93]. IR-NSOM has certain advantages over the above mentioned methods: it is non-intrusive, it achieves much higher spatial resolutions than conventional optical microscopes, and it generates chemical and topographic images at the same time, offering the ability to follow the chemical modifications directly [94, 6].

In the following all IR-NSOM experiments on photolithographic polymers were conducted on the same type of sample. The photoresist chosen was poly(tert-butylmethacrylate) (PTBMA), which is part of the family of acrylate photoresists, that show promise for deep-UV lithography. The resist samples were doped with 5 wt % of the photoacid generator triphenylsulfonium hexafluoroantimonate. Film thicknesses obtained by spin-coating were either 1000 nm or 250 nm. The patterning was done by a chromium contact mask and the UV illumination wavelength was 250 nm, with a maximum dose of 21 mJ/cm^2.

8.1.2 Contrast mechanisms in polymer films

In order to understand more quantitatively the contrast formation in near-field optical microscopy a single line feature of 1 μm width was examined. The film thickness was also 1 μm for the unexposed regions. Figure 8.1 shows the optical images for "on-resonance" (left) and "off-resonance" (right). The wavelengths used were 2.92 μm and 2.75 μm respectively. Both images were taken in constant height mode in order to reduce the possible occurrence of topographic artifacts in the optical image. The dark regions correspond in this case to less absorption.

Two facts are worth noting concerning the image in figure 8.1: First, the UV-exposed line dimension is quantitatively larger when the resonant wavelength is used (2.92 μm). Second, an image of the line is present, even when the absorption is near zero for both the irradiated and non-irradiated zones.

The explanation of these features requires consideration of the contrast mechanisms in relation with the resolution at resonant wavelengths, the achievable chemical contrast and the overall contrast. Lets concentrate first on the contrast at non-resonant wavelengths. The experimental contrast of this image is 10 %, while the contrast at $\lambda = 2.92$ μm is 15 %. Therefore the overall contrast has to have a major non-resonant component.

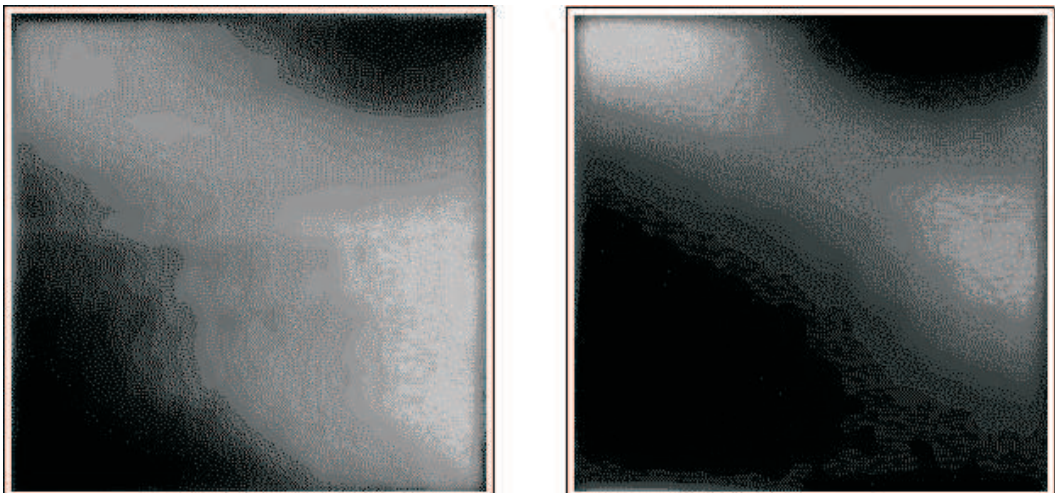

Figure 8.1: IR-NSOM optical images of a 1 μm thick film. The scan range was 2 μm × 2 μm. The left image is taken on the absorption band at 2.92 μm, while the IR laser was completely tuned away from any possible absorption to 2.75 μm in the right image.

With no absorption at 2.75 μm the contrast must be refractive in origin. There are two explanations for this: First the real part of the index of refraction changes when moving from an UV exposed region to a non-exposed region or second the thickness of the exposed film is different from that of the non-exposed film and multiple reflections occur. Both situations lead to different reflection coefficients for the exposed and unexposed films and therefore different external transmittances. The reported refractive index for PTBMA at the sodium D line (589 nm) is n = 1.464, and the poly(acrylic acid), a close analog of poly(methylmethacrylate) (the deprotected form of PTBMA) has n = 1.5. At this wavelength and for a collimated beam, the far-field variation of transmittance, due to the index of refraction modification subsequent to UV exposure, should be around 0.5 %.

The film thickness variation causes an external transmission variation only if multiple reflections occur. In this case, and considering the above variation in the real part of the index of refraction and a collimated beam, one expects only a 4 % contrast in the visible region. It should therefore be possible to obtain NSOM images of patterned photoresist films at visible wavelengths, and this experiment has also been realized in our laboratory. However, the observed contrast is as high as 18% (at 675 nm, krypton ion laser) even though there is no observable absorption. The contrast using visible light (675 nm, 18 %) is higher than the maximum contrast with IR light (about 2900 nm, 10-15 %), where there is absorption as obvious from the IR spectra. Therefore, calculations of the contrast based on collimated beams and far-field refractive effects give results significantly smaller

than the experimental ones. It follows that the source of contrast must be related to the actual geometrical shape of the beam, collimated in the near-field and divergent in the far-field.

The fact that the beam is collimated at the exit of the tip for distances comparable to the aperture diameter, while it has a divergence of about 80^0 in the far-field, indicates that some of the light rays are totally reflected by the sapphire substrate at the air interface as depicted in figure 8.2. The refraction angles are different at the polymer/sapphire interface for exposed and unexposed areas, therefore a different amount of light will be totally reflected at the sapphire/air surface as the tip is located above exposed or unexposed regions of the polymer. The difference in the maximum angle of transmitted light in these two cases gives rise to a contrast of refractive origin, called here the cone angle effect. Using the difference in the real part of the indices of refraction for the exposed and unexposed polymers, in the visible, this contrast can be estimated at approximately 11 %, the same order of magnitude as the experimental one. These estimates show that, in our case, this is the main mechanism for the overall contrast, when no absorption is present. The contrast magnitude is proportional in this case to the numerical aperture of the collection optics.

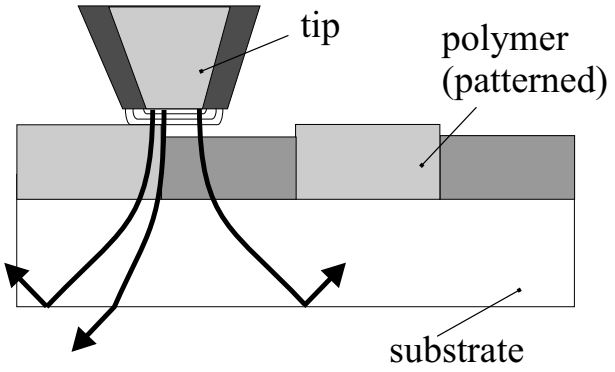

Figure 8.2: Spreading of the angular distribution of the probe light in absorptive and refractive contrast mechanisms. In the case of a thick film, the envelope of light includes, at the same time, exposed and unexposed zones of the polymer.

To investigate the contrast mechanisms further, we performed confocal microscopy imaging, with 633 nm laser light, of similarly prepared samples, but with 16 μm features. The same contrast as found in the NSOM images at 675 nm was observed. From this comparison two conclusions can be inferred. First, a possible enhancement of the contrast of the visible NSOM images by a topographic artifact can be ruled out since the same contrast is obtained with the confocal microscope, which is a far-field technique. Second,

one obtains more than 15 % contrast only when using focused beams with a different divergence in the near and far fields. This suggests that the refractive cone angle effect accounts for the most of the contrast.

Let us consider now the chemical effect observable as a difference of about 5 % in the contrast of the images of figure 8.1. In the IR, in addition to the mechanism related to the real part of the index of refraction, there is also contrast given by the difference in the absorption coefficient between exposed and unexposed areas. Again, the IR light emitted by the NSOM tip has a certain angular distribution varying with the distance from the tip. It follows that thicker films, together with the large cone angle of IR light emitted from the NSOM tip, will spatially broaden the absorbing region.

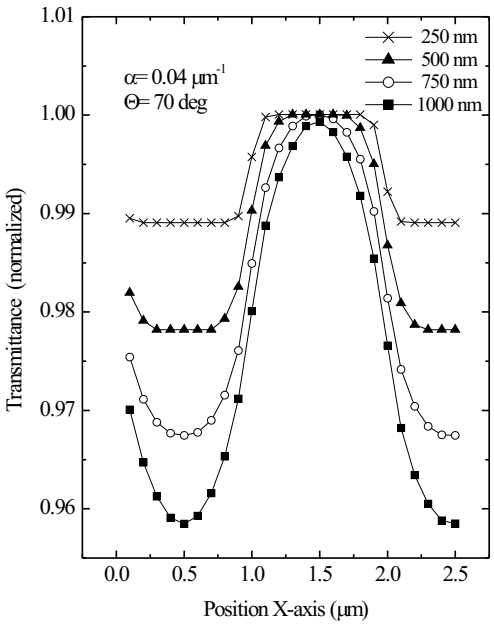

Figure 8.3: Calculated IR transmittance of the patterned film (1 μm line spacing) for different film thicknesses. This calculation considers the absorption mechanism only.

The result of far-field integration of the transmitted IR light over the angular range of emission is presented in figure 8.3. The observable modulation is shown only for the effect of the absorption coefficient (at the resonant wavelength) as the tip scans the surface. An ideal tip of aperture much less than the surface features has been considered. One can infer from these simple calculations that the resolution is limited in the case of

thick polymer films by the far-field effect of angular averaging during collection. One can avoid this by decreasing the numerical aperture of the collection optics at the expense of sensitivity. Also, the calculated contrast for 1 μm-thick films of about 4 %, agrees well with the contrast difference between the resonant and non-resonant wavelength images (about 5 %). The difference in film thickness does not contribute significantly at IR wavelengths since it is very small compared to the wavelength. As a consequence all following measurements were done with a small numerical aperture lens system. Considering the film thicknesses and the above estimates, numerical apertures of less than 0.25 do not contribute substantially to the expected absorption contrast in the following experiments.

8.1.3 Absorption contrast for on- and off-resonance imaging

With the influence of different contrast mechanisms known, pure absorption measurements can be obtained by IR-NSOM. This is very useful, since before more than one parameter of the sample properties influenced the optical imaging. At first fairly large structures with a line/space pattern of 8 μm / 8 μm were imaged in constant height mode. In this case, the shear-force feedback was disabled. The average tip height over the surface was roughly 250 nm. Due to the feedback control switched off, large area scans were possible at reasonable speed. Images acquired in this mode are also expected to exhibit fewer topographic artifacts. The IR-NSOM images given in figure 8.4 were taken at two different wavelengths, 2.80 μm (a) and 2.94 μm (b). One can easily notice the spectroscopically enhanced contrast in image (b) as compared to image (a). The image taken at 2.80 μm wavelength still shows some contrast, mainly at the borders between the irradiated and non-irradiated areas. Since we expect about 400 nm shrinkage of the 1 μm thick film upon post-exposure bake, the deep edge formation could explain the presence of contrast via refractive mechanisms. One can also notice that the vertical edges of the features in figure 8.4 are sharper than the horizontal edges. This is more apparent in image (a). Since the IR radiation is linearly polarized, the enhancement of the edge contrast is possibly due to a polarization effect.

To obtain maximum spatial resolution, the near-field images need to be acquired in the constant gap mode (about 5-10 nm gap, using shear-force feedback). Constant shear-force (topographic) and IR images at 2.85 μm ("off-resonance" (a)) and at 2.94 μm ("on-resonance" (b)), for a 2 μm / 2 μm line/space pattern on a 1000 nm thick film are presented in figure 8.5. The contrast is about 2 %, which matches well with the calculated contrast for pure absorption from the bulk absorption coefficient ($\alpha = 0.04\ \mu\text{m}^{-1}$).

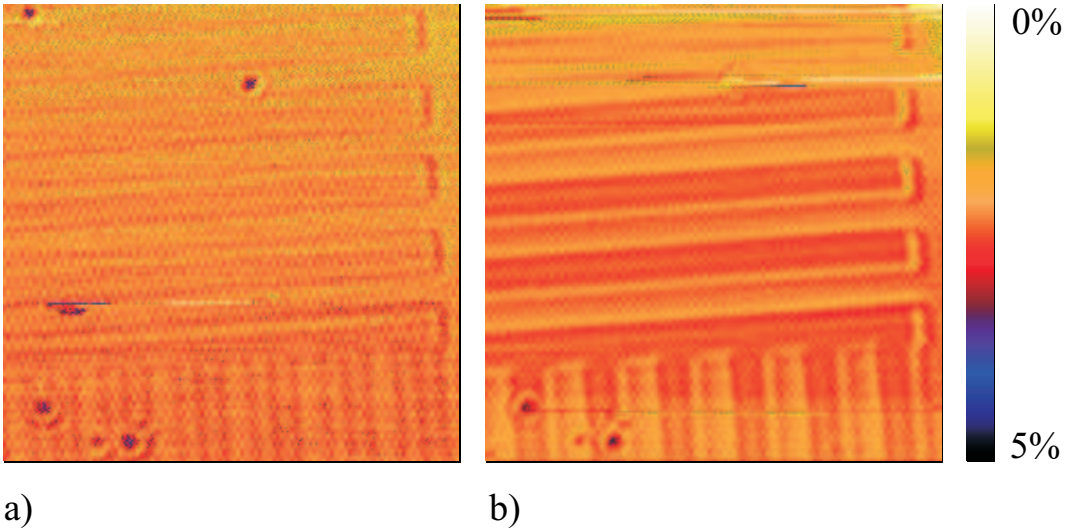

Figure 8.4: IR-NSOM optical images in constant height mode. The features shown have a line/space width of 8 μm × 8 μm. Image (a) was taken at λ = 2.80 μm and (b) at λ = 2.94 μm.

An example for the high lateral resolution well beyond the diffraction limit can be seen in figure 8.6. The line/space pattern was 1 μm / 1 μm on a 250 nm thick polymer film. For the optical image the wavelength was tuned to maximum contrast at λ = 2.97 μm. Average horizontal cross-sections of the IR and topographic images are also included. This line/space pattern is close to the limits of this particular NSOM tip in terms of spatial resolution. Thus both the contrast and clarity of the image are degraded compared to images of wider spaced lines. The deeper zones in the topographic image correspond to more strongly absorbing zones in the IR image, as expected. The UV dose was 21 mJ/cm^2. The maximum absorption modulation (0.5 %) is less than the expected value from the experimental determinations in the far-field, with the absorption modulation being defined as the difference between the peak and the valley signals divided by the average signal. Below 2.8 μm wavelength there was no contrast at all in the optical scans.

The apparent spatial resolution of the IR image from figure 8.6 is at least 500 nm. The non-averaged signal-to-noise (S/N) ratio is roughly 2. In addition to the pattern smearing due to interference, another cause for the small S/N value is the angular pointing stability noise of the krypton ion laser beam that pumps the color-center laser, thus affecting the pointing of the color-center beam. Since this is a very low frequency noise, it can be seen in the optical image of figure 8.6 as horizontal streaks (slow scanning axis is oriented vertically). However, the averaged line scan (over 100 lines) has a better S/N ratio of 20.

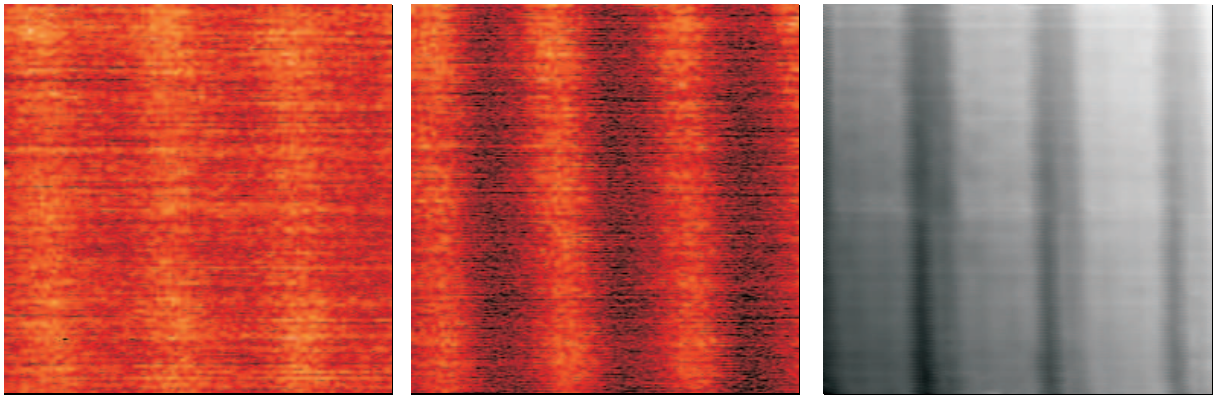

Figure 8.5: Specific IR absorption for exposed and unexposed areas result in contrast variations of the optical images (12.5 μm × 12.5 μm) taken at two different wavelengths: (a) λ = 2.85 μm and (b) λ = 2.94 μm. (c) shows the corresponding topographical image, with the darker regions being the exposed features.

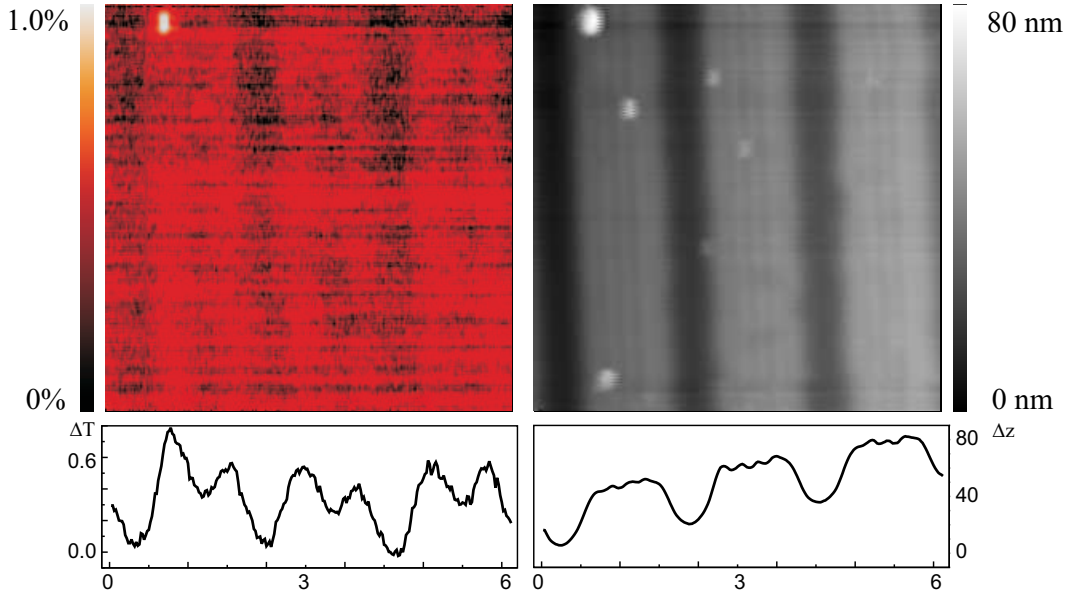

Figure 8.6: IR-NSOM optical and topographic images of 1 μm / 1 μm line/space pattern (250 nm thick film). Scan range was 6.25 μm × 6.25 μm and the infrared wavelength was at λ = 2.97 μm. The cross sections below were averaged over 100 scan lines.

Therefore, in the averaged mode, much thinner films (down to 50 nm thickness) could be characterized, at this resolution, with an absorption sensitivity of about 0.05 %.

8.1.4 Diffraction-induced artifacts in latent image formation

The shrinkage of the polymer in the topographic image of figure 8.6 has 4 weak local maxima (∼3 nm high) along the unexposed lines (light regions). This secondary pattern in the region of the geometrical shadow of the mask may be explained by diffraction of the UV light (250 nm wavelength) on the proximity mask edges and interference of the secondary waves within the geometrical shadow region. In the IR image, the unexposed lines have a comparatively deeper single secondary maximum. It is interesting to note that merely having a lower optical resolution than the topographic resolution cannot explain why the secondary minimum in the absorption image is so deep. Making a convolution of the secondary topographic structure with a large optical aperture would only wash out the structure. The difference suggests that the polymer shrinking does not follow the same dependence on the photochemistry and postexposure bake chemistry, at least at the low exposure levels involving the unexposed areas.

In order to study the origins of these effects a model based on Fresnel-Kirchhoff diffraction for the deep UV irradiation of the polymer through the proximity mask was used. The basic idea behind the Fresnel-Kirchhoff integral is that the illumination at a given point in space arises from the superposition of elementary, spherical waves that proceed from a surface situated between this point and the light source. The Fresnel-Kirchhoff theory is an approximation for the diffraction problem at the mask edges, but numerical simulations based on accumulative propagation of spherical waves as described by Fresnel's principle (figure 8.7) show at least qualitatively good agreement with the observed experimental results. As a second step the related topography image can also be calculated. It is believed that the cause for the shrinkage of the exposed and deprotected regions is due to the chemical process, which releases gaseous isobutylene. Assuming that the number of deprotected sites and therefore the infrared absorption scales linearly with the loss of the gaseous compounds, the topography can be approximated. Macroscopic measurements described later in this work show, that the proportionality between chemical deprotection and shrinkage is well approximated. From the measured UV dose versus shrinkage relation, the topography in figure 8.7 is simulated.

This simple scalar Kirchoff-Fresnel approach for near-field diffraction on amplitude masks therefore indicates the presence of a significant level of UV exposure within the masked

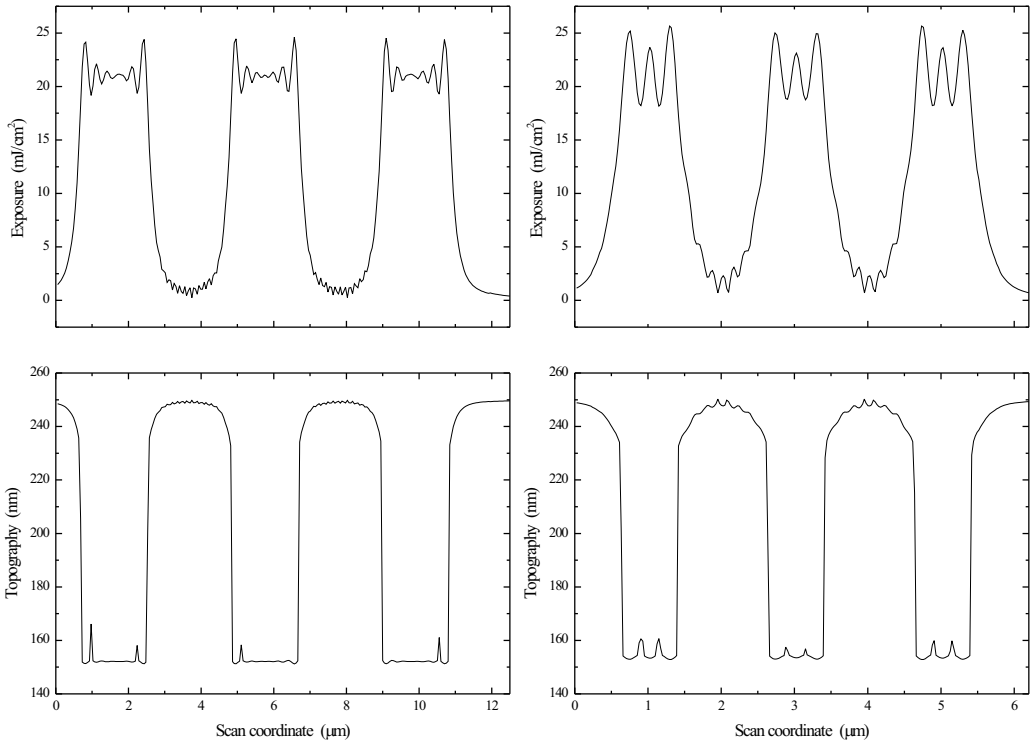

Figure 8.7: Calculated DUV exposure and related shrinkage for 21 mJ/cm^2 intensity at λ = 250 nm. The distance for the proximity mask was assumed to be 250 nm. Mask feature dimension on the left was 2 μm/ 2μm in line/space and 1 μm/ 1μm in line/space on the right.

regions. Since the maximum dose of 21 mJ/cm^2 is close to saturation, a residual UV level in the unexposed regions will decrease the contrast of the latent image with respect to the one expected from a geometrical shadow approach. On larger line/space patterns, as those in figure 8.4, the edge effects at the UV exposure step are not important and therefore the contrast is closer to the value expected from the geometrical shadow model.

8.2 Diffusion properties of chemically amplified photoresists

8.2.1 UV response for poly(t-butoxycarbonyloxystyrene)

Next to the near-field optical measurements, macroscopic studies on photoresist polymers were performed to investigate diffusion properties in the polymer films. With information about the latent image spreading a more complete picture of the mechanisms during the deprotection process is obtained.

Fourier transform infrared spectroscopy was used to study interferometric lithography samples of varying exposure dose and bake times [95]. The instrument allowed lateral mapping of the samples at a low spatial resolution as described in the experimental section.

In a first step experiments were performed to shed some light onto the effectiveness of the incident UV light to photolize the photoacid generators (PAG) in the polymer film, in the following referred to as UV response. For an independent extraction of the UV response curve of PTBOCST, an unpatterned but exposed sample was used. In this case only one laser beam is incident on the surface, leaving a gaussian intensity distribution throughout the sample. Hence it is possible to connect the absorption properties measured locally by the FTIR at any point of the sample with the related UV intensity value. The UV beam intensity was 180 mJ/cm^2 in the center of the sample and the width of the Gaussian beam profile was 8.4 mm. In order to stabilize the sample after exposure it was baked for 30 seconds. Spectra were taken in 0.5 mm steps across the plain sample. Each data point represents the deprotection of the polymer at a different initial UV intensity. In figure 8.8 the transmission at either the CH or the OH absorption band is mapped for different spots along an arbitrary line through the center of the sample. As it is typical for the deprotection chemistry, the CH peak will vanish, therefore indicating the development of the area, while an OH peak will rise at the same time. Also illustrated is the intensity distribution, which allows to connect each transmission value with its specific UV intensity.

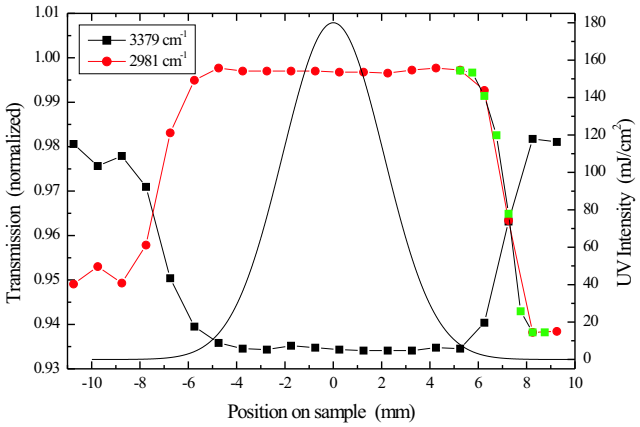

Figure 8.8: Extraction of the UV response for PTBOCST. The measurements were performed by monitoring the OH (3379 cm^{-1}) as well as the CH (2981 cm^{-1}) absorption peak.

Since every photoacid generator, that has undergone photolysis, will lead to a chemically amplified chain reaction with roughly 800-1100 polymer sites deprotected, one can assume a linear relation between transmission and the number of photoacid generators. Hence it is possible to directly express the transmission as concentration of the photoacid generators.

In figure 8.9 the UV intensity dependence of the PAG concentration is shown. The decay of unused photoacid generators can be explained by the following differential equation:

$$\frac{d[PAG]}{dt'} = -C[PAG]I \tag{8.1}$$

The solution is given by a first order exponential function

$$[PAG] = [PAG]_0 e^{-CIt'} \tag{8.2}$$

where $[PAG]_0$ is the initial photoacid generator concentration, I is the intensity and C is Dill's parameter of exposure [96]. While the time of exposure was kept constant for all measurements, the intensity varies due to the Gaussian beam distribution of the UV light. The rms fit of a first order exponential function determines Dill's parameter C to be 0.725 $cm^2/(mJ\ s)$. For PTBOCST, this is in good agreement with other methods published elsewhere [16].
Another more indirect indicator for the chemical reaction is the shrinkage of the polymer after deprotection due to the loss of the volatile compounds, namely isobutylene. Profiling

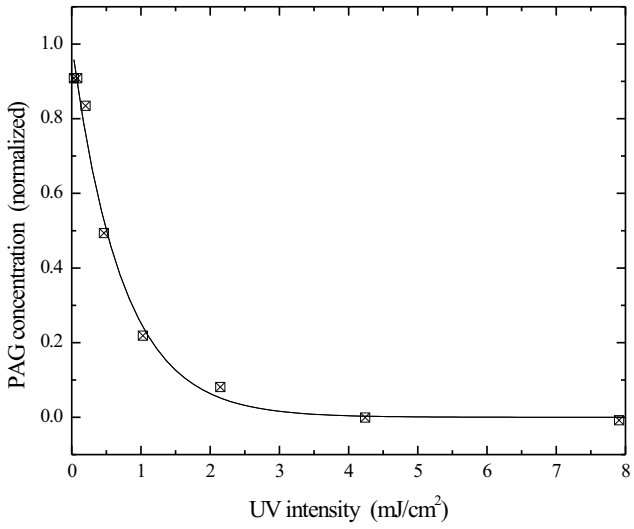

Figure 8.9: The PAG concentration as measured by the transmission change after deprotection for different initial UV irradiations (PTBOCST).

with a tapping mode AFM was done to examine the relationship between topography and infrared absorption locally. For figure 8.10 AFM images were taken along the same virtual line through the center of the sample as it was done for the FTIR measurements. 5 valley-to-top values were extracted from each image and the average trough depth of each sample was plotted as a function of the position on the sample.

The gaussian intensity distribution is implemented in figure 8.10 as well and illustrates a similar trend as seen for the FTIR measurement.

Following the same procedure as for the optical data, the UV dependence of the depth of the troughs is shown in figure 8.10. Increasing valley-to-top numbers that can be well-fitted with a first order exponential function are a good experimental proof for the direct and linear relationship between shrinkage and chemical deprotection process (figure 8.11).

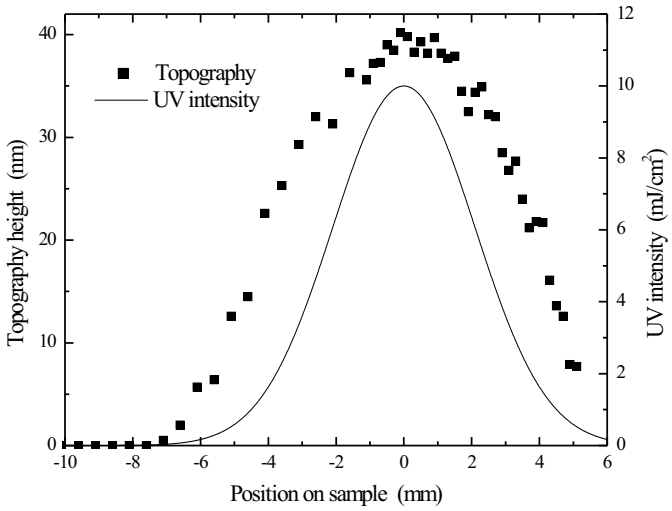

Figure 8.10: AFM-profiling of the sample topography. The measurements were taken from the center of each valley to its highest neighboring plateau.

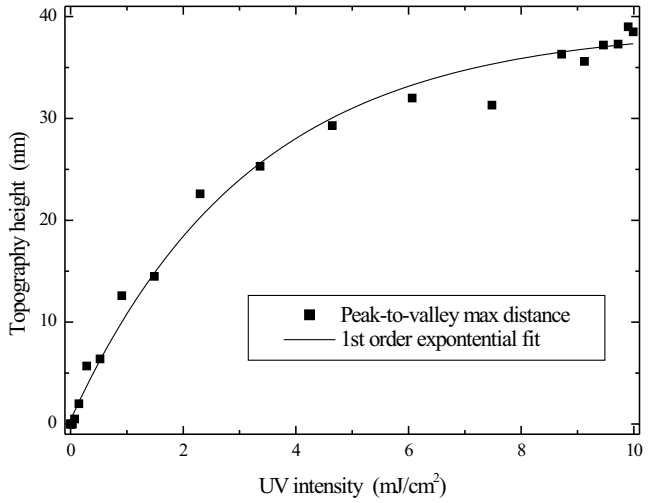

Figure 8.11: UV dependence of topography.

8.2.2 Acid distribution after UV exposure

For a second experiment the deprotection is modelled throughout the sample for the case that two laser beams are overlapped under a small angle and interfere on the surface of the sample. Including the above response in equation 4.2 leads to the following equation

$$PAG(x) = PAG_0 \exp\left(\sin^2\left(\frac{2\pi\sin(\theta)}{\lambda}x\right)e^{-\left(\frac{x}{A}\right)^2}\cdot C\right) \tag{8.3}$$

and represents the actual initial photoacid generator distribution for the interferometrically written lithography samples. The principle distribution is shown in figure 8.12. For better illustration a bigger periodicity of the fringe pattern was chosen. Resulting from an illumination with 257 nm a period of 972 nm would be expected. In order to show the effect of deprotection saturation on single fringes the periodicity was arbitrarily changed in figure 8.12, so only a few fringes are seen. Nevertheless the envelope over all fringes will stay the same regardless of the number of fringes. For the extraction of the diffusion coefficients later the original periodicity of 972 nm was used as expected experimentally.

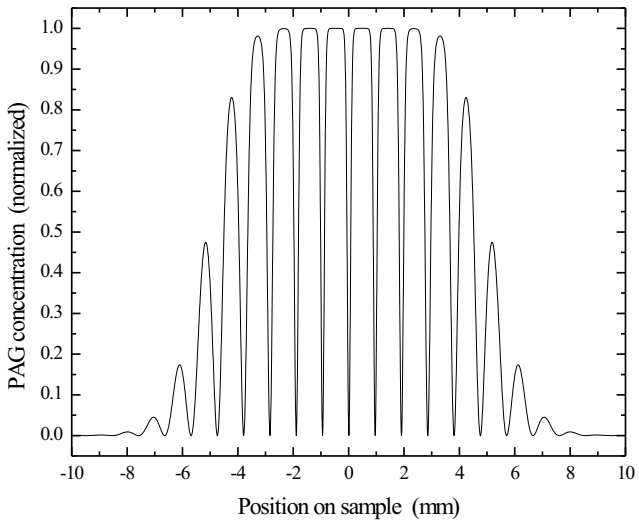

Figure 8.12: Calculated PAG distribution for interferometric lithography. The periodicity was changed arbitrarily in this graph by 10^4, so the shape of single fringes becomes obvious.

A more detailed look at the photoacid generator distribution is given in Figure 8.13. Here a single feature from one period near the center of the sample (maximum irradiation with

10mJ/cm^2) is shown. An obvious broadening of the photolized feature can be seen, which transforms the original sinusoidal behavior of the UV intensity into a very asymmetric periodic pattern. The full width at half maximum value of troughs near the center of the sample are as small as 140 nm. While this kind of illumination technique allows for writing of very narrow features, it is important to study the diffusion mechanisms during the following baking process, since the above width only represents the initial PAG distribution.

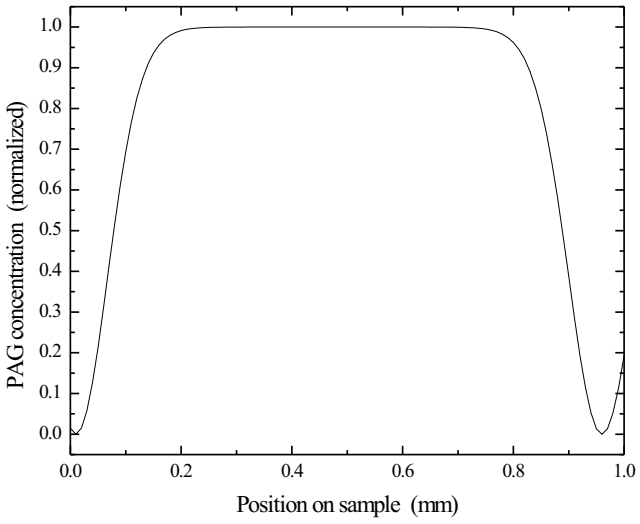

Figure 8.13: A single fringe from the center of the UV illumination spot is magnified. As one can see the width of the deprotected area appears much broader than the narrow troughs.

8.2.3 Latent image spreading under the influence of bake time and UV intensity

With the original photoacid generator distribution known, follow-up samples with the exact same exposure conditions but varying post exposure bake times were prepared. By varying the bake time it is possible to determine the kind of diffusion that happens during the deprotection process. In case of Fickian diffusion, the diffusion coefficient D can also be extracted. Knowing the average distance L that the diffusing particles travelled during

the time t, the diffusion constant is given by

$$D = \frac{L^2}{2t}. \tag{8.4}$$

The FTIR measurements represent the infrared transmission at either the CH or the OH resonance. Depending on which absorption line is monitored, an increase (CH) or a decrease (OH) is seen in transmission respectively. The change in transmission is directly linked to the amount of deprotection of the original polymer. As long as there is enough unprotected polymer available, such that diffusion during the bake process will lead to more deprotection, the length L is directly proportional to the transmission.

Figure 8.14 shows the absorbance for the CH peak (2981 cm^{-1}) as function of the position of the sample for the PTBOCST polymer system. Each differently colored graph represents a unique sample, that was exposed under the same conditions as the other samples but post-exposure baked for the time displayed in the graph. The figure already illustrates qualitatively the influence of longer baking as the absorbance change becomes more pronounced. The same measurements were done for the PTBMA photoresist and are depicted in figure 8.15.

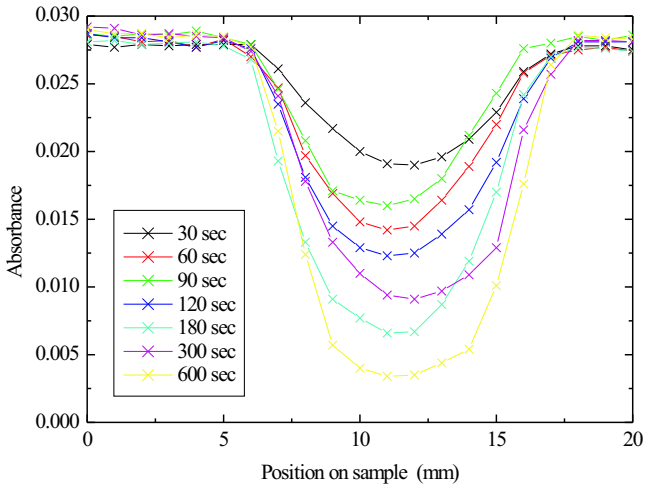

Figure 8.14: PTBOCST samples were prepared at different bake times. The absorbance at the CH peak (2981 cm^{-1}) is monitored along a center line of each sample.

For the direct linkage between the average travelling length L and the measured transmission the acid distribution for at least two different bake times needs to be calculated, so a

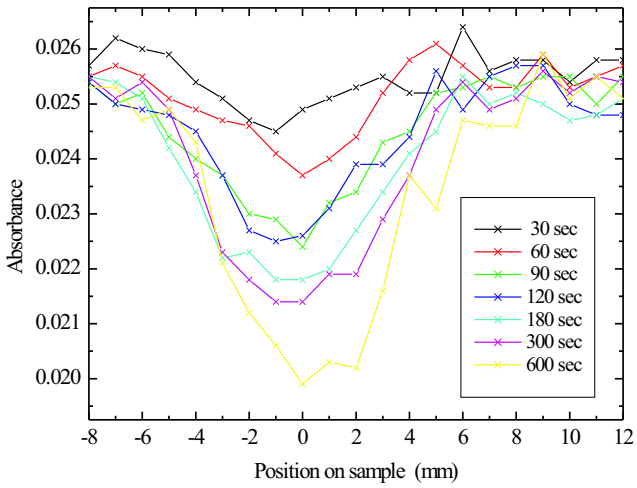

Figure 8.15: PTBMA samples were prepared at different bake times. The absorbance at the CH peak (2935 cm^{-1}) is monitored along a center line of each sample.

calibration in units of length can be obtained. Equation 8.3 provides the local acid distribution in the polymer film after baking of 30 seconds. As the second bake time estimate the moment that diffusion filled in the fringe pattern in the center of the sample is chosen. This point is reached when the transmission does not change anymore upon longer bake times and is reached in this case after 775 seconds. Knowing the area that is governed by diffusion during this time interval allows for an absolute calibration of the parameter L.

With the measurements shown in figure 8.14 and 8.15 a complete dataset is on hand to describe diffusion during the deprotection process. The measurements contain feature broadening as a function of bake time and also as a function of UV intensity. After performing the transmission-to-length calibration, the length can be plotted in relation to the bake time, allowing a direct extraction of the diffusion constant D.

Figure 8.16 shows the behavior for the PTBOCST/PFBS system. The transmission axis is already converted to length squared as described above. For better illustration scans are plotted at only 4 different UV intensities, while the complete dataset contains far more scans to cover the whole intensity range from 0 to 10 mJ. All scans can be well fitted with linear fits, even though systematic errors can be seen at each baking time interval. Also noticeable is, that the inclines of the fits change with UV intensity, which results on first

sight in different values for the diffusion coefficients depending on the illumination. The greatest diffusion coefficient, that can be reported from figure 8.16 is $4.5{\cdot}10^{-14}$ cm^2/s.

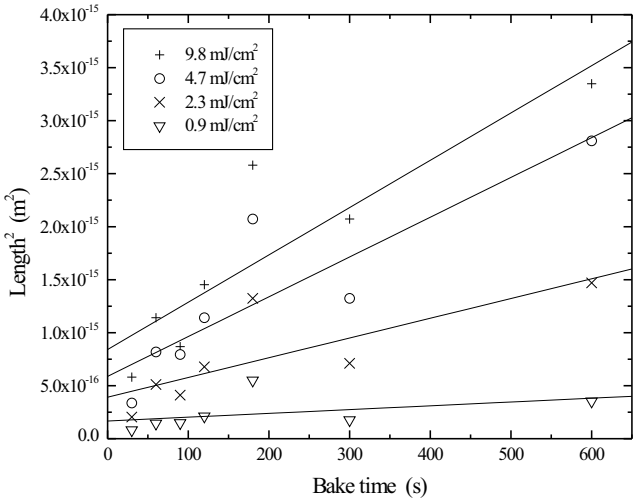

Figure 8.16: The image spreading in PTBOCST is shown for varying bake times and changing UV intensities.

Sources of error are uncertainties in applying exactly the same post exposure bake conditions to every sample. One of the difficulties is to control exact baking parameters for all samples, which leads to errors in the bake time and therefore uncertainties in the diffusion coefficient. This systematic error becomes obvious in figure 8.16 and 8.18 as the deviation for all measurement points at the same bake time shows the same direction. Also the film thickness of each sample can differ slightly. These errors are difficult to quantify but can be diminished by more advanced preparation techniques. The error of the measurements on the other hand is very small and mostly dominated by the exact placement of the FTIR aperture on the sample. The accuracy is given by the manual translation unit and is better than 100 μm. This leads to an equivalent maximum uncertainty of 2 % for the UV illumination.

The influence of the UV intensity is an important mechanism since the UV light prepares an initial acid distribution, which is key to the following diffusion during the PEB process. With a high concentration of PAGs, the average distance between two photoacid molecules is small, so that the polymer flanked by them is deprotected fairly quickly. With less UV irradiation fewer PAGs undergo photolysis and therefore bigger volumes have to be covered by diffusion to deprotect the irradiated area completely. After this

initial deprotection of the irradiated volume, further diffusion is only measurable outside the illuminated areas. Diffusion still happens inside the deprotected volume, but acid that is present in an already deprotected environment does not contribute to any further chemical changes of the polymers - hence it cannot be detected by this experiment. As a consequence further deprotection only appears along the borders of the irradiated and deprotected features. The probability for the diffusing acid molecules to find a still protected polymer is diminished if compared to the initial state described above. Since the measurements rely on mapping the amount of original and deprotected polymer as a result of acid presence rather than the acid itself, the diffusion constants appear to depend on the initial acid concentration, hence on the UV intensity. Figure 8.17 illustrates how the diffusion constant seems to rise linearly with increasing UV intensity up to a maximum where it stays constant regardless of further intensification of the UV beam. This saturation is equivalent to all PAGs being photolyzed. More intensity does not lead to more initial acid molecules. A closer look at the simulated pattern in figure 8.12 reveals that the fringe maxima reach saturation for intensities at about 4 mJ/cm^2 and higher. This saturation level also describes the point in figure 8.17, where the diffusion constant does not change upon higher UV dose.

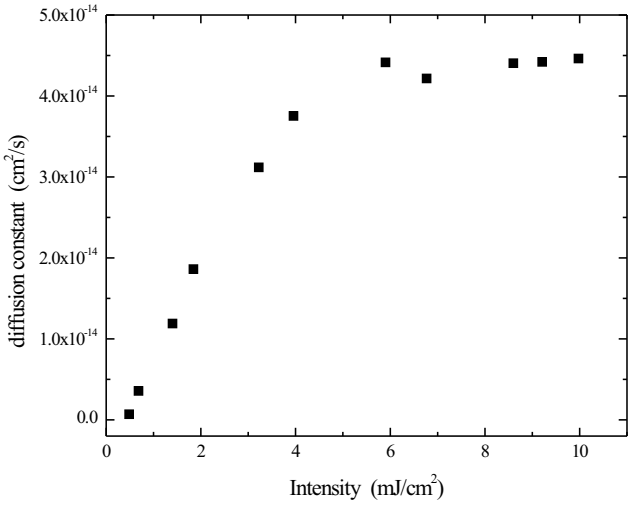

Figure 8.17: Depending on the amount of initial PAGs prepared by the UV intensity, the measured diffusion constant seems to change. While this is an artifact that can be explained with the measurement, an estimate for a necessary minimum exposure for PTBOCST can be derived.

This measurement illustrates the necessity for high optical contrast and enough light intensity to saturate the photoacid generators at sites that are to be deprotected. In this case the concentration of photoacid generators was high enough, that no measurable diffusion is necessary in case of saturation to deprotect the illuminated area completely.

The PTBMA/PFOS system was also investigated. The bake time dependent graph can be seen in figure 8.18. Next to the systematic errors, which are also present in the PTBOCST system, the plot does not show linear behavior. Therefore the use of equation 8.4 to extract diffusion constants is not possible, implying that the diffusion is influenced by other mechanisms and cannot be described by the Fickian case I model.

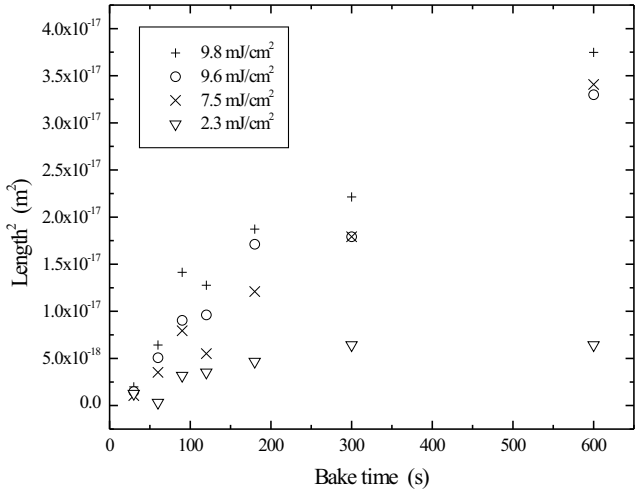

Figure 8.18: The image spreading in PTBMA resist is shown for varying bake times and changing UV intensities.

The measured maximum diffusion constants for PTBOCST are in good agreement with the work of other groups, even though the PEB conditions of this work were set at a higher temperature. Itani et. al. [31] and Houle et. al. [34] report diffusion constants of about $3{\cdot}10^{-14}$ cm^2/s for PEB temperatures around 90^o C measured with ion conductivity (Itani) and spectroscopic methods combined with a kinetics model (Houle) respectively. The PTBMA data on the other hand shows a definite nonlinear behavior and therefore suggests that the diffusion in this case does not follow the Fickian case I model. One of the reasons is certainly that the baking temperature was chosen slightly above the glass transition for PTBMA, which was necessary to fuel further deprotection by thermolysis in this specific system.

9 Imaging with apertureless near-field optical microscopy

9.1 Gold islands on glass surface

Imaging with apertureless near-field optical microscopy promises superior optical resolution over any other microscopy technique. Due to the reduction to a localized dipole field, where the confinement is mainly controlled by the tip diameter of the emitting antenna, optical resolution as small as 1 nm has been reported in literature [97, 59]. Theoretical evaluations of the tip-sample interaction even predict the possibility of optical atomic resolution. [59]

Unfortunately experimental limitations, that are not accounted for in the calculations, raise pretty high barriers, which are to overcome from an experimentalists point of view. The reasons for not reaching the theoretical limits are manifold and only few of the major obstacles are mentioned in the following:

- Intensity of the light source and effective power delivery to the probe,
- incoming light geometry for dipole excitation,
- multiple reflection at substrate surfaces,
- stability of the optical beam path (interferometric detection scheme),
- Shot-noise of the detectors,
- field enhancement in the tip only occurs if the tip material encounters plasmons due to correct wavelength and is able to radiate resonantly due to size.

With all this in mind, it is important to first have a closer look at the performance of an apertureless near-field optical microscope. Hence samples are needed, that have small enough features to probe the lateral resolution limit of the instrument and high optical contrast with very little topography as well. A promising candidate for such a sample was first examined by VanDuyne and coworkers [98]. Regular patterns of small metal islands were deposited on dielectric surfaces to study single molecules by attaching a few molecules

to each island. Other experiments were conducted to understand the behavior of localized surface plasmons. And last but not least the method, which was introduced to pattern the surface, is thought to be a good way of nanostructuring surfaces for other applications.

The preparation of small, regularly spaced metal islands follows the subsequent procedure. A substrate (glass cover slips in this case) is cleaned by sonicating it in acetone to remove any protrusions and obtain a flat surface. Polystyrene spheres of 1 μm diameter, which are commercially available as immersions with well characterized size distributions, are spin-coated on the glass surface to manufacture a closely packed monolayer of spheres as depicted ideally in figure 9.1. Another way of depositing the polystyrene balls is to prepare a very dilute immersion of the original concentration and evaporate it off of a tilted substrate. By heating the sample, the liquid vanishes, while the spheres gain enough thermal energy to move around on the surface and organize themselves in a hexagonally packed structure with the least surface energy possible.

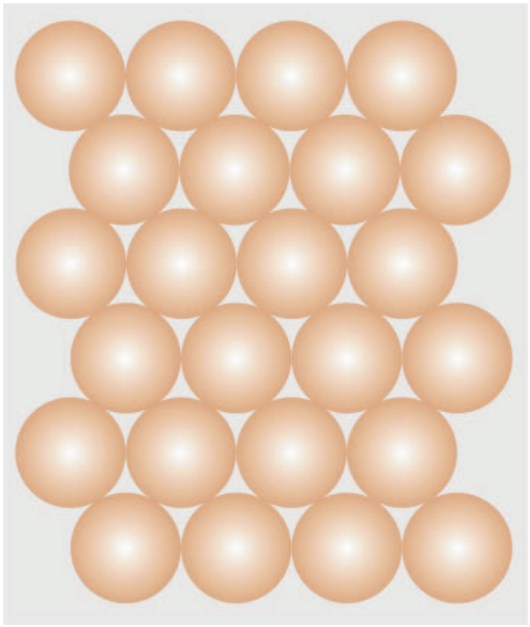

Figure 9.1: Ideally the spheres will be packed in a hexagonally closely packed monolayer, leaving a regular pattern of small holes, that fill with gold upon coating.

For the final sample preparation the polystyrene is only used as a mask for the following step of metal deposition. The metal coating is typically done by evaporative deposition or chemical vapor deposition (CVD), which depends on the metal that is to be used. In any case the collimated beam of metal vapor can only reach the top of the flat substrate

in the small areas between the spheres. The height of those little islands is controlled by the amount of metal deposited. For very small amounts the islands appear flat, while bigger amounts cause the shape of the islands to be pyramidical. In a final step the polystyrene spheres are removed in an ultrasonic bath of acetone. Depending on the follow-up implementations, people have also annealed the patterned surface afterwards, which leads to smoothing of the island edges.

For this work, gold was deposited at a very thin layer of 3 to 5 nm to ensure topographically flat samples. The self organization of the spheres was less than optimal, which lead to a loosely-packed assembly on the surface with only pockets of hexagonal packs. The reason was probably that the surfaces of the substrates were not clean enough. Hydrophilic groups can attach to certain sites of the silicon crystal structure, which makes the glass surface an area of strong Van-der-Waals forces and therefore prohibits the free motion of the polystyrene beads on the surface. Chemical passivation of the substrate prior to deposition of the spheres would minimize the attraction of the surface and ensure unperturbed motion in the lateral plane. Figure 9.2 shows two areas on the patterned surface, that were imaged by conventional microscopy. The gold-coated areas appear dark, while the blank substrate is bright in contrast. Especially in the right image areas can be found that show regular patterns left by the deposited polystyrene spheres.

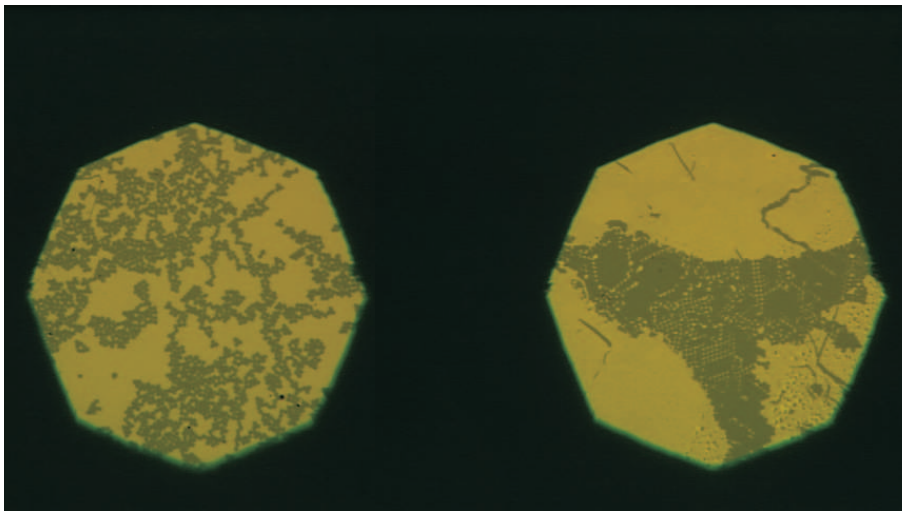

Figure 9.2: Conventional microscopy on gold-coated nanopatterned substrate after removal of the polystyrene beads. The right image shows small areas of regular patterning due to self-assembly of the spheres.

It can also be seen that even in the case of the regularly patterned area, a lateral

distance between spheres was present, which can be attributed to electrical charges on the polystyrene beads and leads to compulsion between them.

In a first approach apertureless NSOM images were obtained by detecting the optical signal at the modulation frequency of the tip (figure 9.3 and 9.4). For topographic tracking the tip was dithered at its mechanical resonance at about 65 kHz and a closed feedback-loop kept the tip in proximity of the surface. The damping of the tip was set, so the tip monitored the topographic changes by either non-contact or slight tapping mode. In addition to the resonant dither frequency a slow modulation of 2.5 kHz was impinged on the vertical motion of the AFM tip. The amplitude of this non-resonant motion was measured interferometrically to be on the order of 2 to 5 nm, while the resonant amplitude varied between 5 and 10 nm [99, 100]. Next to this small amplitude, which allows to probe the short-ranged dipole coupling, the low frequency was also necessary for the 2f detection. The lock-in amplifier could simply not demodulate signals beyond 102 kHz. Regarding the probe, in most cases standard silicon AFM tips were used, which were coated with a 10 to 15 nm thick layer of gold in an evaporative coater. The metal coating is predicted to enhance the dipole field of the tip, but on the downside also causes the AFM tip to have a tip apex diameter of about 30 nm. As a laser source an intensity-stabilized He-Ne laser with 1 mW output power at $\lambda = 633$ nm was used. The above settings were used generally for all measurements presented in the following sections.

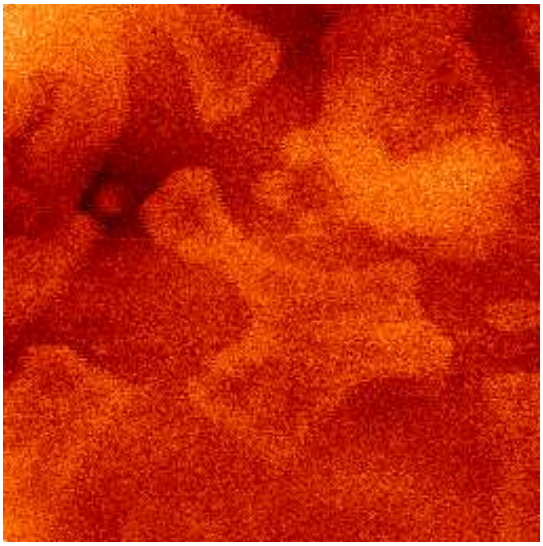

Figure 9.3: Apertureless NSOM: optical image 2 μm $\times$ 2 μm, first harmonic.

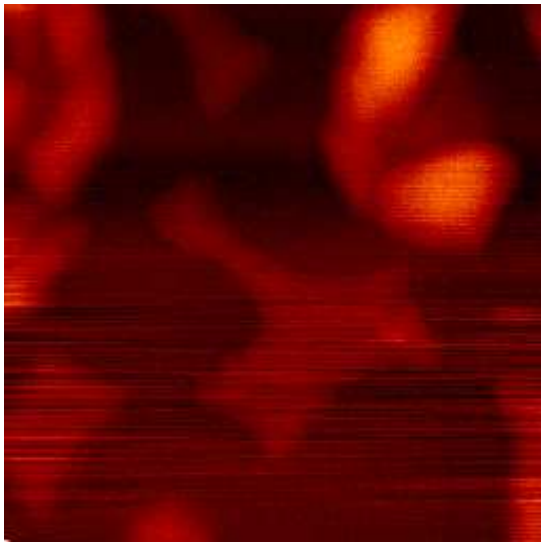

Figure 9.4: Apertureless NSOM: topographical image 2 μm $\times$ 2 μm.

The topographic image does not show the regular pattern one would have hoped for from the samples described before. Nevertheless, gold structures of very small dimensions can be found and are therefore a good playground to estimate resolution limits of the microscope. The scale spans about 10 nm, with most features being about 4 nm high, which is in good agreement with the settings for the metal deposition. Comparing the optical output on the left with the topography, three major remarks have to be pointed out. First, an obvious feature broadening is apparent in the optical signal. A closer look reveals, that the broadening is on average about 30 nm, which matches well with the probe size. Second, the edges of the gold structures cause an optical contrast enhancement, which can be seen throughout the image. Another important fact is, that features are present in the optical image without a counter fit in topography. Hence optical contrast shows details about the sample, which can not be accounted for in a topography scan.

To better quantify the image spreading and edge enhancement, one arbitrarily chosen line was extracted from the images and is plotted in figure 9.5. Clearly two features, centered around position 0.6 μm and 1.1 μm, show the same behavior as described above. The optical signal increase almost by a factor of 2 at the edges of the gold pattern, but only shows slightly higher intensity once the tip is placed on the gold structure away from any edges. It is predicted theoretically that enhancement of the optical signal is a probable mechanism for optical contrast in apertureless NSOM. Similar to the tip, an edge also represents a discontinuity for the electromagnetic waves. Hence confinement effects as observed for the localized dipole in the tip can enhance the tip-sample dipole coupling in the presence of a metal edge. Another reason could also be a topographic artifact induced by the fairly broad AFM tip. Both features in the linescan show very moderate slopes for the topography, while the optical signal reveals almost discrete changes in intensity for the same positions.

In order to rule out topographic influences in the optical signal, scans were performed, while detecting the optical signal at twice the modulation frequency. As estimated in the theory chapter before, contributions from topographic influences should be neglectable as long as the tip-sample distance is short compared to the wavelength used. The images in figure 9.6 and 9.7 are centered over a site, which was covered by a polystyrene sphere before. The dimension of this circular gold pattern matches exactly the diameter of the used beads. The tiny elevation in the center, which is only visible in the topography, is probably leftover material from the removal process and is not covered by gold.

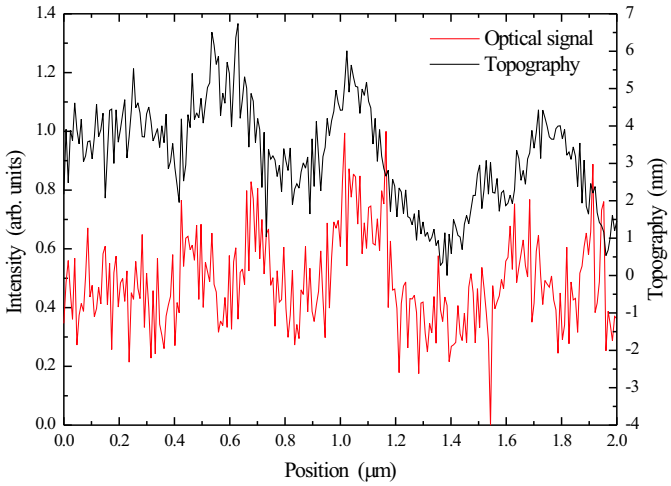

Figure 9.5: Extracted linescan from the images before. The curve in red shows the optical signal, the black one is the topography.

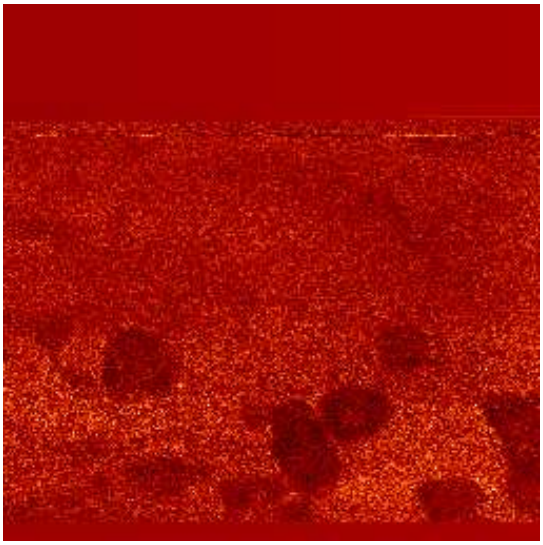

Figure 9.6: Apertureless NSOM: optical image 2 μm $\times$ 2 μm, second harmonic.

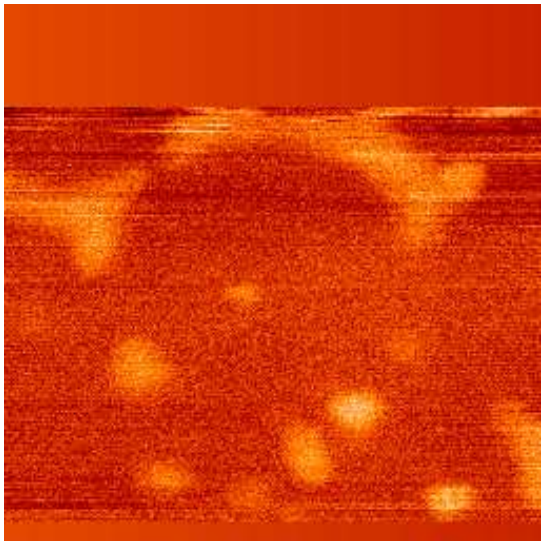

Figure 9.7: Apertureless NSOM: topographical image 2 μm $\times$ 2 μm.

Drifts in both, the topographic and optical signal have rendered the beginning and the end of the scan useless, but these images seem to contain good evidence that artifact-free optical imaging with apertureless NSOM is possible. Again a horizontal line from the lower third of the images was extracted and plotted in figure 9.8. The most pronounced feature centered around 1.7 μm shows sharp edge tracking for both, the optical and topographic signal. This by itself would not be proof for artifact-free imaging, but it is apparent, that the topographic width is quite a bit narrower than the optical one. Interestingly the strong optical contrast does not appear, while the tip is still on the downward slope, but changes its value only after the feature is not present in the topographic signal. Hence the optical and topographic signal are decoupled at least for structure heights that are small compared to the wavelength of the light used. The 2f linescan also allows an experimental estimate of the optical resolution limit of the apertureless NSOM. With the assumption, that the gold features represent a step-edge at their borderlines, the optical response of the instrument can simply be extracted from the slope at those edges. By analyzing several edge responses from 2f linescans an optical resolution of about 30 nm was found. This result matches well with the tip apex diameter, which should also limit the resolution of apertureless near-field optical microscopy theoretically.

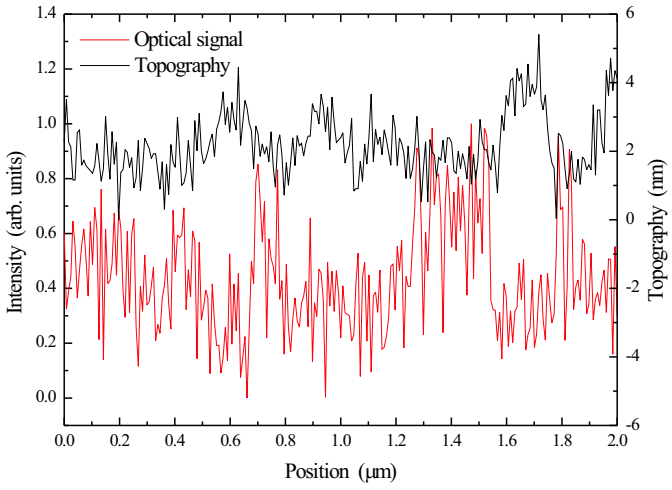

Figure 9.8: Extracted linescan from the images recorded at twice the tip modulation. The curve in red shows the optical signal, the black one is the topography.

9.2 Diblock copolymers

Copolymers have interesting properties regarding the nano-structuring of surfaces. In bulk, it is known, that diblock copolymers organize in microdomains, after segmentation of the two polymer components has occurred [101, 102]. Upon phase separation, the linkages between the blocks are arranged along the borderline of the phases, which leads to a brush-type micro-structure. By connecting the two different polymers by covalent bonding, the polymers are forced to organize themselves on a molecular level [103]. With one of the components being polar and the other not, several copolymers can aggregate to what is generally referred to as micelle. A micelle consists of a controlled number of diblock copolymers, which has a core (consisting of block polymer type A) and an outer shell (made out of polymer type B). In ultrathin films, monolayers of micelles can be formed by spin-coating very dilute solutions onto a substrate. Due to minimizing of the surface energy, a regular pattern of these aggregations can be achieved. This mechanism leads to formation of chemically heterogenous more or less regular surface patterns and is thought to be used in future for structuring and chemical patterning of surfaces. By chemical modifications, the core of the micelles can also contain anorganic salts, where these salts on the other hand can have metallic components. Therefore metallic nanoclusters can be delivered on a surface and be self-organizing due to the chemical nature of the diblock copolymers, which are surrounding them. The size of these nanoclusters can be controlled by the amount of salt attached to each micelle and allow size distributions within a few nanometers. In summary a micelle can be thought of as a template, that forms a regular structure on the surface of a substrate, therefore allowing other chemical compounds to be positioned in nanostructured environments [104, 105].

The copolymer used in these experiments was made of polystyrene(1350)-b-poly(2-vinylpyridine)(400), in short PS-b-P2VP. Ultrathin films with monolayer aggregations could be formed by spin-coating very dilute solutions of the copolymer on atomically flat surfaces as found the easiest on freshly cleaved mica. In order to obtain a surface pattern that corresponds to a minimum in free energy, the samples were annealed at 150^o C. In figure 9.9 the aggregation of copolymers on the mica surface is imaged by atomic force microscopy. The left image shows the topography of the sample, while the image on the right is obtained in phase contrast. Noticeable are core/shell structures of each micelle, with the core being 5 to 8 nanometer high and the outer shell only forming a flat area of about 1 nm height. Several aggregations can be found with slightly different sizes and the tendency to form a closely packed monolayer of micelles becomes obvious for example in the center of the image. In phase contrast the dimension of each shell is even better visible, also showing that a monolayer density is reached locally in the center

of the sample. Typical lateral dimensions of the micelles are found to be 100 nm for the core diameter and 200 to 300 nm for the whole micelle.

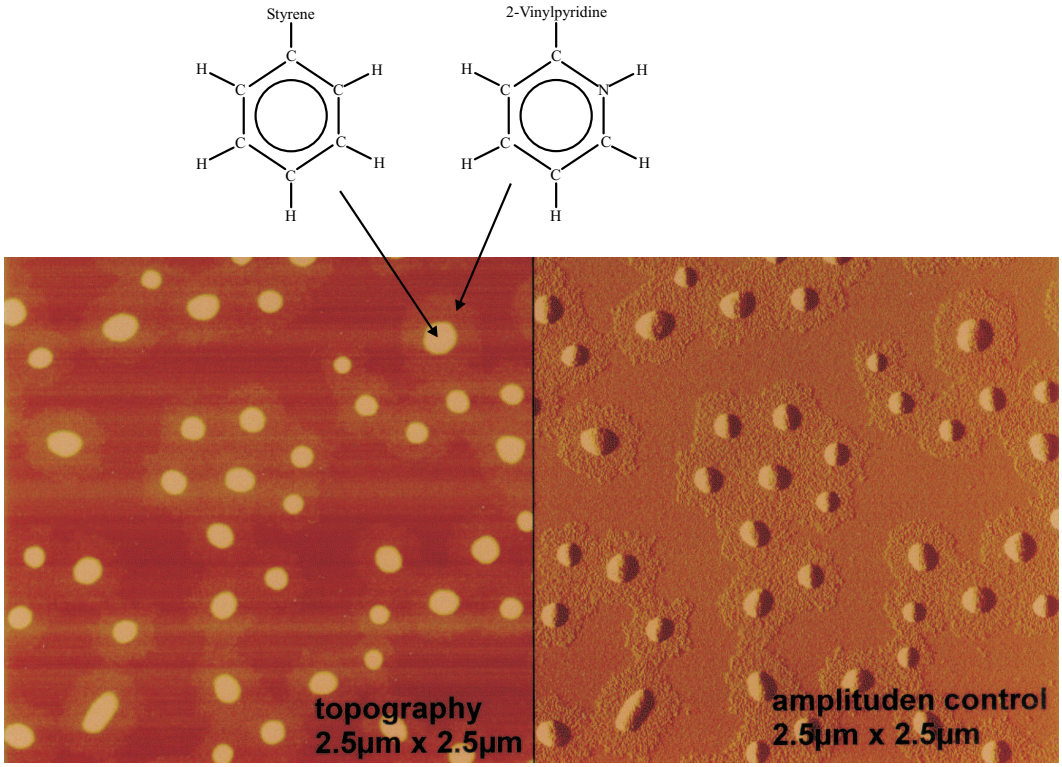

Figure 9.9: Aggregation of 2-block copolymer on mica.

Imaging a monolayer surface pattern of diblock copolymers by other means than atomic force microscopy and its related contrast mechanisms is a very difficult undertaking. Even though polystyrene as well as poly(2-vinylpyridine) have very specific infrared absorption lines, examination with the infrared absorption based near-field optical microscope is not possible due to the ultrathin structures, which lead to a theoretical absorption contrast of less than 0.01 %. Also the substrate made from mica is not suitable for transmission experiments in the infrared, since mica has an opaque window right around the interesting wavelength region of our infrared laser source at 2.8 μm. Even another obstacle is the lateral resolution as determined before, which is found to be around 300 nm. For feature sizes small compared to the optical resolution only a washed out contrast - with the tip aperture defining the observed structure size - can be expected.

Apertureless near-field optical microscopy on the other hand seems to offer quite a few promises for imaging diblock copolymers aggregations on surfaces. As shown in the theory section, apertureless NSOM is very surface sensitive, because the probe is only interacting

with a small sample volume, which is comparable to its smallest diameter. It would be best to examine the polymers at their specific infrared absorption bands since the dipole coupling and therefore the optical contrast is expected to be big. But imaging in the visible wavelength range can also lead to differentiation between the two polymer chains. This optical contrast can be explained by the complex nature of the index of refraction and therefore the connected material specific dielectric constant. With the complex refractive index the wavelength dependent absorption and index of refraction changes are expressed. Kramers and Kronig showed that contributions of the complex refractive index in the infrared regime have an influence on the optical properties in other wavelength ranges and vice versa. This is expressed in the Kramers-Kronig relations, which connect the real and imaginary part of the index of refraction.

$$n(\omega) = 1 + \frac{1}{\pi} \int_{-\infty}^{+\infty} \frac{k(\omega')}{\omega' - \omega} d\omega' \tag{9.1}$$

$$k(\omega) = -\frac{1}{\pi} \int_{-\infty}^{+\infty} \frac{n(\omega') - 1}{\omega' - \omega} d\omega' \tag{9.2}$$

Connecting the two expressions, for example the reflectivity of a sample at a specific wavelength can be expressed. The reflectivity is defined as

$$R = \frac{|E_{refl}|^2}{|E_{in}|^2}, \tag{9.3}$$

which can also be expressed as

$$R = \left| \frac{1 - \kappa}{1 + \kappa} \right|^2 \tag{9.4}$$

$$= \frac{(1-n)^2 + k^2}{(1+n)^2 + k^2} \tag{9.5}$$

With the help of the Kramers-Kronig relations the reflectivity can be expressed for example as a function of wavelength:

$$R(\omega) = \frac{\int_{-\infty}^{+\infty} \frac{d\omega'}{\pi^2} \left(\frac{k(\omega')}{\omega' - \omega} \right)^2 + k^2}{\left(2 + \int_{-\infty}^{+\infty} \frac{d\omega'}{\pi} \frac{k(\omega')}{\omega' - \omega} \right)^2 + k^2} \tag{9.6}$$

This suggests that an optical contrast can be observed even though no direct absorption is present in the visible wavelength range. Another mechanism measured experimentally [106] and also shown by numerical simulations [107, 108] is thought to rely on the

fact that the dipole interaction between tip and surface inhibits enhancement, which is contributed to antenna resonances as well as plasmon resonances in the half-sphere of the end of the probe and depends strongly on the dielectric constant of the tip and the local area on the sample [86, 61]

In figure 9.10 and 9.11 the optical and the topographic image of a 1 μm $\times$ 1 μm scan on PS-b-P2VP diblock copolymers is shown. The optical signal was recorded at the vertical tip modulation frequency of 2.5 kHz with an amplitude less than 2 nm. As a light source the intensity-stabilized He-Ne laser was used at λ = 633 nm and output powers of P = 1 mW. The AFM tip was coated with a 10 nm thin layer of gold, which increases the tip diameter to be on the order of 30 nm. Other tips, which were coated under the same conditions, were examined by scanning electron microscopy and showed all very similar dimensions. It has to be noted that 30 nm was also the resolution limitation of the SEM, therefore tip diameters could be smaller than characterized by this method. The topographic image was obtained simultaneously with the tip dithered at 65 kHz, which was used for the feedback based tracking of the topography. Polymer aggregations are clearly visible in either the optical and the topographical image. Their dimensions suggests, that only the core is mapped by the instrument, with the height of the features being around 6 to 8 nm and the diameter measured to be of 100 nm. The dielectric particle of about 80 nm height on the right side of both images makes it difficult to scale the images to a good contrast but is also a strong indicator for optical contrast, that is induced by topographic changes in the scan.

Measurements throughout the sample showed similar results, but due to drifts of the tip in the focus of the laser beam and because of instabilities in the AFM topography control it was almost impossible to obtain complete images without discarding scans before completion.

The theoretical estimate that detecting the optical signal at the second harmonic rather than the modulation frequency itself, suggests that contributions from topographically induced artifacts can be minimized for tip-sample distances much shorter than the wavelength. Since this is the case with nominal average gap sizes of 2 to 5 nm, measurements were also performed by detecting the optical signal at twice the modulation frequency. The images in figure 9.12 and 9.13 are based on the second harmonic detection and inhibit some interesting results.

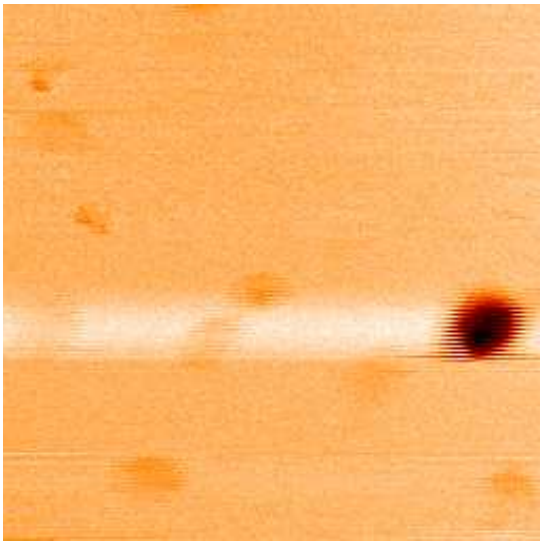

Figure 9.10: Apertureless NSOM: optical image 1 μm $\times$ 1 μm, first harmonic.

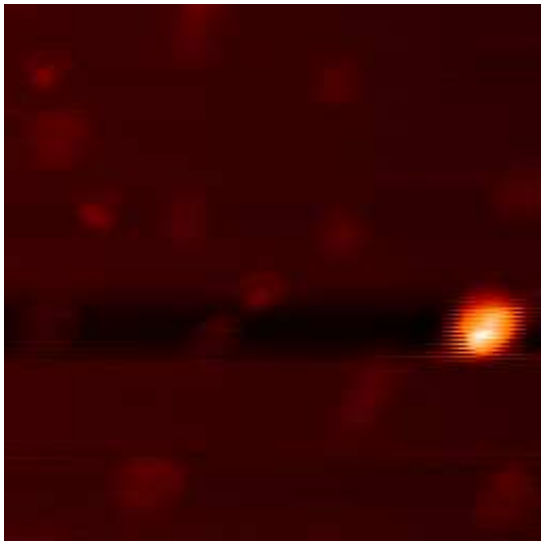

Figure 9.11: Apertureless NSOM: topographical image 1 μm $\times$ 1 μm.

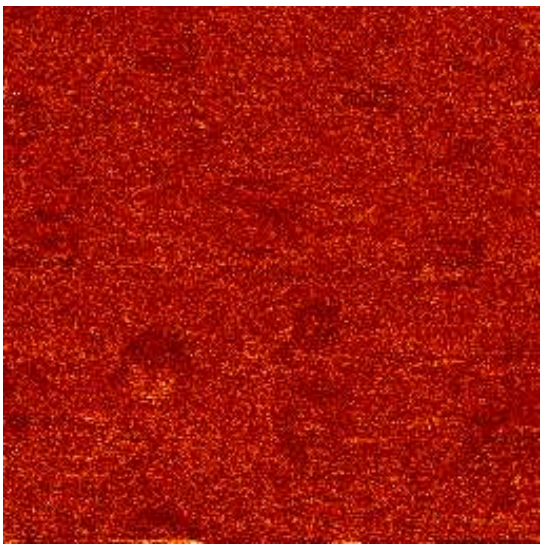

Figure 9.12: Apertureless NSOM: optical image 1 μm $\times$ 1 μm, second harmonic.

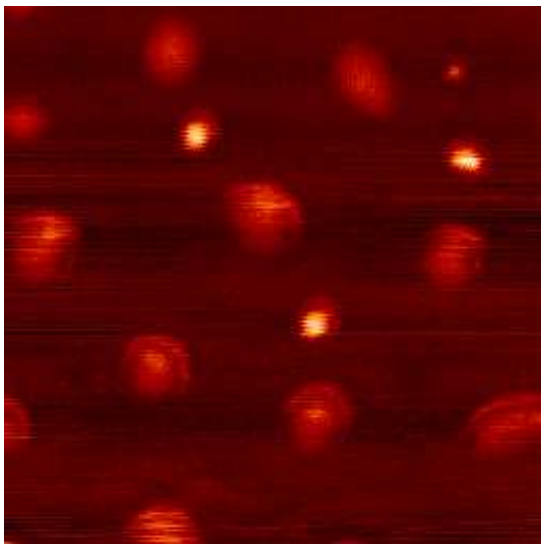

Figure 9.13: Apertureless NSOM: topographical image 1 μm $\times$ 1 μm.

The absolute amplitude of the second harmonic signal dropped by about 2 orders of magnitude compared to detection at the main modulation frequency. The 2f-signal was only five times bigger than the shot-noise level of the silicon photodiodes that were used. With such a poor signal-to-noise ratio it is not possible to give good estimates about the optical contrast. On the other hand, looking at the data qualitatively, some interesting conclusions can be drawn.

Compared to the image in 9.11, the features in figure 9.13 show more details and most of them can be divided into a core and a shell as expected from the AFM scans earlier. The shells appear not as wide as the AFM image suggests, but this can be easily explained by the shape of the AFM tip, which is fairly big in diameter due to the gold coating. As shown before the image process is always a convolution of the tip curvature with the shape of the feature. In case of features being small compared to the probe, the convolution becomes visible and is certainly the explanation for the apparent projection. However, a few structures appear smaller in lateral dimension by a factor of 2, but also increased in height. These features are about 20 nm higher than other features on the sample surface. While it is difficult to explain the appearance of two different forms of polymer surface aggregations, which probably has to be attributed to the initial micelle aggregation during the annealing process, the optical response to these features is quite remarkable. It seems that the optical image is not affected by different topography, but instead shows similar optical contrast for features regardless of the absolut height. This is a strong indicator that the image contrast in second harmonic detection is not heavily dictated by topographic artifacts. Another reason to believe that topographically induced contrast can be ruled out in the optical scan is given by the fact that the drifts in the topographic image do not find an corresponding change in overall optical intensity. Hence the experimental results give at least a qualitative agreement with the theoretical prediction [109].

9.3 Photoresist polymer structures imaged by ANSOM

With the promising results found by imaging the thin diblock copolymer films in the previous section, apertureless near-field optical microscopy was also applied to photopolymer resists studied by other methods in this work.

The same samples were used as described in section 8.2. The decision was made for the interferometrically written line structures over the contact-mask ones, due to the

narrower features and the already well characterized distribution of the different chemical compounds. The images in 9.14, 9.15, 9.16 and 9.17 were taken in the center of a patterned sample made from PTBOCST, which was post-exposure baked for 30 seconds. The short bake time assured that diffusion did not cause much line broadening, therefore the concentration of deprotected polymers is described by the calculated profile shown in figure 8.12.

Images were taken under the same conditions as described in the previous section. Figures 9.14 and 9.15 show a 3 μm $\times$ 3 μm scan with the optical image recorded at the modulation frequency of the probe. The topography reveals a feature depth of approximately 40 nm, which is substantially less than the shrinkage expected from the gaseous losses during the deprotection process. This can be attributed to the relatively big diameter of the AFM tip, so the bottom of the troughs cannot be reached entirely by the tip. A situation like this is prone to optical contrast induced simply because the tip-sample distance is not kept constant. Therefore the optical image on the left will have major contributions of topographically caused contrast. Still the optical image shows another effect, which is not perturbed by the topographic signal. With the vertical axis being the slow scan axis, it is noticeable that the focussed light shifts around on the tip with time. With scanning times for complete images of about 20 minutes, this is a very slow process, but it illustrates the importance of the focus being well-centered on the tip. During the first half of the scan (starting at the bottom-left corner) the incoming light obviously scattered more of the side of the tip, since the lines appear asymmetric in the optical image. During the coarse of the scan the drift of the focus accidentally corrected for the misalignment and for a short period one can see the left and the right edge of the line being enhanced in contrast. During the last vertical 500 nm of the scan the drift caused scattering from the other side of the tip as one can see from the shifted edge enhancement. The shifts were clearly induced by the focussing optics since the topographic image does not appear to shift in correlation with the optical effects.

Due to the narrow deep troughs in the topography of the sample and hence the possibility of changing tip-sample distances, the application of 2f-detection for the optical signal seems questionable. Still, scans were obtained and showed contrast in the optical and topographic images (figure 9.16). In the beginning of the scan the feedback regulation for the topographic signal was not stable and caused fluctuation in both the topography and the optical image. Therefore the brighter areas of the first part have to be discarded. About a quarter into the scan the topography was very stable and also the optical image

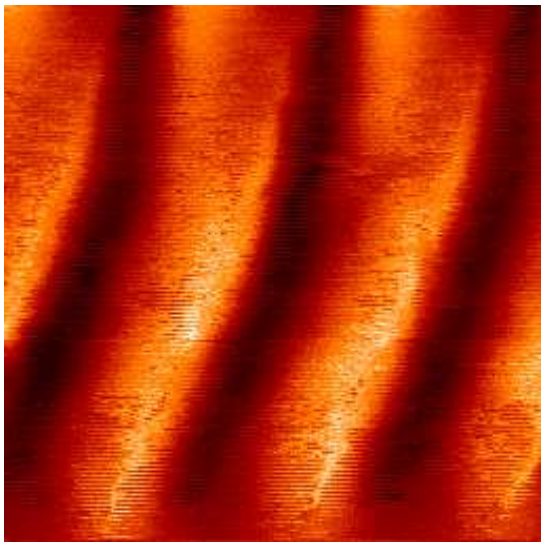

Figure 9.14: Apertureless NSOM: optical image 3 μm $\times$ 3 μm, first harmonic.

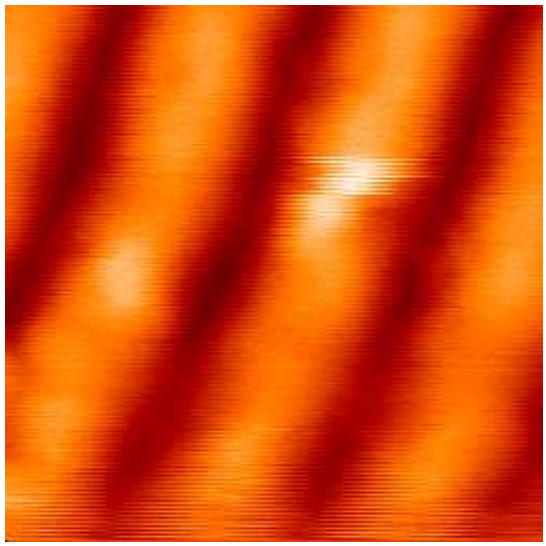

Figure 9.15: Apertureless NSOM: topographical image 3 μm $\times$ 3 μm.

revealed contrast. Again, the signal-to-noise was not good enough to give quantitative comparisons, but the optical signal tracks the topography very well. If the optical contrast is still topography-influenced can not be said at this point. Work by other groups suggests that constant-height scans at different heights above the surface can reveal the topographic contributions to the optical signal [110]. Unfortunately this requires reproducible scans over the same area, which is only possible at better signal-to-noise ratios than achieved in the current set-up.

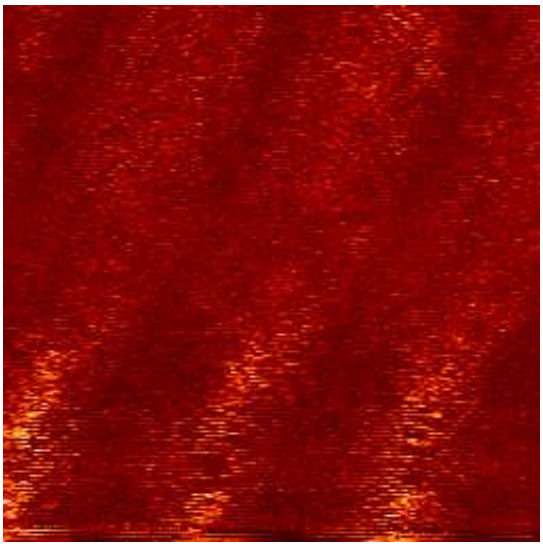

Figure 9.16: Aperture less NSOM: optical image 3 μm $\times$ 3 μm, second harmonic.

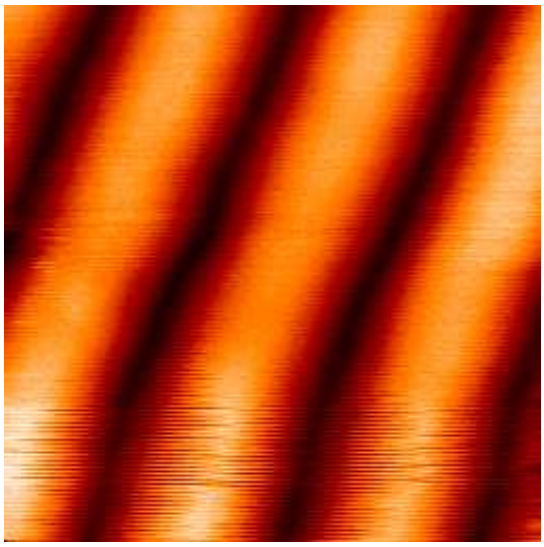

Figure 9.17: Aperture less NSOM: topographical image 3 μm $\times$ 3 μm.

10 Conclusions

For the first time subwavelength resolution has been demonstrated in the mid-infrared wavelength range. It was possible to observe microstructures, that are 10 times smaller than the used wavelength of $\lambda = 3$ μm [5]. At the same time the infrared wavelength range represents the "fingerprint" region for molecular vibrational and rotational excitation. With each molecule showing its characteristic infrared spectrum of absorption bands, it is easy to distinguish different chemical species. Infrared near-field optical microscopy shows the means to deliver microscopic resolution combined with chemical specificity. It was possible to distinguish small areas composed of different polymers in the latent image of the photoresist poly(t-butoxyoxycarbonylstyrene) (PTBOCST) purely by their infrared absorption contrast. The instrument was designed to operate in the wavelength range up to $\lambda = 3.3$ μm, specifically for monitoring the CH stretch vibration around 2900 cm^{-1} and OH band at 3300 cm^{-1}. Contrast mechanisms were found to be composed of pure absorption and contributions from changes of the refractive index at interfaces in the sample. By reducing the far-field collection angle of the instrument, the contrast was solely given by the absorption. Calculations of the optical contrast (about 2 % for a 250 nm thick polymer film) as well as the image spreading matched well with the observed results. Utilizing theoretical approximations for the near-field optical imaging process allowed good estimates on the field distribution at a subwavelength aperture for the infrared wavelength range.

Further information on latent image spreading and line edge roughness was achieved from fourier transform infrared spectroscopy. A new method to obtain microscopic information from substantially bigger areas is introduced, utilizing the high reproducibility of interferometric lithographic patterning. By averaging over many features of exactly the same size, feature broadening and hence diffusion could be observed in chemically amplified photoresists. The influence of parameters as UV dose and post exposure bake time was examined and diffusion constants as well as the nonlinear response function of a commonly used photoresist system could be determined. The results match well with work from other groups and show an alternative way of measuring lithographic resist properties with the advantage of studying realistically sized features.

Finally the introduction of an apertureless-type near-field optical microscope gave interesting insights into the realm of superresolution. The set-up included an interferometric

detection scheme for the collection beam path and an additional dither possibility for the probe cantilever for optical detection at the driving oscillation as well as for higher harmonics. With a flat, high optical contrast sample of gold islands on glass, lateral resolution of 30 nm can be reported. This number is in good agreement with the dimension of the probe, thus showing that the optical resolution limit is dominated by the size of the tip. The influence of topography induced artifacts in the optical image was studied and possible contributions decreased by detection at twice the modulation of the optical signal.

Apertureless NSOM was used to examine diblock copolymers on surfaces, which are aggregated to micelles. The possible use of the micelles for structuring of surfaces with metal nanoparticles made these polymers very interesting candidates for a surface sensitive optical method as near-field optical microscopy [104]. Even though optical absorption contrast was expected to be nonexistent at the wavelength used ($\lambda = 633$ nm), images were obtained with features that could not be explained by the influence of topography but had to be assigned to optical contrast. Due to strong absorption in the infrared wavelength range, contrast contributions are possible in the visible as for example shown by Kramer-Kronigs relations. Also plasmon enhancements due to the gold-coated probe could have caused the sample induced fluctuations [86]. Due to a very low overall signal, quantitative analysis was not feasible, but the images show a definite correlation between the position of features in the topography and the optical signal.
Examination of the photopolymer samples as used before did not yield convincing optical contrast, since a big influence of the topographic pattern had to be assumed. Nevertheless this demonstrated the extreme surface sensitivity of apertureless near-field optical microscopy as shown theoretically.

In order to reach an even more detailed picture of latent image formation in chemically amplified photopolymer resists the optical resolution of the instruments demonstrated has to be extended. Promising results were obtained for the apertureless near-field optical microscope and it seems reasonable to broaden the optical wavelength range into the infrared regime, even though experimentally more difficulties have to be faced as for example the need of sensitive IR detectors and intensive IR sources for the required wavelength range. With this said, another possibility could also be microscopy by coherent anti-stokes raman scattering (CARS) [111], which has been demonstrated to give rich contrast for thin polymer films [112, 113] just recently. Methods that have shown enhancement of the optical signal in the infrared range are surface enhanced raman scattering (SERS) [114] or surface enhanced infrared absorption (SEIRA) [115], but require specially prepared surfaces to allow an amplified contrast.

Bibliography

[1] G. Moore. Proc. Soc. Photo-Opt. Instr. Eng., **2438**(2), (1995).

[2] H. Ito and C. G. Willson. Polym. Eng. Sci., **23**,1012, (1982).

[3] J. Frechet, H. Ito, and C. G. Willson. Proceedings of Microcircuit Engineering, **82**,260, (1982).

[4] T. Mulvey and eds. C. J. R. Sheppard. *Advances in optical and electron microscopy.* Academic Press, New York, ((1991)).

[5] B. Dragnea, J. Preusser, J. M. Szarko, S. R. Leone, and W. D. Hinsberg. *Pattern characterization of deep-ultraviolet photoresists by near-field infrared microscopy.* Journal of Vacuum Science and Technology B, **19**(1),142–152, (2000).

[6] B. Knoll and F. Keilmann. *Near-field probing of vibrational absorption for chemical microscopy.* Nature, **399**,134–137, (1999).

[7] P. Hartsuch. *Chemistry of Lithography.* Lithographic Technical Foundation, New York, ((1961)).

[8] W. Moreau. *Semiconductor Lithography.* Plenum Press, New York, ((1988)).

[9] C. G. Willson, L. Thompson, and M. Bowden. *Introduction to microlithography.* American Chemical Society, Washington D.C., ((1994)).

[10] W. DeForest. *Photoresist: Materials and Processes.* McGraw-Hill, New York, ((1975)).

[11] R. Dammel. *Diazonaphthoquinone-based Resists.* SPIE Optical Engineeering Press, Bellingham, Washington, ((1993)).

[12] F. Billmeyer. *Textbook of Polymer Science.* Wiley-Interscience, New York, ((1984)).

[13] eds. N. Einspruch. *VLSI Electronics: Microstructure Science, Vol 1.* Academic Press, New York, ((1981)).

[14] K. Patterson, T. Okoroanyanwu, T. Shimokawa, S. Cho, J. D. Byers, and C. G. Willson. Proc SPIE, **3333**,425, (1998).

[15] L. Schlegel, T. Ueno, N. Hayashi, and T. Iwayanagi. *Determination of acid diffusion in chemical amplification positive deep ultraviolet resist.* Journal of Vacuum Science and Technology B, **9**(2),278–289, (1990).

[16] W. Hinsberg, F. Houle, G. Wallraff, M. Sanchez, M. Morrison, J. Hoffnagle, H. Ito, C. Nguyen, C..E. Larson, P. J. Brock, and G. Breyta. *Factors controlling pattern formation in chemically amplified resists at sub-100 nm dimensions.* Journal of Photopolymer Science and Technology, **12**(4),649–662, (1999).

[17] G. W. Reynolds and J. W. Taylor. *Factors contributing to sidewall roughness in a positive-tone, chemically amplified resist exposed by x-ray lithography.* Journal of Vacuum Science and Technology B, **17**(2),334–344, (1999).

[18] B. Lu, J. W. Taylor, F. Cerrina, C. P. Soo, and A. J. Bourdillon. *Study of acid diffusion in a positive tone chemically amplified resist using an on-wafer imaging technique.* Journal of Vacuum Science and Technology B, **17**(6),3345–3350, (1999).

[19] G. Wallraff, J. Hutchinson, W. Hinsberg, F. Houle, P. Seidel, R. Johnson, and W. Oldham. *Thermal and acid-catalyzed deprotection kinetics in candidate deep ultraviolet resist materials.* Journal of Vacuum Science and Technology B, **12**(6),3857–3862, (1994).

[20] E. Reichmanis, S. MacDonald, and T. Iwayanagi. *Polymers in Microlithography, ACS Symposium, Series 412.* American Chemical Society, Washington D.C., ((1989)).

[21] J. P. Fouiassier and eds. J. F. Rabek. *Radiation Curing in Polymer Science and Technology (Vol II): Photoinitiating Systems.* Elsevier, New York, ((1993)).

[22] M. Zuniga, G. Wallraff, and A. R. Neureuther. *Reaction diffusion kinetics in deep-uv positive tone resist systems.* SPIE, **2438**,113–124, (1995).

[23] L. E. Ocola, F. Cerrina, and T. May. *Synchrotron radiation micro-fourier transform infrared spectroscopy applied to photoresist imaging.* Applied Physics Letters, **71**(6),847–849, (1997).

[24] J. Crank. *The mathematics of diffusion.* Clarendon Press, Oxford, ((1975)).

[25] E. L. Cussler. *Diffusion, mass transfer in fluid systems.* Cambridge University Press, Cambridge, ((1997)).

[26] X. Shi. *Effect of coulomb interaction and pka on acid diffusion in chemically amplified resists.* Journal of Vacuum Science and Technology B, **17**(2),350–354, (1999).

[27] A. Fick. *Über diffusion.* Annalen der Physik, **170**(59), (1855).

[28] T. Alfrey Jr., E. F. Gurnee, and W. G. Lloyd. *Diffusion in glassy polymers.* Journal of Polymer Science, Part C, **12**(249), (1966).

[29] R. A. Grinsted, L. Clark, and J. L. Koenig. *Study of cyclic sorption desorption into poly(methacrylate) rods using nmr imaging.* Macromolecules, **25**(4),1235, (1992).

[30] W. Qin, Y. Shen, and L. Fei. Chinese Journal of Polymer Science, **11**,358, (1993).

[31] T. Itani, H. Yoshino, S. Hashimoto, M. Yamana, N. Samoto, and K. Kasama. *A study of acid diffusion in chemically amplified deep ultraviolet resist.* Journal of Vacuum Science and Technology B, **14**(6),4226–4228, (1996).

[32] S. Pickup and F. D. Blum. *Self-diffusion of toluene in polystyrene solutions.* Macromolecules, **22**(10),3961, (1989).

[33] B. Nystroem, M. E. Moseley, W. Brown, and J. Roots. Journal of Applied Polymer Science, **26**,3385, (1981).

[34] F. A. Houle, W. D. Hinsberg, M. Morrison, M. I. Sanchez, G. Wallraff, C. Larson, and J. Hoffnagle. *Determination of coupled acid catalysis-diffusion processes in a positive tone chemically amplified photoresist.* Journal of Vacuum Science and Technology B, **18**(4),1874–1885, (2000).

[35] D. A. Edwards. *Non-fickian diffusion in thin polymer films.* Journal of Polymer Science, Part B, **34**,981–997, (1996).

[36] M. Cheng, J. Tyminski, E. Croffie, and A. Neureuther. *Modeling anomalous depth dependent dissolution effects in chemically amplified resists.* Journal of Vacuum Science and Technology B, **18**(3),1294–1298, (2000).

[37] R. A. Jones, D. J. R. Taylor, J. I. Cail, R. F. T. Stepko, and I. M. Ward. *Atomistic modeling of the formation of radical pairs in irradiated amorphous poly(propylene).* Macromolecules, **32**,8350–8355, (1999).

[38] J. I. Cail, D. J. R. Taylor, R. F. T. Stepko, M. G. Brereton, R. A. Jones, M. E. Ries, and I. M. Ward. *Computer simulation studies of molecular orientation in polyethylene networks: orientation functions and the legendre addition theorem.* Macromolecules, **33**,4966–4971, (2000).

[39] D. J. R. Taylor, R. F. T. Stepko, R. A. Jones, and I. M. Ward. *Computer simulation studies of molecular orientation and the stress-optical properties of polyethylene networks.* Macromolecules, **32**,1978–1989, (1999).

[40] L. Bergmann and C. Schaefer. *Lehrbuch der Experimentalphysik, Band 3, Optik.* Walter de Gruyter, Berlin, ((1987)).

[41] E. Abbé. Arch. Mikrosk. Anat., **9**,413–468, (1873).

[42] P. Toeroek. *Imaging of small birefringent objects by polarised light conventional and confocal microscopes.* Optics Communications, **181**,7–18, (2000).

[43] R. H. Webb. *Confocal optical microscopy.* Reports on Progress in Physics, **59**,427–471, (1996).

[44] E. H. Synge. *Suggested method for extending microscopic resolution into the ultramicroscopic region.* Philos. Mag., **6**,356–362, (1928).

[45] E. A. Ash and G. Nicholls. *Super-resolution aperture scanning microscope.* Nature, **237**,510–512, (1972).

[46] D. W. Pohl, W. Denk, and M. Lanz. *Optical stethoscopy: image recording with resolution λ/20.* Applied Physics Letters, **44**,651–653, (1984).

[47] R. C. Dunn. *Near-field scanning optical microscopy.* Chemical Review, **99**,2891–2927, (1999).

[48] J. W. P. Hsu. *Near-field scanning optical microscopy studies of electronic and photonic materials and devices.* Materials Science and Engineering, **R33**(1),1–50, (2001).

[49] H. A. Bethe. *Theory of diffraction by small holes.* The Physical Review, **66**(7,8),163–182, (1944).

[50] C. J. Bouwkamp. *On bethe's theory of diffraction by small holes.* Philips Research Reports, **5**(5),321–332, (1950).

[51] C. J. Bouwkamp. *On the diffraction of electromagnetic waves by small circular disks and holes.* Philips Research Reports, **5**(6),401–422, (1950).

[52] L. Novotny, D. W. Pohl, and P. J. Regli. *Light-propagation through nanometer-sized structures - the 2-dimensional-aperture scanning near-field optical microscope.* Journal of the Optical Society of America A, **11**(6),1768–1779, (1994).

[53] B. Hecht, H. Bielefeldt, and D. W. Pohl. *Influence of detection conditions on near-field optical imaging.* Journal of Applied Physics, **84**(11),5873–5882, (1998).

[54] Y. Leviatan. *Study of near-zone fields of a small aperture.* Journal of Applied Physics, **60**(5),1577–1583, (1986).

[55] H. Heinzelmann, T. Lacoste, T. Huser, H. J. Guentherodt, B. Hecht, and D. W. Pohl. *Instrumental developments and recent experiments in near-field optical microscopy.* Thin Solid Films, **273**(1-2),149–153, (1996).

[56] D. W. Pohl. *Near-field optics - light for the world of nano-scale science.* Thin Solid Films, **264**(2),250–254, (1995).

[57] L. Novotny and C. Hafner. *Light-propagation in a cylindrical wave-guide with a complex, metallic, dielectric function.* Physical Review E, **50**(5),4094–4106, (1994).

[58] H. Heinzelmann, T. Huser, T. Lacoste, H. J. Guentherodt, D. W. Pohl, B. Hecht, L. Novotny, O. J. F. Martin, C. V. Hafner, H. Baggenstos, U. P. Wild, and A. Renn. *Scanning near-field optical microscopy in basel, ruschlikon, and zurich.* Optical Engineering, **34**(8),2441–2454, (1995).

[59] F. Zenhausern, Y. Martin, and H. K. Wickramasinghe. *Scanning interferometric apertureless microscopy: optical imaging at 10 angstrom resolution.* Science, **269**,1083–1085, (1995).

[60] H. F. Hamann, M. Kuno, A. Gallagher, and D. J. Nesbitt. *Molecular fluorescence in the vicinity of a nanoscopic probe.* Journal of Chemical Physics, **114**(19),8596–8609, (2001).

[61] R. Hillenbrand and F. Keilmann. *Complex optical constants on a subwavelength scale.* Physical Review Letters, **85**(14),3029–3032, (2000).

[62] B. Hecht, H. Bielefeldt, Y. Inouye, and D. W. Pohl. *Facts and artifacts in near-fiel optical microscopy.* Journal of Applied Physics, **81**(6),2492–2498, (1997).

[63] K. Fukuzawa and Y. Tanaka. *Apertureless near-field optical microscopy with differential and close-proximity detection.* Applied Physics Letters, **71**(2),169–171, (1997).

[64] R. Hillenbrand, B. Knoll, and F. Keilmann. *Pure optical contrast in scattering-type scanning near-field microscopy.* Journal of Microscopy, **202**(1),77–83, (2001).

[65] M. Labardi, S. Patane, and M. Allegrini. *Artifact-free near-field optical imaging by apertureless microscopy.* Applied Physics Letters, **77**(5),621–623, (2000).

[66] N. Maghelli, M. Labardi, S. Patane, F. Irrera, and M. Allegrini. *Optical near-field harmonic demodulation in apertureless microscopy.* Journal of Microscopy, **202**(1),84–93, (2000).

[67] W. Hinsberg, F. A. Houle, J. Hoffnagle, M. Sanchez, G. Wallraff, M. Morrison, and S. Frank. *Deep-ultraviolet interferometric lithography as a tool for assessment of chemically amplified photoresist performance.* Journal of Vacuum Science and Technology B, **16**(6),3689–3694, (1998).

[68] C. Durkan and I. V. Shvets. *Investigation of the physical mechanisms of shear-force imaging.* Journal of Applied Physics, **80**(10),5659–5664, (1996).

[69] R. Brunner, A. Bietsch, O. Hollrichter, and O. Marti. *Distance control in near-field optical microscopy with piezoelectrical shear-force detection suitable for imaging in liquids.* Review of Scientific Intruments, **68**(4),1769–1772, (1997).

[70] A. G. T. Ruiter, J. A. Veerman, K. O. van der Werf, and N. F. van Hulst. *Dynamic behavior of tuning fork shear-force feedback.* Applied Physics Letters, **71**(1),28–30, (1997).

[71] M. Schuettler, M. Leuschner, M. Lippitz, W. W. Ruehle, and H. Giessen. *Towards the origin of the shear force in near-field microscopy.* Japanese Journal of Applied Physics, **40**,813–818, (2001).

[72] K. Karrai and R. Grober. *Piezoelectric tip-sample distance control for near-field optical microscopes.* Applied Physics Letters, **66**(14),1842–1844, (1995).

[73] M. A. Unger, D. A. Kossakovski, R. Kongovi, J. L. Beauchamp, J. D. Baldeschwieler, and D. V. Palanker. *Etched chalcogenide fibers for near-field infrared scanning microscopy.* Rev. Sci. Instrum., **69**(8),2988–2993, (1998).

[74] R. Stoeckle, C. Fokas, V. Deckert, R. Zenobi, B. Sick, B. Hecht, and U. P. Wild. *High-quality near-field optical probes by tube etching.* Applied Physics Letters, **75**(2),160–162, (1999).

[75] D. T. Schaafsma, R. Mossadegh, J. S. Sanghera, and I. D. Aggarwal. *Singlemode chalcogenide fiber infrared snom probes.* Ultramicroscopy, **77**,77–81, (1999).

[76] D. J. M. Stothard, M. Ebrahimzadeh, and M. H. Dunn. *Low-pump-threshold continuous-wave singly resonant optical parametric oscillator.* Optics Letters, **23**(24),1895–1897, (1998).

[77] C. Gmachl, F. Capasso, D. L. Sivco, and A. Y. Cho. *Recent progress in quantum cascade lasers and applications.* Reports on Progress in Physics, **64**,1533–1601, (2001).

[78] Z. Feit, M. McDonald, R. J. Woods, V. Archambault, and P. Mak. *Low threshold pbeusete/pbte separate confinement buried heterostructure diode lasers.* Applied Physics Letters, **68**(6),738–740, (1996).

[79] D. L. Partin. *Lead salt quantum effect structures.* IEEE, J. Quantum Electronics, **24**(8),1716, (1988).

[80] Laser Components GmbH, Germany. *Indium Antimonide Detectors.*

[81] R. Bhargava, B. G. Wall, and J. L. Koenig. *Comparison of the ft-ir mapping and imaging techniques applied to polymeric systems.* Applied Spectroscopy, **54**(4),470–479, (2000).

[82] J. S. Batchelder and M. A. Taubenblatt. *Interferometric detection of forward scattered light from small particles.* Applied Physics Letters, **55**(3),215–217, (1989).

[83] M. G. Somekh, M. S. Valera, and R. K. Appel. *Scanning heterodyne confocal differential phase and intensity microscope.* Applied Optics, **34**(22),4857–4868, (1995).

[84] M. Vaez-Iravani and R. Toledo-Crow. *Phase contrast and amplitude pseudoheterodyne interference near field scanning optical microscopy.* Applied Physics Letters, **62**(10),1044–1046, (1993).

[85] F. Zenhausern, M. P. O'Boyle, and H. K. Wickramasinghe. *Apertureless near-field optical microscope.* Applied Physics Letters, **65**(13),1623–1625, (1994).

[86] H. F. Hamann, A. Gallagher, and D. J. Nesbitt. *Enhanced sensitivity near-field scanning optical microscopy at high spatial resolution.* Applied Physics Letters, **73**(11),1469–1471, (1998).

[87] B. Dragnea, J. Preusser, W. Schade, S. R. Leone, and W. D. Hinsberg. *Transmission near-field scanning microscope for infrared chemical imaging.* Journal of Applied Physics, **86**(5),2795–2799, (1999).

[88] N. Gross, A. Dazzi, J. M. Ortega, R. Andouart, R. Prazeres, C. Chicanne, J. P. Goudonnet, Y. Lacroute, C. Boussard, G. Fonteneau, and S. Hocdé. *Infrared near-field study of a localised absorption in a thin film.* European Physics Journal, **16**,91–98, (2001).

[89] B. Dragnea, J. Preusser, J. M. Szarko, L. A. McDonough, S. R. Leone, and W. D. Hinsberg. *Chemical mapping of patterned polymer photoresists by near-field infrared microscopy.* Applied Surface Science, **175-176**,783–789, (2001).

[90] C. A. Michaels, L. J. Richter, R. R. Cavanagh, and S. J. Stranick. *Chemical imaging with scanning near-field infrared microscopy and spectroscopy.* Proceedings SPIE: Optical devices and material diagnostics, **4098**,102–109, (2000).

[91] A. Piednoir, C. Licoppe, and F. Creuzet. *Imaging and local infrared spectroscopy with a near field optical microscope.* Optics Communications, **129**,414–422, (1996).

[92] P. M. Dentinger, B. Lu, J. W. Taylor, S. J. Bukofsky, G. D. Feke, D. Hessman, and R. D. Grober. *On-wafer photoacid determination and imaging technique for chemically amplified photoresists.* Journal of Vacuum Science and Technology B, **16**(6),3767–3772, (1998).

[93] K. C. Tseng, N. J. Turro, and C. J. Durning. *Molecular mobility in polymer thin films.* Physical Review E, **61**(2),1800–1811, (2000).

[94] R. D. Schaller, J. C. Johnson, K. R. Wilson, L. F. Lee, L. H. Haber, and R. J. Saykally. *Nonlinear chemical imaging nanomicroscopy: from second and third harmonic generation to multiplex (broad-bandwidth) sum frequency generation near-field scanning optical microscopy.* Journal of Physical Chemistry, **106**,5143–5154, (2002).

[95] J. Preusser, L. Muntean, S. R. Leone, W. D. Hinsberg, and W. Schade. *Infrared transmission study of acid-catalyzed diffusion properties with micropatterned chemically amplified photoresists.* to be published.

[96] E. M. Lee, M. G. Sung, Y. M. Lee, Y. S. Sohn, and H. K. Oh. *Characterization of 193 nm chemically amplified resist during postexposure bake and postexposure delay.* Japanese Journal of Applied Physics, **38**,7094–7098, (1999).

[97] A. Lahrech, R. Bachelot, P. Gleyzes, and A. C. Boccara. *Infrared reflection-mode near-field microscopy using an apertureless probe with a resolution of $\lambda/600$.* Optics Letters, **21**(17),1315–1317, (1996).

[98] J. C. Hulteen and R. P. Van Duyne. *Nanosphere lithography: A materials general fabrication process for periodic particle array surfaces.* Journal of Vacuum Science and Technology A, **13**,1553–1558, (1995).

[99] D. Rugar, H. J. Mamin, and P. Guethner. *Improved fiber-optic interferometer for atomic force microscopy.* Applied Physics Letters, **55**(25),2588–2590, (1989).

[100] T. Ohio, N. Nakatani, Y. Sakai, and N. Suzuki. *Atomic force microscope using an optical fiber heterodyne interferometer free from external disturbances.* Japanese Journal of Applied Physics, **32**,2994–2998, (1993).

[101] F. S. Bates and G. H. Frederickson. *Block copolymers thermodynamics - theory and experiments.* Annual Review of Physical Chemistry, **41**,525, (1990).

[102] G. Krausch. *Surface-induced self-assembly in thin polymer-films.* Mater. Res. Rep., **14**(1-2),1–94, (1995).

[103] B. A. Garetz, M. C. Newstein, H. J. Dai, S. V. Jonnalagadda, and N. P. Balsara. *Birefringence and diffraction of light in ordered block copolymer materials.* Macromolecules, **26**,3151–5155, (1993).

[104] J. P. Spatz, P. Eibeck, S. Moessmer, M. Moeller, E. Y. Kramarenko, P. G. Khalatur, I. I. Potemkin, A. R. Khokhlov, R. G. Winkler, and P. Reineker. *Order-disorder transition in surface-induced nanopattern of diblock copolymer films.* Macromolecules, **33**,150–157, (2000).

[105] J. P. Spatz, M. Moeller, and P. Ziemann. *Nanolithographie mit selbstorganisierenden masken.* Physikalische Blaetter, **55**(12),49–52, (1999).

[106] A. Kramer, W. Trabesinger, B. Hecht, and U. P. Wild. *Optical near-field enhancement at a metal tip probed by a single fluorophore.* Applied Physics Letters, **80**(9),1652–1654, (2002).

[107] Y. C. Martin, H. F. Hamann, and H. K. Wickramasinghe. *Strength of the electric field in apertureless near-field optical microscopy.* Journal of Applied Physics, **89**(10),5774–5778, (2001).

[108] J. L. Bohn, D. J. Nesbitt, and A. Gallagher. *Field enhancement in apertureless near-field scanning optical microscopy.* Journal of the Optical Society of America A, **18**(12),2998–3006, (2001).

[109] J. Preusser, L. Muntean, B. Dragnea, Z. H. Kim, and S. R. Leone. *Phase transition studies in diblock-copolymers using a differential heterodyne/homodyne apertureless near-field scanning optical microscope.* to be published.

[110] B. B. Akhremitchev, S. Pollack, and G. C. Walker. *Apertureless scanning near-field infrared microscopy of a rough polymeric surface.* Langmuir, **17**,2774–2781, (2001).

[111] A. Zumbusch, G. R. Holtom, and X. S. Xie. *Three-dimensional vibrational imaging by coherent anti-stokes raman scattering.* Physical Review Letters, **82**(20),4142–4145, (1999).

[112] J. X. Cheng, L. D. Book, and X. S. Xie. *Polarization coherent anti-stokes raman scattering microscopy.* Optics Letters, **26**(17),1341–1343, (2001).

[113] E. O. Potma, D. J. Jones, J. X. Cheng, X. S. Xie, and J. Ye. *High sensitivity cars microscopy with two tightly syncronized picosecond lasers.* Optics Letters, **27**(13),1168–1170, (2002).

[114] J. J. Ge, G. Xue, F. Li, K. W. McCreight, S. Y. Wand, F. W. Harris, S. Z. D. Cheng, X. Zhuang, S. C. Hong, and Y. R. Shen. *Surface studies of polyimide thin films via surface-enhanced raman scattering and second harmonic generation.* Macromol. Rapid Communications, **19**,619–623, (1998).

[115] A. Hartstein, J. R. Kirtley, and J. C. Tsang. *Enhancement of the infrared-absorption from molecular monolayers with thin metal overlayers.* Physical Review Letters, **45**(3),201–204, (1980).

Publications based on work in the context of this thesis:

1. B. Dragnea, J. Preusser, J. M. Szarko, S. R. Leone, and W. D. Hinsberg, *Pattern characterization of deep-ultraviolet photoresists by near-field infrared microscopy*, Journal of Vacuum Science and Technology B, **19**(1), 142-152, (2000).

2. B. Dragnea, J. Preusser, W. Schade, S. R. Leone, and W. D. Hinsberg, *Transmission near-field scanning microscope for infrared chemical imaging*, Journal of Applied Physics, **86**(5), 2795-2799, (1999).

3. B. Dragnea, J. Preusser, J. M. Szarko, L. A. McDonough, S. R. Leone and W. D. Hinsberg, *Chemical mapping of patterned polymer photoresists by near-field infrared microscopy*, Applied Surface Science, (175-176), 783-789, (2001).

4. J. Preusser, L. Muntean, S. R. Leone, W. D. Hinsberg, and W. Schade, *Infrared transmission study of acid-catalyzed diffusion properties with micropatterned chemically amplified photoresists*, (submitted).

5. J. Preusser, L. Muntean, B. Dragnea, Z. H. Kim, W. Schade, and S. R. Leone, *Phase transition studies in diblock-copolymers using a differential heterodyne/homodyne apertureless near-field scanning optical microscope*, (in preparation).

6. L. A. McDonough, B. Dragnea, J. Preusser, and S. R. Leone, *Water vapor uptake in photolithographic polymers observed by infrared near-field scanning optical microscopy in vacuum*, Journal of Physical Chemistry B, (submitted).

7. E. Potma, X. Sunney Xie, L. Muntean, J. Preusser, D. Jones, J. Ye, S. R. Leone, W. D. Hinsberg, and W. Schade, *Chemical imaging of photoresists with coherent anti-Stokes Raman scattering (CARS) microscopy*, Chemical Physics

8. W. Schade, J. Preusser, D. L. Osborn, Y. Y. Lee, J. deGouw, and S. R. Leone, *Spatially resolved femtosecond time correlation measurements on a GaAsP photodiode*, Optics Communications, **162**(4-6), 200-204, (1999).

9. W. Schade, D. L. Osborn, J. Preusser, and S. R. Leone, *Two-color cross-correlation of fs-laser pulses by two-photon induced photoconductivity for near and far field optical measurements*, Optics Communications, **150**(1-6), 27-32, (1998).

Acknowledgements

Foremost I would like to thank each and everyone who has contributed to the success of this work considering both the scientific inputs as well as everything related to life outside the "bubble".

I am sincerely indebted to my German advisor Wolfgang Schade for his support for all the years that we know. Giving me the opportunity to join him at the University of Colorado in Boulder, USA for completion of my diploma thesis had one of the greatest impacts on my life, which I am extremely thankful for. His stimulating suggestions, advice and encouragement helped me throughout this project. His straightforwardness contributed to an enlightening experience during graduate school and I am very grateful for his confidence and trust in my abilities, in times where I would rather be in doubt.

Not by a bit less am I obliged to my American advisor Stephen R. Leone for the willingness to let me actively participate in the research of his group. His generous offer to support me over all the years of graduate school in every possible sense was key to an utmost exciting experience in my life. I am thankful for his resourcefulness and influence, which was vital for the progress of this work. At the same time I was encouraged to develop and follow my own ideas on a topic, that was fascinating and challenging at the same time.

A lot of credit goes to the current and former members of the work groups on both sides of the Atlantic Ocean for scientific exchange and even more so for the not-so-scientific endeavors. Some people I would like to give special mention for numerous reasons - in no particular order:

Charles Blackledge, who can read scientific publications like other people do their daily newspaper and can always be persuaded to scientific discussions, provided the gold on glass samples. As a direct co-worker on the same experiment Ligia Muntean had to handle more than others and her contributions, especially her perseverance are greatly appreciated. As a source of wisdom and for his keen scientific intuition, that would spin the project in the most productive direction, I would like to thank Bogdan Dragnea. My lab-mates Laurie McDonough and Jodi Szarko have many contributions to this work, since they would be

willing to share their equipment and knowledge without hesitation. Her apparatus was situated at the opposite end of the building and is now placed even further away, yet Astrid Müller would always find the time for encouragement at low tides. Radek Uberna holds major contribution to this work as he is a lab-mate of the first hour. His influence helped to always keep a healthy and productive balance at work and I am thankful for the lasting friendship that originated in practicing this balance. I would especially like to thank a valued friend, Dirk Scheel, for keeping up the contact and for many reflections and thoughtful ideas on our common research. Quite a few helpful hints have contributed to problem-solving even across two continents. His willingness to always accommodate me without hesitation during my visits in Germany is greatly appreciated. Ulrike Willer I would like to thank for proof-reading this pamphlet even on short notice, for her incredible friendliness and all the wonderful and fancy foods I was ever invited to experience.

The staff at JILA needs special mentioning, since they were the most helpful throughout my stay in Colorado:

I am obliged to the instrument shops, their broad expertise and their enthusiasm to deal with about any problem they would be faced with, especially to Terry Brown for his willingness to share all his wisdom and the patience to repeat it, too. Building a Shot-noise limited differential detection scheme would have not been possible without his help. David Alchenberger is to be mentioned as well, the wizard of intractable materials, who for many times made the institute his second home to solve other people's and in particular my problems of technical nature. The lithography patterning and micro-machining for the microscope as well as a profound introduction to SEM-imaging is gratefully acknowledged.

The purchase office crew, namely Ed Holliness, Maryly Dole and Brian Lynch made shopping so comfortable and easy - it almost felt like Christmas when something wrapped got dropped off at your lab door.

Agnieszka Polanowski from administration and payroll I would like to thank for great friendship and for always making sure, that I could pay my rent.

I am grateful to Änne and Helmut Koschay for the generous offer to stay in their mansion. "Schimanski's Hideout" was an intriguing experience and is badly missed.

Special appreciation goes to my parents and sisters for supporting me and my decision to stay abroad at all times. Their contribution to a successful completion of this "project" is uncounted for.

Thank you all!

Eidesstattliche Erklärung

Hiermit versichere ich an Eides statt, daß ich die vorgelegte Arbeit selbstständig, ohne unerlaubte Hilfe verfaßt und die benutzten Hilfsmittel vollständig angegeben habe.

Clausthal-Zellerfeld,

Hiermit versichere ich an Eides statt, daß ich noch keine früheren Promotionsversuche unternommen habe.

Clausthal-Zellerfeld,